Fall 11-20-2015

Volatile Condensible Material Deposition in LEO Simulated Environment

Jinya Pu
University of Nebraska-Lincoln, pujinya@gmail.com

VOLATILE CONDENSIBLE MATERIAL DEPOSITION IN LEO SIMULATED ENVIRONMENT

by

Jinya Pu

A DISSERTATION

Presented to the Faculty of

The Graduate College at the University of Nebraska

In Partial Fulfilment of Requirements

For the Degree of Doctor of Philosophy

Major: Electrical Engineering

Under the Supervision of Professor Natale Ianno

Lincoln, Nebraska

December, 2015

VOLATILE CONDENSIBLE MATERIAL DEPOSITION IN LEO SIMULATED ENVIRONMENT

Jinya Pu, Ph.D.

University of Nebraska, 2015

Adviser: Natale J. Ianno

Room Temperature Vulcanized (RTV) silicone and compounds are widely used in outer-space for bonding or potting spacecraft components. In geosynchronous equatorial orbit (GEO), the silicone may outgas species which can condense on optically sensitive surfaces and degrade their performance, therefore shortening the lifetime of spacecraft. In low-earth-orbit (LEO), the silicone rubber is subject to an energetic and corrosive environment. Atomic oxygen (AO) and ultraviolet radiation can cause abrasion and degradation of the silicone rubber, cause changes in existing condensed VCM films and affect the properties of VCM films condensing in this atmosphere. Experiments were performed to simulate GEO conditions. In this work, the outgassed effluent of RTV566 silicone condensed at three different temperatures.The VCM films were analyzed by an *in-situ* quartz crystal microbalance (QCM) and spectroscopic ellipsometry (SE). A self-consistent analysis approach employing the QCM and SE data has been developed to link the physical and optical properties of the condensed VCM films. It has been shown that at 120K, the VCM film contained ice, while at 150 K and 180 K, the films condense via island nucleation. Experiments were performed to simulate LEO conditions. In this work, an electron cyclotron resonance (ECR) based system was utilized to create atomic oxygen. First, VCM films were deposited in a GEO simulation chamber, then these GEO films were transferred into the ECR system for the AO exposure. Second, the AO exposure and deposition of films oc-

curred simultaneously to produce LEO films for the first time. The results showed that the AO exposed GEO films are optically different than the LEO simulated films.

Table of Contents

List of Figures

List of Tables

Chapter 1

Introduction

A spacecraft operates in a hostile environment filled with light, charged particles, debris and other residual materials. When exposed to this environment, structural materials can become a major contamination source due to outgassing capability.[1] [2] Structural materials, such as elastomers, potting compounds, adhesive silicones, and films of these materials, etc., release molecules through outgassing in the space environment. Over a long lifetime, undesirable levels of outgassed molecules may remain on and contaminate critical spacecraft surfaces.[3].

Because of its broad range of operating temperatures and other benefits [4], silicone has been widely used in spacecraft applications. When bombarded by atomic oxygen (AO) in low earth orbit (LEO), silicone experiences oxidation in methyl groups and gradually transforms into silica [5]. This contamination may become critically harmful when low-molecular-weight, volatile silicone molecules outgas from the silicone matrix and re-deposit on spacecraft surfaces. For example, these small silicone deposits may also be bombarded by AO and transform into silica before they reevaporate. As long as the outgassing species are deposited on surfaces, there will be an accumulation of silica over a period of time. Therefore, the thickened deposit will eventually reduce optical transmittance, diffuse reflectance and increase absorptance. [6]

1.1 Background

1.1.1 History

Due to their desirable characteristics, polymer silicones have been tested and used by the Goddard Space Flight Center (GSFC), European Space Research Organization (ESRO), and Jet Propulsion Lab (JPL).[7] [8]

For over half a century, silicones were used as adhesives for windows, solar panels, and atomic oxygen protective coatings during NASA test flights [9]. Upon return of the spacecraft, oily residues caused by low-molecular-weight species can be observed on screening surfaces [1]. Analysis has shown that low-molecular-weight polymers, which had not cross-linked into the silicone polymer matrix, outgas and deposit on Space Shuttle surfaces[10]. Based on the importance of using low outgassing materials in space, NASA and other space agencies use low outgassing materials, also known as controlled volatility materials (CVM). It is recommended that all adhesives used in outer space environments be tested prior to use since volatile species may release from a structural material under certain conditions in extraterrestrial environments [11].

1.1.2 ASTM E 595 Test Standard

The American Society for Testing and Materials (ASTM) utilized a screening technique for volatile species that could outgas from a material in a vacuum or space environment [11].

Using ASTM E 595, a sample of a test material was held at a temperature of 125 °C for 24 hours at a pressure of less than 7×10^{-3} Pa. Two critical parameters were measured: total mass loss (TML) and collected volatile condensable materials

(CVCM). In addition, water vapor regained (WVR) could be obtained after measuring these two parameters.

This material screening method defined the typical pass/fail criteria for most spacecraft materials as 1% TML and 0.1% CVCM.

ASTM E 595 is one of the older methods for measuring outgassing species. As it did not take activation energy or the absorption coefficient into consideration, this test method could be misleading.

Somehow, a high activation energy material would pass the test with slow outgassing, and most of the outgassable content left the material.

A material with a significant TML value may have a low or transparent CVCM or vice versa, a small TML with significant CVCM may have optically black outgassing material.

Another drawback of ASTM E 595, was that since the test temperature was fixed, materials that condense below 25 °C are not detected. The data measured did not provide specific material and deposition surface temperatures with which a material's impact on the performance of a system could be determined.

1.1.3 ASTM E 1559-93 Test Standard

In order to collect kinetics data on time- and temperature-dependent material outgassing/deposition, ASTM E 595 was abandoned. In 1993, ASTM E 1559-93, a method for measuring the accurate outgassing condensation rates of materials, was standardized by Lockheed under U.S. Air Force sponsorship [12]. In addition to measuring endpoint TML and CVCM, ASTM E 1559-93 can provide time-integral TML and CVCM.

Materials to be tested are placed in a temperature-controlled effusion cell in a

vacuum chamber, where outgassing flux impinges on quartz crystal microbalances (QCMs) which are maintained at different temperatures. When the deposition ceases, the QCMs are wire-heated to eliminate the deposit on the crystal surface. Meanwhile, the frequency-temperature profile can be extracted for QCM thermogravimetric analysis (QTGA). The major strength of the QCM collection method is the ability to measure both outgassing and deposition data simultaneously and the ability to thermally analyze the outgassed species by QTGA.

Nevertheless, there are several factors which may impact the precision of the measurement. These include, for example, the introduction of a view factor relating the orifice of an effusion cell and a QCM substrate, and the noncondensability of some outgassed species at liquid nitrogen temperatures if the outgassed species occupy a large portion of the outgassing products.

1.2 Motivation

The ASTM E 1559 test standard is a powerful tool for characterizing the outgassing and deposition kinetics of essentially any materials, including adhesives, coatings, films, elastomers and components, which can be cut to fit into the effusion cell.

However, in a space environment, especially low earth orbit, ultraviolet radiation, atomic oxygen, thermal cycles, etc., would significantly degrade the material characteristics and subsequently the VCM deposited. [13]

In previous experiments, the properties of photochemically deposited films resulting from VCM outgassing have been quantified, in terms of spectra and deposition temperature [14] [15]. By varying the substrate-film combination, reflection/transmission spectra changes have been quantified [7]. The outgassing rate effected by temperature cycling and ultraviolet radiation has been put into laboratory measurement protocols and numeric simulations [16].

Reaction of AO with different polymeric materials has been shown to occur by various mechanisms. The basic mechanisms are abstraction, addition, elimination, insertion and replacement [7] [17].

The interaction of AO with spacecraft surfaces will result in mass loss and changes in surface morphology and optical, mechanical and thermal properties. In order to protect the exposed surfaces of spacecraft, thin layers of an AO-resistant material can be applied [18]. Coatings of inorganic oxides, such as aluminum oxide and silicon oxide, as well as polymers have been shown to protect surfaces against oxygen plasma and AO erosion [5].

Because of their ease of use and flexibility, polymeric materials are used for protecting surfaces. When exposed to AO radiation, non-carbon-based polymers are converted into protective silica-like coatings [18]. Ground-based tests have shown that silicones exposed to vacuum UV radiation and atomic oxygen release small-weight molecules which can deposit and hence contaminant neighboring surfaces.[19].

However, due to the limited thickness of photo-deposited films and unwanted residue on the surfaces measured, optical constants of these contaminants cannot be extracted properly. Yet they determine material behavior on optically sensitive surfaces. The deposition of outgassing polymers and their effects on optical surface performance have not been studied. Moreover, a VCM film can be further oxidized by AO flux, altering the initial optical constants.

By simulating the LEO environment with UV radiation, vacuum and AO flux, tests of AO behavior on protective polymeric materials can be performed to investigate their optical changes. The VCM resulting from outgassing will be bombarded under AO during and after the deposition process. Real-time ellipsometry is used to observe the VCM spectrum change.

1.3 Approaches

In order to measure VCM deposition at cryogenic temperatures, a high sensitivity QCM is employed. Meanwhile, *in situ* spectroscopic ellipsometry is used on the crystal substrate to observe changes in the VCM optical constants. An effusion cell is set to the selected temperature with a shutter at its orifice for output control. Using these two techniques in tandem allows us to detect thickness growth and optical constants of the VCM in real time. Even though the film thickness is less than 20 nm, using a simple assumption for the density of material, n and k as a function of wavelength can be extracted. Using the QTGA method, outgassed species of the VCM can be analyzed at different deposition temperatures. The QCM can be substituted for a silicon wafer at a fixed temperature for another substrate-film combination.

To investigate the effect of AO on a VCM, photodeposited VCM films are transferred into an AO simulation chamber. Ellipsometry is used to observe the optical change to these films. In another approach to measuring AO effects on a VCM, the growing photo-fixed VCM films are simultaneously bombarded by AO. These processed films are characterized via *ex situ* ellipsometry.

Chapter 2

Instrumentation

2.1 Cryogenic Deposition

2.1.1 QCM

The QCM (Quartz Crystal Microbalance) has commonly been used for monitoring deposition rates of thin films. Also it has been demonstrated to work well at cryogenic temperatures to measure the contaminant accumulation on cold surfaces and identify molecular species from 5K to 400K with mass sensitive piezoelectric crystals which can oscillate at 10MHz, 15MHz or 18MHz [20] [21] [22]. Also the QCMs have been used to measure condensation coefficients [23] [24], gas absorption [25], and sublimation rates [26].

The reason that the QCM has been widely used in mass deposition rate monitoring nowadays is single-crystal quartz oscillators are extremely stable with time, and also highly reproducible from one batch to another.

Finally is it has excellent mechanical properties unchanged over a long period of time (few per million Hz per year) [27].

2.1.1.1 Theory

The quartz crystal, used as a surface acoustic resonator, has different modes of vibration which include the flexure mode, the extensional mode and the shear mode [28]. These basic vibration modes correspond to different crystal cutting angles, which therefore result in different vibrating frequency ranges [29]. In today's quartz resonator applications, the thickness shear mode (within the shear mode) is mostly used for minute mass monitoring due to its fundamental frequency range.

Equivalent oscillator circuits for driving a QCM can be found from these references [30] [31] [32] [33]. The QCM is a mechanical device linked to an electric circuit using the piezoelectric effect[34].

Figure 2.1 shows the electrodes on the back and front side of a thin quartz crystal, where piezoelectric oscillation is sustained in the center area rather than the rim. In the front view of the QCM crystal surface, the crystal which is exposed to space, senses molecular flux (mainly the contaminant molecules), where the added mass as a form of contaminant thickness will change the period of oscillation of the crystal (i.e. the frequency shift). The propagation wave (transverse shear wave) vibrates in the form of Gaussian distribution in the position where the propagation direction is perpendicular to the electrode plane. This mechanism of the confining field is called energy trapping [35]. Having very little damping of gas or liquid on the transverse wave (shear mode wave) amplitude, yields a linear relationship between the frequency shift and loading mass.

The Sauerbrey equation [36] is used as way of relating piezoelectric crystal oscillation frequency to the mass deposited. The equation is derived by treating the deposited mass as the extension thickness of the underlying quartz.

The frequency to mass relationship is defined:

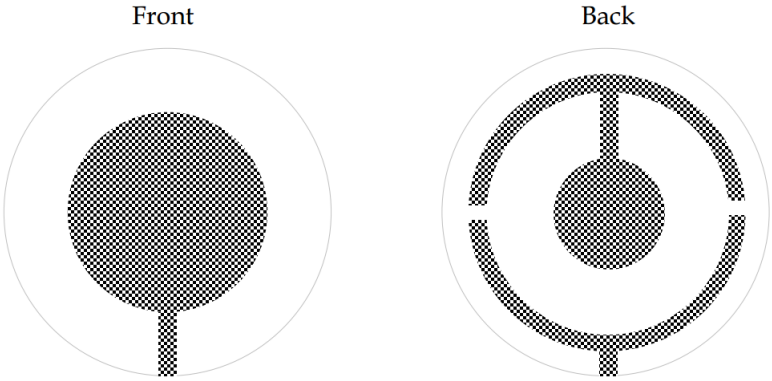

Figure 2.1: Gold electrodes on QCM front and back sides

$$\frac{d(-\Delta f)}{d(\Delta m/A)} = \frac{2f_o^2}{\sqrt{n\mu_q}} = S \tag{2.1}$$

where f_o is the crystal resonant frequency, Δf, is the frequency change, $(\Delta m/A)$ is the mass change on active crystal area, n is the density of the quartz $(2.648 g/cm^3)$, μ_q is the shear modulus of the crystal surface $(2.947 \times 10^{11} g/cm^2)$ and it is related to the crystal stress constants, crystallographic cut angle and temperature, and S is known as the crystal sensitivity.

Calculations of the shear modulus (or shear wave velocity) show the mass sensitivity at $25°C$ differs from the one at $10°K$ by only 0.51%, for which reason the temperature effect on mass sensitivity is always ignored.

At $T = 298°K$,

$$\frac{d(-\Delta f)}{d(\Delta m/A)} = 5.12 \times 10^8 Hz/g/cm^2$$

and

$$S = 1.95 \times 10^{-9} g/cm^2 \cdot Hz$$

Based on the impendence match method, the Sauerbrey equation is valid when

these conditions apply: the deposited mass is rigidly attached and evenly distributed on the surface and the frequency change is less than 0.02%. If the $\Delta f/f_o > 0.02\%$, the small load approximation will not work in this equation, where the inertia effect and viscoelasticity will be used to update the Z-match model [29] [37] [38]. The Z-match model is the Butterworth-van-Dyke (BvD) equivalent circuit and consists of an acoustic branch and electrical branch, where the acoustic impedance has certain relations with the electrical impedance for certain working conditions. The QCM always measures an areal mass density, not a geometric thickness, so the physical density of the film needs to be known in order to obtain thickness.

2.1.1.2 QTGA

In addition, QCM Thermal Gravimetric Analysis (QTGA) is used to identify the deposits constituents by uniformly heating the crystals, which also provides an effective way to clean the QCM surface contaminants before subsequent outgassing tests.

During QTGA tests, as the crystal substrate is heated from a cryogenic temperature (like the liquid nitrogen boiling point), the collected mass will evaporate from the crystal in order of their relative volatilities. The mass remaining on the crystal is measured as a function of frequency versus temperature as the various collected species evaporate over different temperature regimes.

The QCM needs to be heated gradually and slowly (in order of $\sim 2^{\circ}K/min$), so the collected mass remains constant until an evaporation temperature for a specific constituent is reached, thus causing a decrease in frequency. The QCM will respond with an uphill and down peak in outgassing rate (dm/dt). As temperature rises through time, the QCM will continue to produce this rise and fall in rate at the various temperatures until the collected mass is completely evaporated.

2.1.1.3 QCM components

The QCM used in the following experiments is from QCM Research Corporation, which specializes in manufacturing thermoelectric QCMs (tQCM), cryogenic QCMs (cQCM), passive QCMs and control data acquisition units. The exposed piezoelectric sensor crystal, vibrating at approximately 15MHz, responds to a deposition of mass on the crystal by shifting frequency.

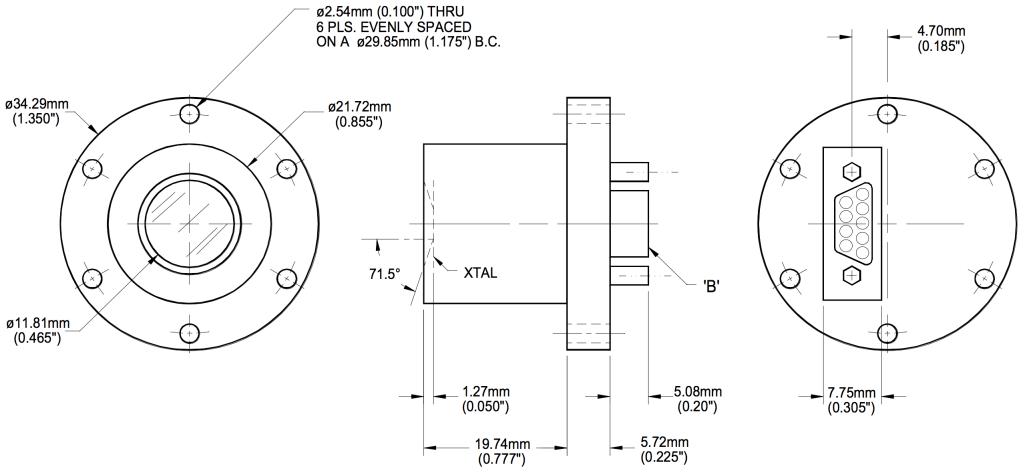

Figure 2.2: MK18 Configuration

From the schematic of the model MK18 cQCM in Fig 2.2, the QCM has an azimuthal angle of 71.5° limited by its mechanical structure, the operating temperature range is limited by the heatsink temperature and it is passively cooled due to its resistive crystal heating. There is another reference crystal with the same specification hidden underneath the sense quartz crystal to eliminate any temperature fluctuation effects.

2.1.2 Spectroscopic ellipsometry

In spectroscopic ellipsometry, optical constants and film thicknesses of samples are determined from the change in the polarization state by light reflection over a wide range of wavelengths and at one or multiple incident angles [39].

Initially the optical interference can be utilized as a simple way to understand how phase difference is a function of incident angle, thickness, light wavelength, etc..

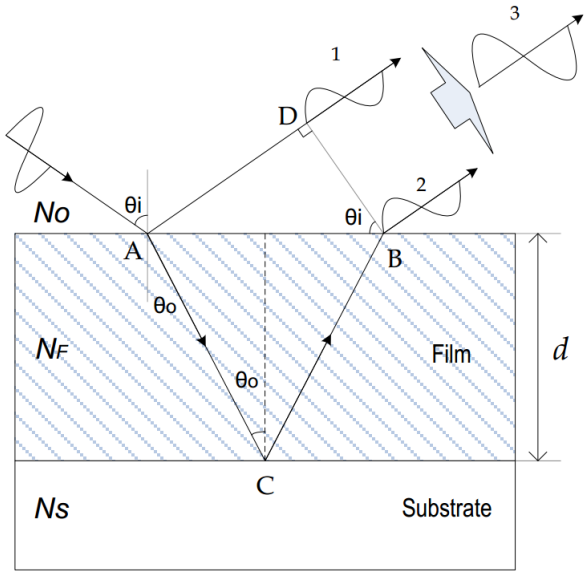

Figure 2.3: Optical interference in a thin film

Measuring the thickness of a thin film on a substrate can be deduced from the optical interference illustrated in the Fig 2.3. The reflected beam (*primary1*) and the transmitted beam (*secondary2*) overlap into form of beam *3* which has a larger electric field amplitude (if the two beams have the same phase) or smaller electric field amplitude (if the two beams are out of phase). The phase difference can be explained by the optical path difference between $(\overline{AC} + \overline{CB})$ and $\overline{AD}$ shown in the equation below,

$$\alpha_{1,2} = K_F(\overline{AC} + \overline{CB}) - K_O\overline{AD} \tag{2.2}$$

where $K_i = \dfrac{2\pi N_i}{\lambda}$ is the propagation number for beam *1* and beam *2*.

By using Snell's law, the secondary beam (*3*) shows a total phase difference of the form below

$$\alpha = \frac{4\pi d N_F}{\lambda} cos\theta_o \tag{2.3}$$

As seen from equation 2.3, in a thin film/substrate structure, if assuming that the phase difference α induced by this optical interference corresponds to Δ observed in ellipsometry, knowing the thickness of the film, the optical constant N_F can be derived, or vice versa.

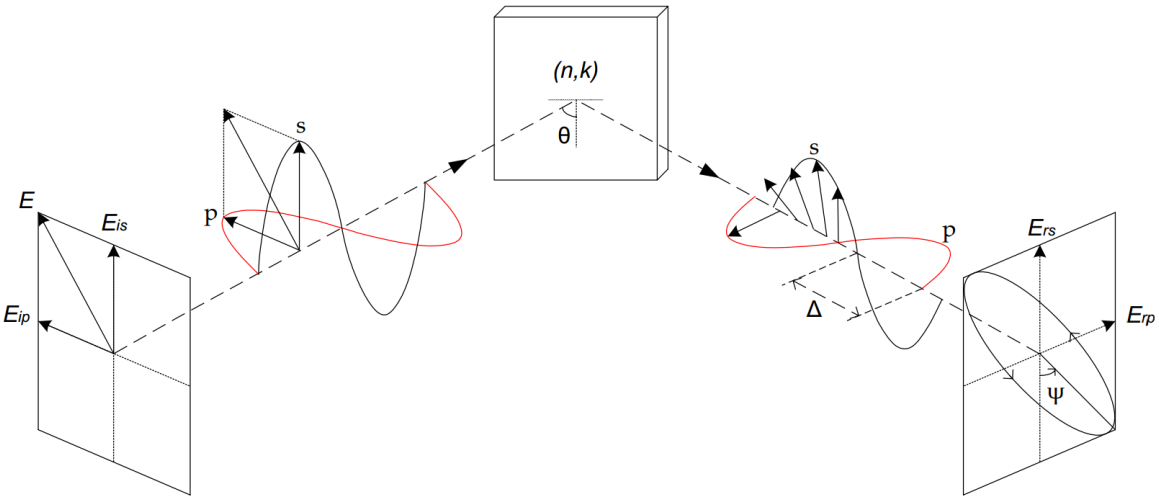

Figure 2.4: Measuring principle of ellipsometry

Fig 2.4 illustrates the measurement principle of ellipsometry, the polarization states of incident and reflected light waves are described by $p-$ and $s-$ polarizations (parallel to and perpendicular to the plane of incidence). In this figure, the incident light is linear polarized with an orientation of $+45°$ to E_{ip} axis. The ampli-

tudes of $p-$ and $s-$ polarizations are the same ($E_{is} = E_{ip}$) and the phase difference between them is zero.

Upon reflection from a sample, polarizations are changed in amplitude and phase in the directions of both $p-$ and $s-$. As show in Fig 2.4, the reflected light wave converts into elliptical polarization. The two values (Ψ, Δ) measured present the amplitude ratio of the Fresnel reflection coefficients r_p and r_s and phase difference between $p-$ and $s-$ polarizations, respectively.

The raw ellipsometric data is related to the ratio of complex reflection coefficients, which defined as:

$$\rho = \frac{r_p}{r_s} = tan\Psi exp(i\Delta) \tag{2.4}$$

The optical constants and thickness cannot be solved in analytical fashion. Given initial standard deviation estimates (δ_Ψ and δ_Δ) for the measured Ψ and Δ, pairs of Ψ, Δ values are calculated for the measured wavelengths and angles of incidence. By varying the model parameters, the mean-square error can be reduced then minimized using Levenberg-Marquardt algorithm, which in the form of weighted test function below,

$$\zeta^2 = \frac{1}{2n-m} \sum_{j=1}^{n} \left\{ (\frac{\Psi_j^{ca}(\mathbf{x}) - \Psi_j^{me}}{\delta_{\Psi,j}})^2 + (\frac{\Delta_j^{ca}(\mathbf{x}) - \Delta_j^{me}}{\delta_{\Delta,j}})^2 \right\} \tag{2.5}$$

where n is the measured $\Psi - \Delta$ pairs, m is the number of fitting parameters, $\mathbf{x}$ is a vector with m components including thickness,

Sellmeier coefficients, Ψ^{me}, Δ^{me} and Ψ^{ca}, Δ^{ca} are measured and calculated data, respectively.

Then the optical constants and thickness can be obtained as a result of regression fit from the figure of merit.

In this work, the RCE (rotating compensator ellipsometer) has been utilized to

measure the ellipsometric data. The optical configuration of the ellipsometer is shown in Fig 2.5

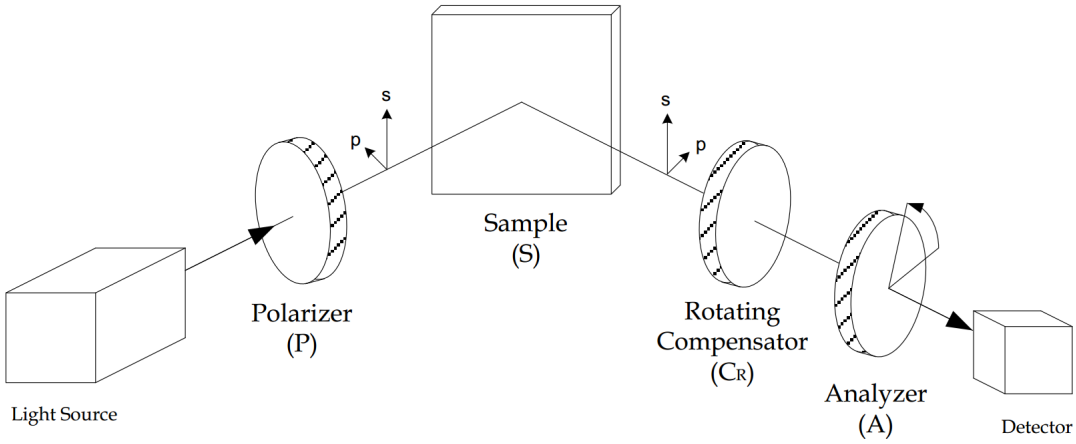

Figure 2.5: Optical configuration of RCE

This rotating-compensator ellipsometry (PSC_RA) consists of basic polarization components including a polarizer, compensator and analyzer.

The polarizer extracts linearly polarized light from unpolarized light (light source like halogen bulb). Commonly, a polarizer consists of calcite prisms. Such polarizers like the Glan-Taylor prism is used in the $\lambda = 0.21 - 5\mu m$ region because of its low extinction ratio ($\kappa \sim 10^5$). For the deep UV region ($\sim 6eV$), Rochon prisms made from MgF_2 and quartz can be used for a polarizer.

The compensator is used to convert linear polarization into circular polarization or vice versa. A compensator also requires optical anisotropy and is composed of a birefringent crystal. The compensator with phase difference of $\delta = \pi/4$ is called a quarter-wave plate. When rotating in the $s-, p-$ polarization plane, the relative phase difference can be changed. Thus, in this case, it can be called a rotating compensator. The compensator is usually made from MgF_2 and mica for their ultra low light transmittance in the UV region.

Finally, the table listed below shows the strengths and drawbacks by using spectroscopic ellipsometry as a characterization method[39].

Table 2.1: Strengths and drawbacks of SE

Strengths:	Nondestructive to measured sample Materials range from metal to polymers Characterizations for optical constants and film thickness High precision sensitivity for thickness ($\sim 0.1\mathring{A}$) Real-time monitoring
Drawbacks:	Indirect characterization (optical model built before analysis) Data analysis tends to be complicated Thickness and Δ are entangled in ultra thin film regime Difficulty in the characterization of low absorption coefficients

Chapter 3

Experimental Apparatus and Procedure (Cryogenic Temperature CVCM Deposition)

The lifetime of space systems and space-level sensors can be significantly degraded by contaminants. One of the major contaminant sources is outgassing products from structural materials, and design analyses must be conducted in order to ensure that this source is reduced to an acceptable low level. In order to perform these analyses it is necessary to know the outgassing behavior of these materials. The ASTM E-1559 standard has been used to determine the in-situ outgassing rate, as well as TML and VCM value for years at NASA/Goddard Space Flight Center (GSFC). In our cyogenic experimental system, not only has the QCM been used to determine the outgassing rate and deposition of contaminants, but also in-situ ellipsometry has been used to investigate the optical effects of the deposited contamination on sensitive spacecraft surfaces.

3.1 Chamber Setup

The experimental chamber setup referred to as the Contamination Analysis Test Chamber (CATC), is shown in Fig. 3.1. The lower level of this chamber contains the contamination source for creating the flux of outgassing material for collection

on a QCM surface or test sample surface. The source comprises a vapor effusion cell (VEC) made of copper with an electrical resistance heater silver soldered to the outside of the cell, and a type E thermocouple soldered to the outside of cell. The thermocouple is connected to a Micromega CN77300 thermal controller which drives a solid state relay that controls power to the heater. The orifice of the VEC lies in a plane with the QCM surface or test sample surface, and these two planes are coaxial, the QCM and VEC are exaggerated in this schematic, the actual distance between these two planes is around 13 inches. The form factor (i.e. view factor) and converting coefficient for outgassing rates will be calculated in the following sections. A shutter is installed in lower level of the chamber and can be adjusted by an air side knob. This shutter can used to cut off molecular flux to the QCM surface or test sample surface. The whole experimental chamber is surrounded by a cryogenic shroud which can attract excess source molecular flux not directly incident on the collecting surface. The pipelines that encircle the chamber wall can be temperature controlled by a circulating fluid. The chamber can be maintained at or near room temperature.

Solid materials can be outgassed or vaporized in the VEC, which is constructed of a copper alloy. The VEC is fastened by a series of ceramic rods to the flange in the lower part of chamber. The heater surrounding the VEC is capable of 30 watts power output which can support the temperature of the VEC up to 200 °C. The VEC itself is 45mm inner diameter, 47mm external diameter and 90mm tall. The cured silicones were cut into cubes of approximately 0.25 inches in dimension. At a distance of 13 inches from the opening of the VEC is the test sample surface and QCM. The QCM is bolted by its heat sink through the hole in the liquid nitrogen filled shroud, which is represented by the shadowed area in Fig. 3.2 (shows lateral view and vertical view of QCM housing). The shroud within the CATC is a bell shaped

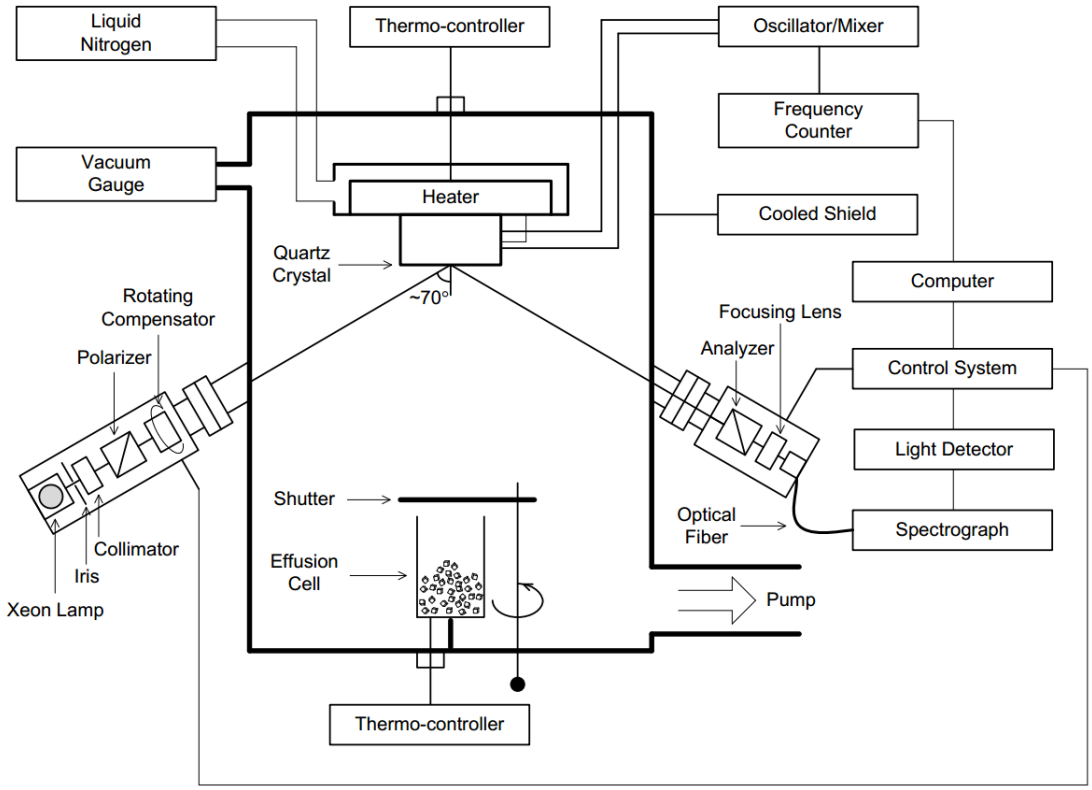

Figure 3.1: Schematic of Contamination Analysis Test Chamber

liquid nitrogen container which can be sustained at temperature $-180°C$ and below. The copper case of the QCM can be held at cryogenic temperature while the crystals are heated to the desired temperature via the in-situ heater. The crystal temperature can range from 84K to 400K. The QCM views the VEC orifice through a shuttered hole permitting the impinging outgassing flux to be interrupted when needed. In this Mark 18 model QCM, two crystals are used (sense and reference) in a crystal pack (gold plate OFHC copper), which is supported from the base by four heat-isolating struts, the sense temperature is measured by a cryogenic temperature silicon diode in a four-wire electrical circuit. This allows the heater (25 Watts wire-wound precision resistor) to raise the temperature of the crystal pack using 3.6 watts of power. The temperature can be increased to measure the mass change rate (frequency rate of

change) as a function of the sense temperature allowing QCM thermogravimetric analysis (QTGA) to be performed. The bell-shaped cooling shroud traps the non-targeting source outgassing flux and helps to reduce the background outgassing rate to an undetectable low level.

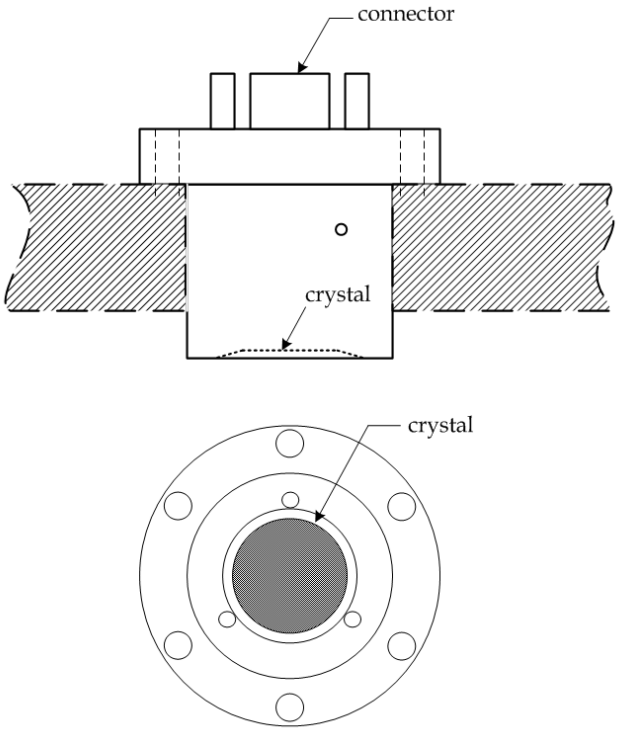

Figure 3.2: QCM Diagram with Shroud

The contamination film thickness can be calculated if the film density if known. Typically, the film density is unknown, but it is usually assumed to be $1.0 gm/cm^3$ to facilitate the calculations.

3.2 Sample preparation

The main material being tested was RTV 566, a two component room-temperature vulcanizing (RTV) silicone rubber, a methyl-phenyl compound, produced by the Momentive. Processing of material includes mixing, DE aeration, curing and cutting.

RTV 566 part-A (base compound) and RTV 566 part-B (curing catalyst) were poured into an aluminum foil boat (diameter of 50mm and depth of 15mm). The amount of RTV 566 part-B is commonly 0.1% mixed with part-A by weight. A 40 gram silicone batch was produced in the foil boat. The purpose of the low percentage catalyst is to extend the curing time and give entrapped air enough time to escape. The process of mixture and weighting were done within the case of a precision digital scale (the accuracy can reach up to 0.0001 gram). The micro capillary tube or clean cotton swab end was used to stir thoroughly the RTV base compound and catalyst, the sides and bottom of the aluminum foil boat were scraped carefully to produce a homogeneous mixture and yield less entrapped air. Air entrapped during mixing needs to be removed to eliminate voids in the cured product. A roughing pump is used to expose the mixed material to a moderate vacuum, where degassing is usually complete about two minutes after frothing disappears. RTV 566 silicone rubber compound can be cured sufficiently in 24 hours at 25 °C and 50% relative humidity to allow handling, also the RTV 566 silicone rubber compound can be fast cured in temperature controlled oven at temperature 150 °C for 30 minutes. The oven used in these experiments is a Thermolyne Type 1300 Furnace with accurate temperature control. The cured rubber was cut into cubes of 0.25 inches in dimension by a clean razor blade, and then transferred into the cleaned VEC for outgassing experiments. One batch of silicone rubber was repeatedly tested in the VEC for several runs under different test conditions. The outgassing rate decreased noticeably with time if the sample was stored at room temperature before vacuum exposure, usually to reduce this effect, tested samples were wrapped within aluminum foil and were stored in a refrigerator between the end of curing and the beginning of vacuum exposure.

3.3 Test procedure

The VEC loaded with the test material was installed in the lower part of the chamber, the cap of the chamber with the bell- shaped LN2 container was then lowered down to seal the chamber. After a 5 minutes evacuation with the roughing pump to 5×10^{-2}torr, the pressure was low enough for the turbo pump to be operated. The final pressure was below 5×10^{-6} Pa measured by hot-filament ion gauge outside the chamber. The chamber was pumped overnight before liquid nitrogen filling in. Fig. 3.3 is the schematic of the LN2 auto-filling system within the CATC. The auto-fill system includes a capacitance-based cryogenic liquid level sensor and Model 185 controller from AMI company. The cap on left side of the schematic is the air/nitrogen relief cap, it needs to be removed before the LN2 is filled in since air within the thin pipe and LN2 shroud will be trapped. The QCM was cooled to below 100K in about 5 hours. The VEC was pre-heated to reach the particular test temperature while the shutter was on to block the outgassing flux. The heating wires around the outside of the chamber and the internal high-power light bulbs were heated to drive off water vapor and small molecules attached on the wall of chamber. This took around two hours for the heating procedure, depending upon the VEC and QCM temperature difference from the ambient. The VEC was again heated up to 100 °C and stabilized in 45 minutes, meanwhile, the QCM crystal was heated up to 95 °C for 15 minutes and then cooled down to the desired test temperature, for example, -153 °C or 120K. When the beat frequency stabilized at the desired temperature (with fluctuation of ± 0.1°C), the shutter opened and the QCM began to collect the outgassing flux, the QCM frequency was recorded as a function of time, the in-situ ellipsometer began to collect raw ellipsometric data (Ψ, Δ) as a function of time.

When a substantial deposit was observed on the QCM crystal through the monitor

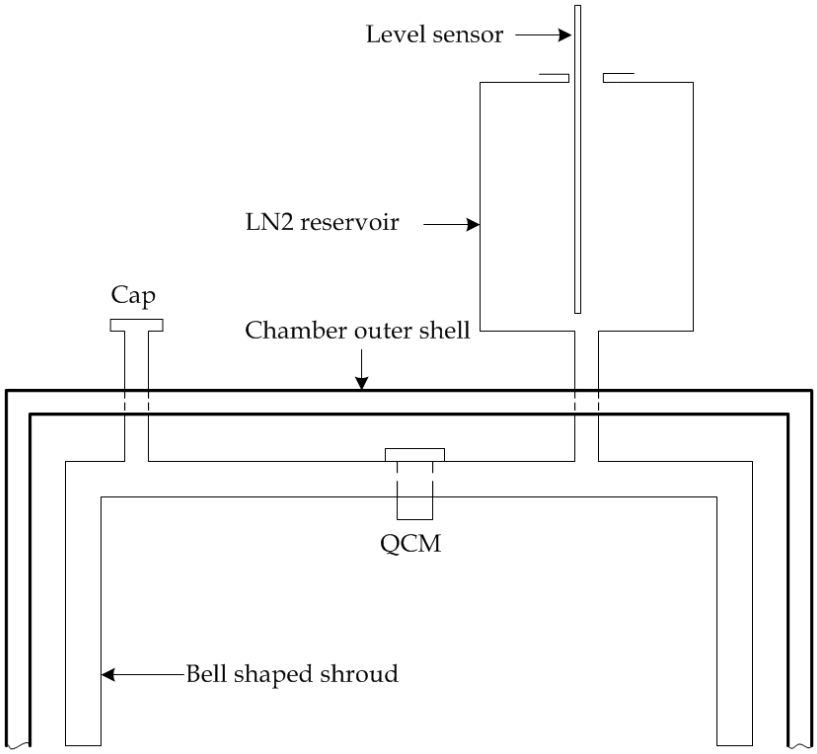

Figure 3.3: LN2 tank coupled with QCM

program on computer, the shutter was closed the VEC turned off and the QCM was heated up from the cryogenic temperature slowly in the rate of 2K/min. The QCM frequency was recorded as a function of time and temperature as the condensed deposit re-evaporated from the crystal. When the heat sink of QCM reached 95 °C and no further change in QCM frequency was observed, all of the deposit can be considered as evaporated. The heat sink was turned off, and the QCM was cooled down to another desired collecting temperature, for example, -183 °C or 150K. The VEC was heated up again and shutter was then opened, and the measurement of outgassing rate was resumed.

The outgassing rate decreased over time, the more times the sample was heated, the less deposit it will produce. The duration for each test varied from about one

hour to more than days. As each type of material was done for various required temperatures, the CATC was then warmed back to room temperature and raised to atmospheric pressure, and the sample was removed and stored in a refrigerator in an isolated wrap.

3.4 Data measurement

During all experiments, the measured data include the QCM frequency, time duration of the experiment, the VEC and QCM temperatures, and the ellipsometric data.

The QCM frequency data reflects the mass per unit area collected on the QCM crystal, $(m/A)_q$. This is determined by multiplying the frequency shift by the QCM sensitivity constant, which is $1.96 \times 10^{-9} g/cm^2 Hz$ for the 15-MHz crystal in use. The sample outgassing rate R_{og} is given by

$$R_{og} = (\Delta f/\Delta t) \times 1.96 \times 10^{-9} \times FF \times \frac{\pi L^2}{SA} g/cm^2 s \tag{3.1}$$

where FF is the form factor which is calculated in Appendix A (3.18×10^{-4}), L is the distance from the VEC orifice to the QCM surface ($330mm$), SA is the exposed QCM crystal area ($\pi R_2^2 = 109.36mm^2$)

Equation 3.1 can be regressed to

$$R_{og} = 1.95 \times 10^{-9} (\Delta f/\Delta t) g/cm^2 s$$

Δf is defined as QCM frequency change during time slot Δt. As in QTGA analysis, the evaporation rate (m_e/A) of the collected deposit from the QCM crystal during the warm up procedure can be considered equal to $(m/A)_q$

Chapter 4

Data Analysis (Cryogenic Temperature CVCM Deposition)

Silicone and siloxane rubbers have been widely utilized in space applications, especially for potting and filling components of solar panels. Sunlight and atmospheric gases in space cause the protection materials to degrade.

The organization of Chapter 4 will be as follows:

- In the CATC system, turbo pump is mandatory when using the ECR system for atomic oxygen simulations. However, a series of experiments showed that the turbo pump cannot reduce the water vapor partial pressure to an acceptable level.

- In subsequent experiments, a cryo pump was substituted for the turbo pump. The cryo pump can eliminate water vapor efficiently and fast, allowing accurate QCM data to be collected.

These two kinds of pumps are compared in Table 4.1 below,

Table 4.1: Cryo pump and Turbo pump comparison

	Cryo Pump	Turbo Pump
model	Cryo-Torr 8	TURBOVAC 600 C
Advantages	Very Clean	Full speed obtained quickly
	High Speed	Reactive gas flow allowed
Disadvantages	Requires regeneration	Difficult to maintain
	Low capacity for H_2 and He	Low compress ratio for light gases
Pump Speed	H_2O: 4000L/s	He: 600L/s
	Air: 1500L/s	N_2: 560L/s
	H_2: 2500L/s	H_2: 570L/s

4.1 Pre-outgassing test with turbo pump

Before the silicone materials were tested, the overall cleanness of the chamber was tested.

In this section, the effusion cell was removed from the chamber, and contaminants from the chamber itself, were deposited onto the QCM under standard test conditions. The CATC was pumped down via the turbopump to a base pressure on the order 10^{-6} torr for 12 hours. The contaminants may include water molecules, carbon dioxide, or other small mass molecules.

Assuming homogeneous films and a density of $1g/cm^3$, the thickness of films can be derived by simple calculations. The deposition process was done at several QCM temperatures (T_{QCM}) and each test was over 40 hours in duration.

The data analysis will be divided into two parts, first, QCM data and QTGA data, second, in-situ ellipsometry data during film growth.

The raw QCM data at 120K is shown in 4.1

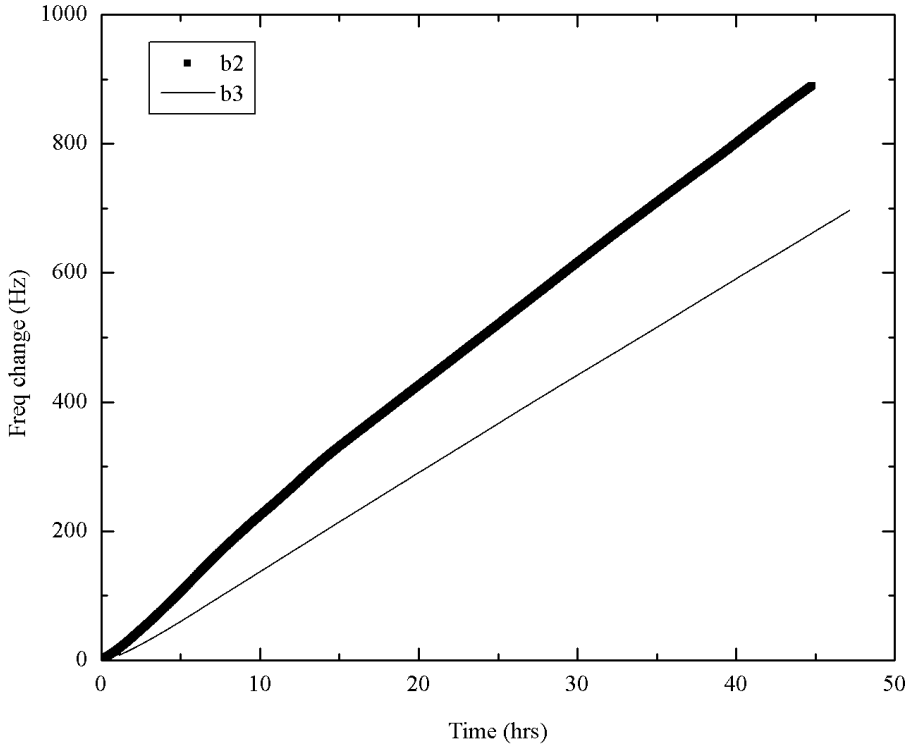

Figure 4.1: QCM deposition raw data in 120K

Data collection under the b3 conditions occurred immediately after data collection under the b2 conditions without exposure of the chamber to air. The thickness of the film collected under b2 was 17.4 nanometers while that of b3 was 13.6 nanometers, based on the density of accumulation being $\rho = 1g/cm^3$.

4.1.1 Ellipsometric data at 120K b-2

The ellipsometer started at 38min for data b-2, and it is assumed that the QCM substrate is free of any deposit at this point in time. The gold electrode on the QCM

substrate is fitted using a B-Spline mathematic model as 'substrate' for the films to grow on. The fitting procedure and fitting results are discussed in below.

1. Open real time ellipsometric measurement data file ended with .iSE suffix in CompleteEase program.

2. Pick the single data when deposition began, un-check 'show dynamic data', fit the data with B-Spline model begin with material 'gold'

3. Save this layer optical constants of B-Spline model as tabulated constants, and use this model as substrate

4. Using the thickness versus time provided by the QCM, and multi-sample analysis, the optical constants of film can be obtained.

The ellipsometric data and fitted data for the substrate at 38min are shown in Fig.C.1, the MSE is 1.107.

For corresponding time slices T_{ei} (ellipsometry) and T_{qi} (QCM), while $1 \leq i \leq n$, the film thickness D_i correspond to the thickness calculated from the QCM frequency shift. Using the multi-sample analysis tool from CompleteEase, the parametric model can be solved from multiple time-slice samples during the growth, where the films at different time-slice are assumed to be optically identical. The time-slice film thickness can be seen from the pancake illustration in Fig. 4.2

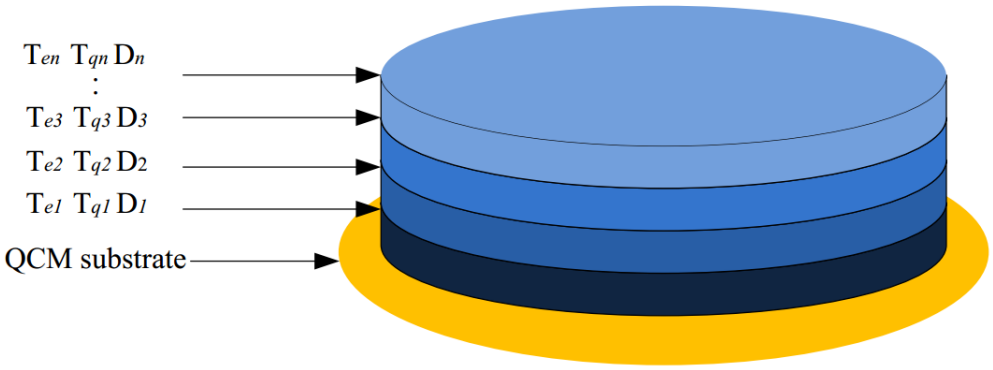

Figure 4.2: Stacked-layer film on QCM substrate

The deposit on the QCM substrate was simplified as a transparent film on the Au substrate. The transparent material is fitted by a Cauchy model for convenience, the general form of Cauchy's equation used in CompleteEase is

$$n(\lambda) = A + \frac{B}{\lambda^2} + \frac{C}{\lambda^4} \tag{4.1}$$

The Cauchy dispersion equation is valid for normal dispersion in regions of visible wavelength. The equation cannot handle anomalous dispersion in the infrared region. A revised Cauchy model is needed for better fitting the ellipsometric data in certain cases.

For the b-2 in-situ ellipsometric data, leaving the default parameters in the Cauchy model (A=1.45, B=0.01), the thickness becomes the only fitting parameter. After clicking 'Fitting dynamic' button, the thickness growth versus time will be calculated. The thickness growth from QCM and ellipsometry are examined in Fig. 4.3

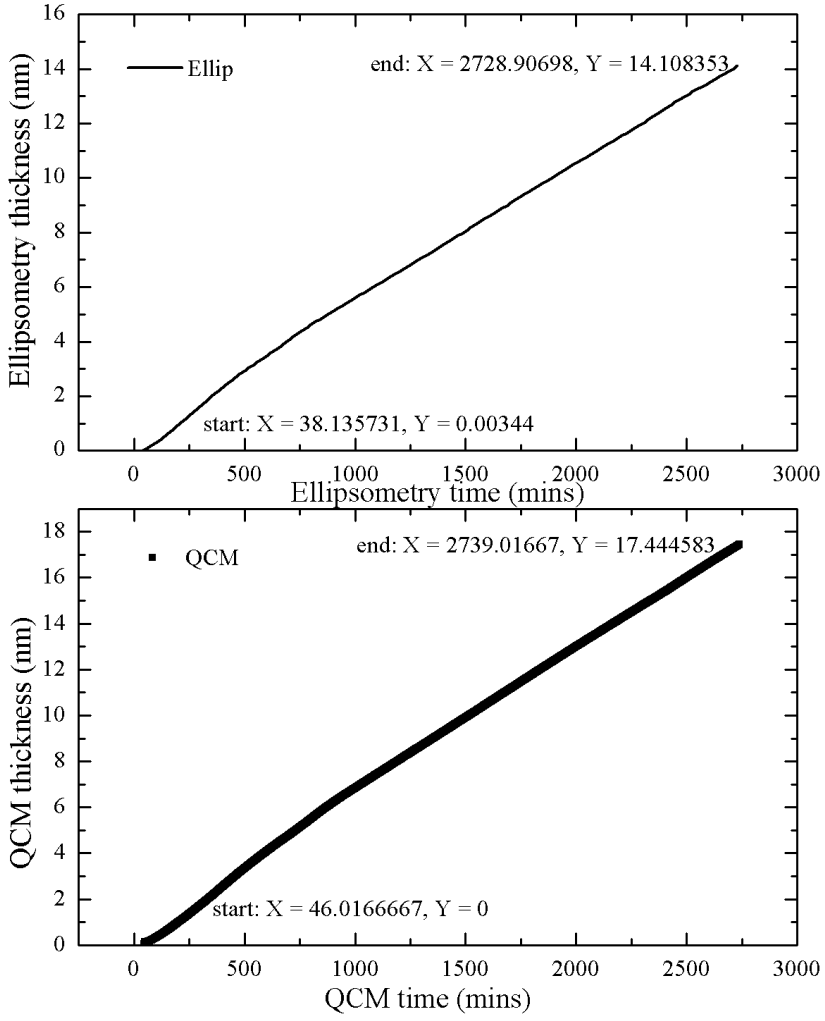

Figure 4.3: b-2 thickness from SE dynamic fitting and the QCM

Regardless of the larger MSE (4.502) at the end of film deposition, the dynamic thickness growth calculated from ellipsometry follows the QCM data almost exactly. In order to obtain Fig. 4.3, each technique employed one assumption, that is, in QCM, when converting from frequency change to thickness, the deposit on the QCM quartz has been assumed to have unity density ($\rho = 1$), while for ellipsometry, the

film is assumed to be homogeneous.

By toggling the value of A to be 1.341 in Cauchy model, the dynamic thickness fitting graph becomes identical with the QCM frequency translation, see Fig. 4.4

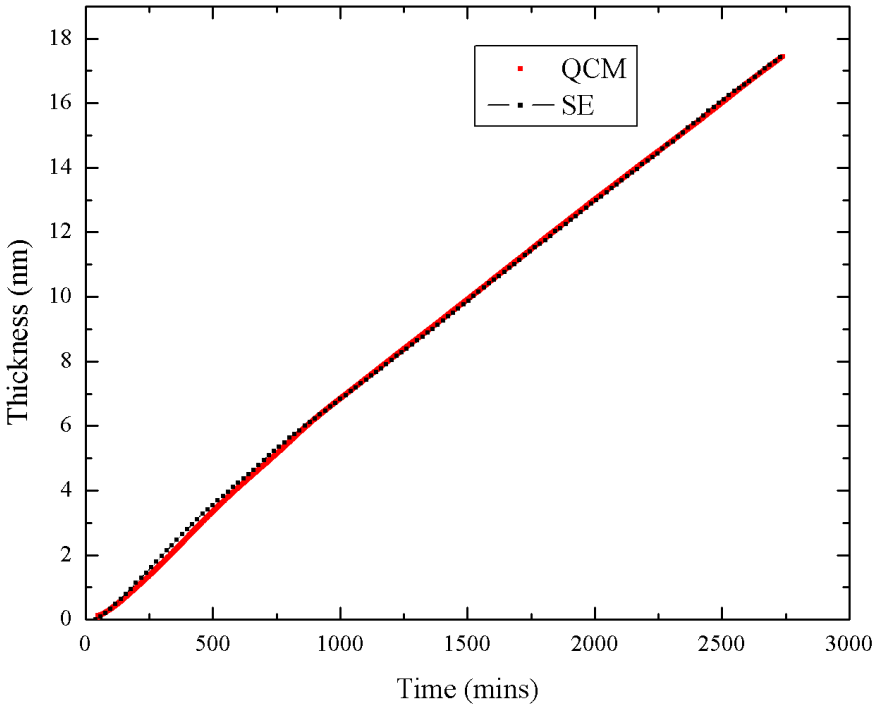

Figure 4.4: b-2 thickness from SE and QCM (A=1.341, $\rho = 1$)

When these two growth rate curves are almost identical, the parameter A in Cauchy model is equal to 1.341, the density of QCM condensation film is 1 which is the same with water ($\rho_{water} = 1$). By examining the refractive index at 589nm, the n of refractive index is equal to 1.369. However, the water deposit would turn into ice at this low temperature (120K), and $\rho = 1$ is no longer valid in this case. The density of the deposit will be revised to be 0.9257 at this temperature[40], then the

thickness based on the QCM conversion will be $\frac{17.43nm}{0.9257} = 18.83nm$. In order for the final thickness calculated from SE to be equal to this value, A needs to be toggled down to 1.309.

By graphing the optical constants from the Cauchy model (Fig. 4.5), it can be seen at 589nm, the refractive index is equal to 1.338 which differs from the ice book value by 0.03. The percentage difference between book value and model value is 2.24%. The deviation of the refractive index may result from the uncertain book value of ice density at 120K. Therefore, the deposited film during 40 hours self-growth deposition is most likely ice.

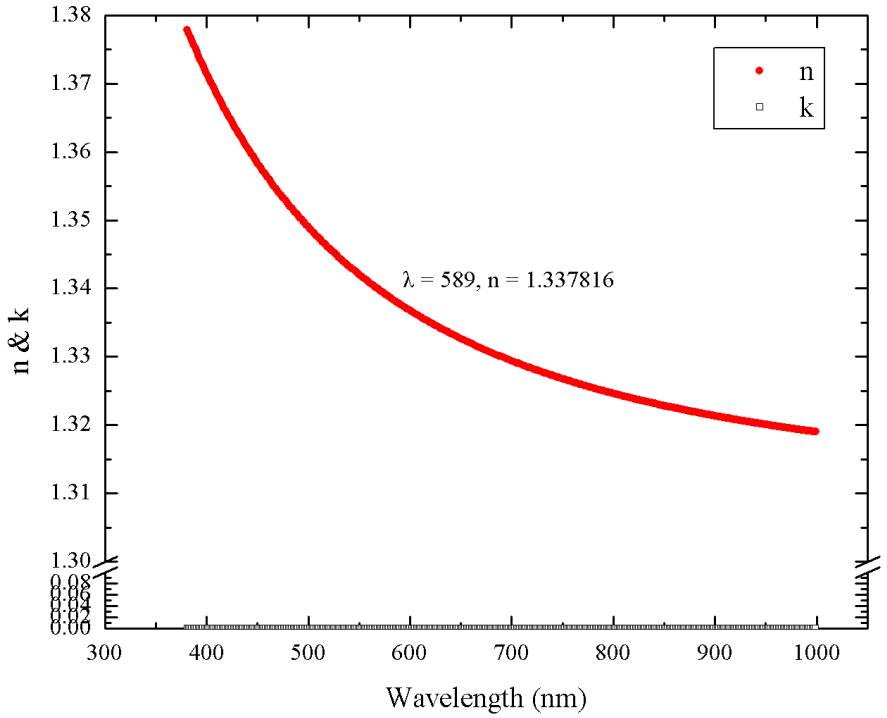

Figure 4.5: b-2 Optical constants of film after applying density of ice

In order to further illustrate data analysis of thin transparent films by combined SE and QCM measurements the Lorentz-Lorenz equation can be employed. In theory, the density ρ and refractive index n can be interrelated by Lorentz-Lorenz equation (also known as Clausius-Mossotti relation and Maxwell's formula). The general form of this equation is followed by below:

$$\frac{n^2-1}{n^2+2}\frac{1}{\rho} = \frac{N}{M} \tag{4.2}$$

When the media is transparent which is assumed so here, the equation will be revised: (reference from [41])

$$\frac{n^2-1}{n^2+2}\frac{1}{\rho} = constant \tag{4.3}$$

The density-temperature relationship for the ice can be expressed as equation 4.4 [42]

$$\rho = -8.133 \times 10^{-5}T + 0.917567 \tag{4.4}$$

where T is in °C. The reference density of ice at different temperatures can be calculated in the table below

Table 4.2: Ice density at different temperature

Temp in C	Temp in K	$\rho(gm/cm^3)$
-153	120	0.93001
-143	130	0.929197
-123	150	0.927571
-60	210	0.922447

The Lorentz-Lorenz equation, when assuming water, yields $\rho = 1$, $\frac{n^2-1}{n^2+2}\frac{1}{\rho} = 0.225912$, when assuming ice, yields $\rho = 0.9257$, $\frac{n^2-1}{n^2+2}\frac{1}{\rho} = 0.225229$, as the film change from water to ice, $\frac{N}{M}$ stays almost constant.

From this equation, it can be seen the density and refractive index are related to each other. When the refractive index changes, the density of the film will follow, or vice versa. Pick a different time slice during film growth, also shown in Fig. 4.2 at (T_{e1}, T_{q1}), (T_{e2}, T_{q2}), ... (T_{en}, T_{qn}), the film grows as a layer-by-layer stack.

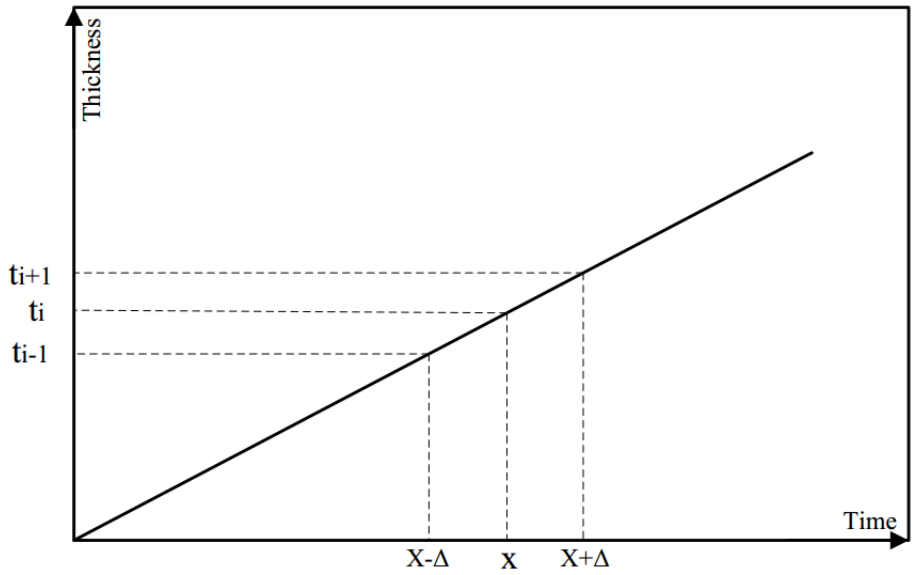

Figure 4.6: Illustration of film growth

From the film growth illustration in Fig. 4.6, at time $x - \Delta$, x, $x + \Delta$, the thicknesses are t_{i-1}, t, t_{i+1} respectively. When Δ approaches a very small value, as compared to the total 1200 minutes, the optical constants (refractive index) and thickness at three different time slice are very close each other, then these values can be considered to be the same. The extrapolation of the Cauchy model (Cauchy parameters A, B and C) can be transformed into the equation array from 4.5. The

thickness can be transformed in the same manner.

$$t_i \rightarrow n(\lambda) = A + \frac{B}{\lambda^2} \tag{4.5}$$

$$t_{i-1} \rightarrow n(\lambda) = A + \frac{B}{\lambda^2} \tag{4.6}$$

$$t_{i+1} \rightarrow n(\lambda) = A + \frac{B}{\lambda^2} \tag{4.7}$$

Solving Cauchy for the parameters A, B and thickness (three unknowns) can be done by means of Multi-Sample Analysis. The procedure is as follows:

1. Extract single point spectroscopic data from dynamic in-situ data, at time slices of which are within 10 minutes interval. (like 178 min, 173 min, 152 min)
2. Make these five data points as independent .SE data file
3. Append these three data into one fitting window, then turn on multi sample analysis
4. Make Cauchy parameters A, B and thickness as fitting parameters within the multi sample analysis
5. A, B and thickness can be then derived

The more fitting data points, the more precise the optical model will be.

4.1.2 Ellipsometric data at 120K b-3

Similar work is done for data b-3 at 120K and d-1 at 150K (shown later). The ellipsometric data for b-3 at 120K was fitted by the same procedure as b-2.

The ellipsometric data and fitted data for the substrate at 38min (the beginning of deposition) are shown in Fig.C.2, the MSE is 0.960.

Leaving the default Cauchy parameters (A=1.45, B=0.01), the dynamic thickness fitting will be calculated and compared to, the QCM frequency translation in Fig. 4.7

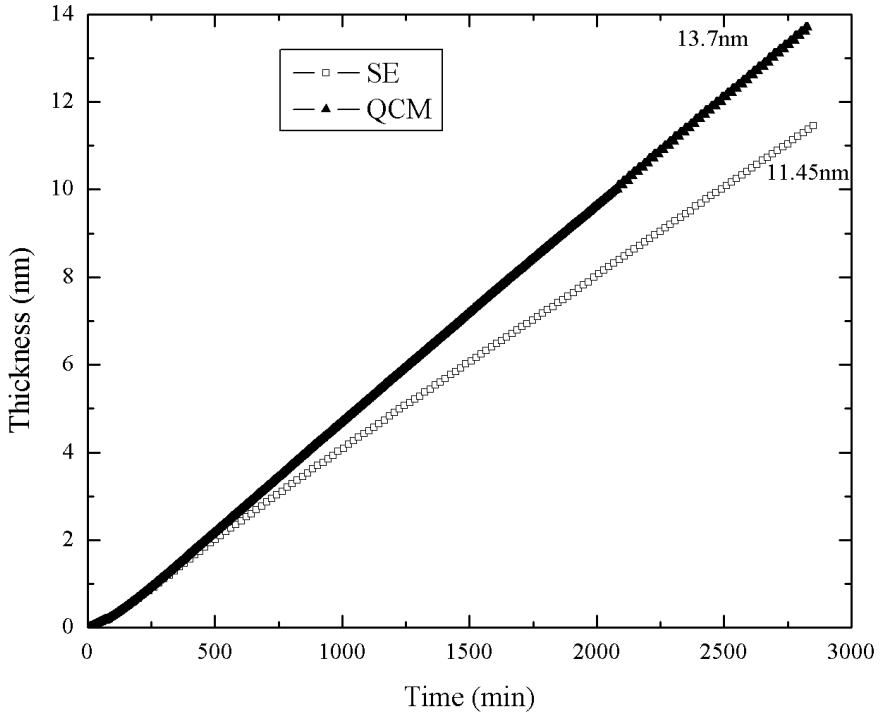

Figure 4.7: b-3 thickness from SE dynamic fitting and the QCM data

The end point thickness for the QCM is 13.7nm, for ellipsometry is 11.45nm. These thicknesses are based on assumption of $\rho = 1$ and $A = 1.45, B = 0.01$. In the real conditions as stated in the b-2 thickness calculation, the density of the film is changed from 1 to 0.9257 at 120K, then the end point thickness of the QCM will be

$\frac{13.7nm}{0.9257} = 14.8nm$. To force the final thickness of SE to be 14.8nm, the value of A needs to be toggled down to 1.319.

The revised thickness with film density and optical constants is plotted in Fig. 4.8. The dynamic thickness growth from ellipsometry overlaps the QCM thickness.

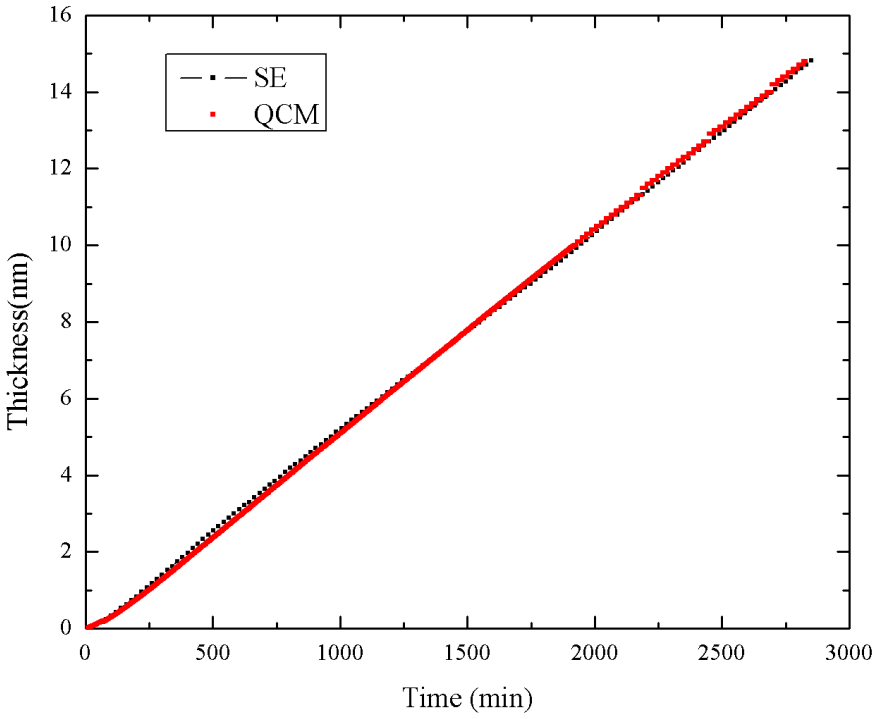

Figure 4.8: b-3 thickness from SE and QCM (A=1.319, $\rho = 0.9257$)

By graphing the optical constants from the Cauchy model in b-3 (Fig. 4.9), the refractive index at 589nm is 1.347 which differs with ice index book value by 0.04.

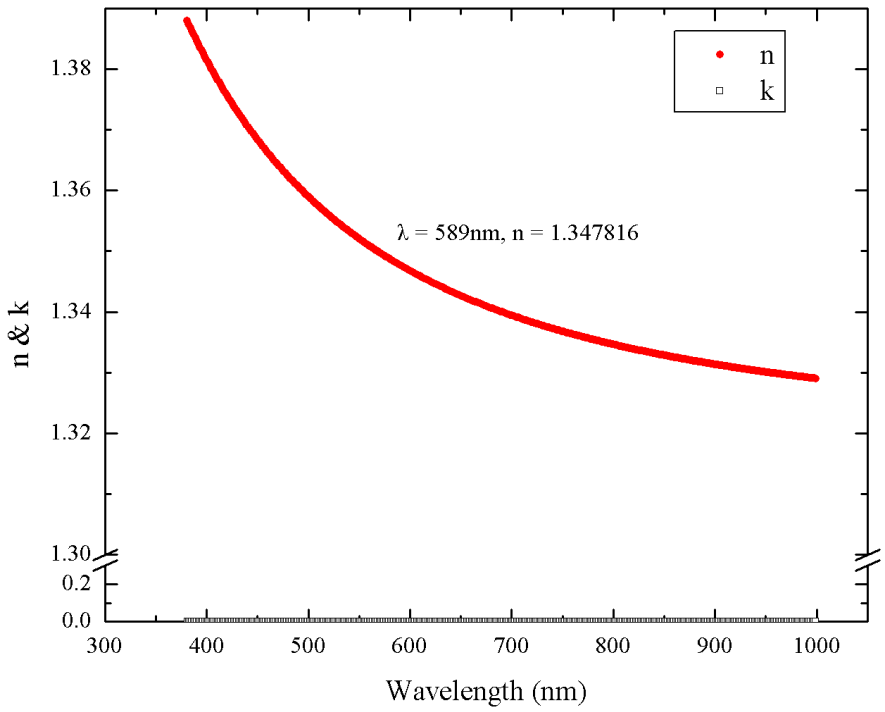

Figure 4.9: b-3 Optical constants of film after applying density of ice

4.1.3 Ellipsometric data at 150K d-1

Taken from the Table 4.3, d-1 represents the self-deposition at 150K in chamber. The ellipsometric data started from 84min, at this time, the substrate for d-1 is fitted as below (Fig. C.3). The MSE is 1.128.

Leaving the default Cauchy parameters (A=1.45, B=0.01), the dynamic thickness fitting will be calculated and compared to the QCM frequency translation in Fig. 4.10. At the end of deposition, the thickness of QCM is 7.99nm while the thickness fitted by ellipsometer dynamic is 7.39nm. Also, if the density of the film is revised from 1 to 0.927 at 150K. Then the thickness of QCM will be $\frac{7.99}{0.927} = 8.619nm$. By

toggling the value for A in ellipsometry, the thickness will be 8.619nm when A is set to 1.364. The thickness growth with revised density and A is plotted in Fig. 4.11.

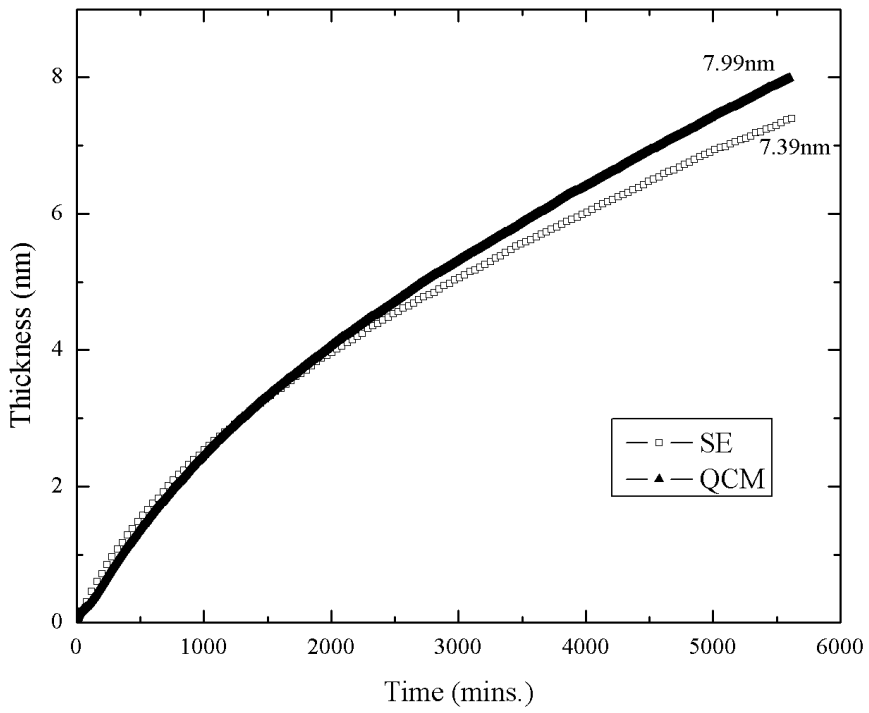

Figure 4.10: d-1 thickness from SE dynamic fitting and the QCM data

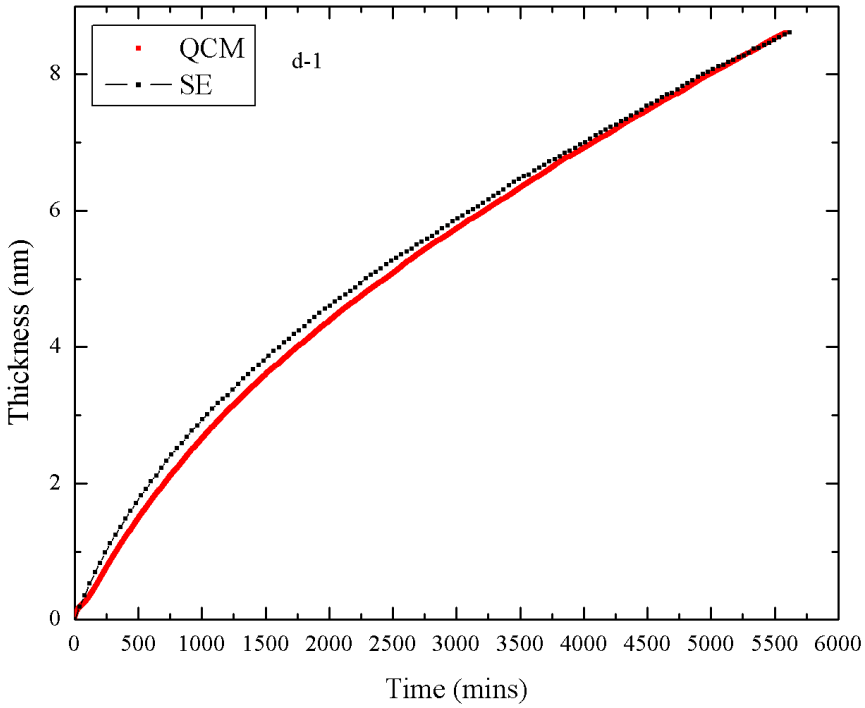

Figure 4.11: d-1 thickness from SE and QCM (A=1.364, $\rho = 0.927$)

Comparing the growth rate at 120K (Fig. 4.4 and Fig. 4.8), to that at 150K the deposition took more time to reach a steady growth rate, furthermore, the growth rate at 150K is half the one at 120K. In the same vacuum condition, the deposition is much less at a higher QCM deposition temperature.

The optical constants with revised film density and Cauchy parameter A are plotted in Fig. 4.12.

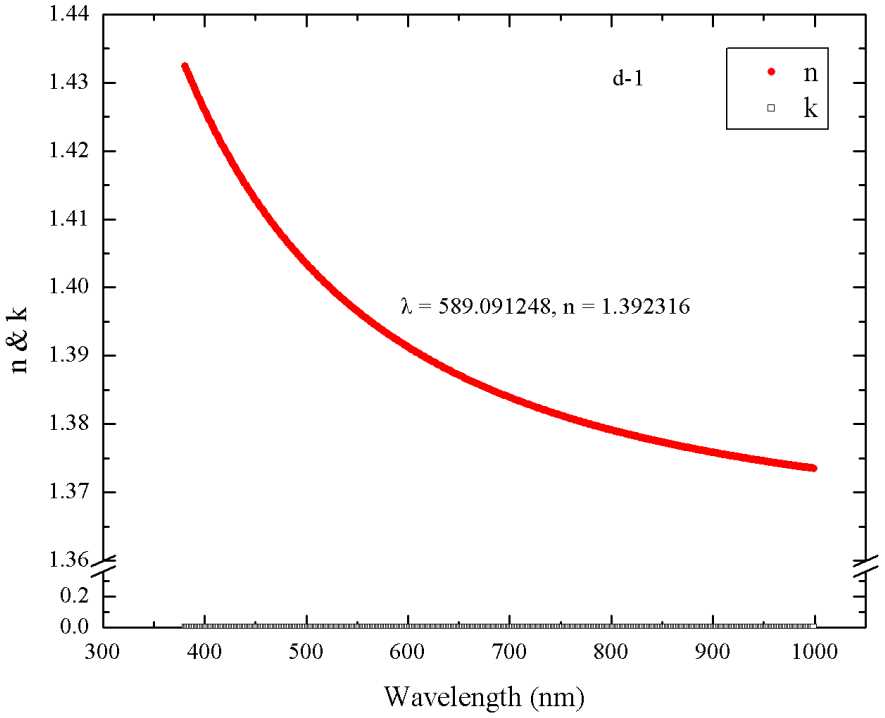

Figure 4.12: d-1 Optical constants of film with revised density and A

With the same fitting procedure, the refractive index is 0.05 larger at 150K which indicates the deposition is denser.

Similar depositions has been done at temperature 210K and 130K. These data sets are shown in Table 4.3

Table 4.3: Mass Accumulation from chamber residue with turbo pump without outgassing

date	data	temperature	duration	thickness	film growth rate
3-14	a-1	210K	40 hours	2.15nm	0.05375nm/hr
3-18	a-2	210K	37 hours	1.23nm	0.03324nm/hr
3-21	b-1	120K	44 hours	2.15nm	0.04886nm/hr
4-2	b-2	120K	45 hours	17.6nm	0.39111nm/hr
4-12	b-3	120K	47 hours	11.42nm	0.24297nm/hr
4-15	c-1	130K	47 hours	2.94nm	0.06255nm/hr
4-20	d-1	150K	43 hours	4.43nm	0.10302nm/hr
5-23	b-4	120K	41.5 hours	11.22nm	0.27036nm/hr
5-26	d-2	150K	36 hours	3.22nm	0.08944nm/hr

Comparing the data b-2, b-3 at 120K and d-1 at 150K deposition, the refractive indices at 589nm are shown in Table 4.4

Table 4.4: Refractive index comparison of self-contaminant films at different condensation temperatures

	Temperature	n
b-2	120K	1.3378
b-3	120K	1.3478
d-1	150K	1.3923

When the turbo pump is used to evacuate the system, there was mass accumulation on the QCM substrate. Within 50 hours, the thickness growth on the QCM substrate is in the order of tens nanometers at 120K while less than five nanometers at higher temperatures like 150K and 210K.

Using the calculation methods in this section, the accumulation species were shown to be water ice due to the close values in refractive index. In order to minimize contamination of this kind, the cryo-pump was used instead of the turbo pump.

4.2 Pre-outgassing test with the cryo pump

The preparation procedure with the cryo pump is the same as with the turbo pump before the deposition experiments can proceed. As the chamber vacuum was around 10^{-6}torr, the self growth started at 120K.

Assuming the density of the film to be $1gm/cm^3$, the QCM thickness growth at 120K is shown in Fig. 4.13

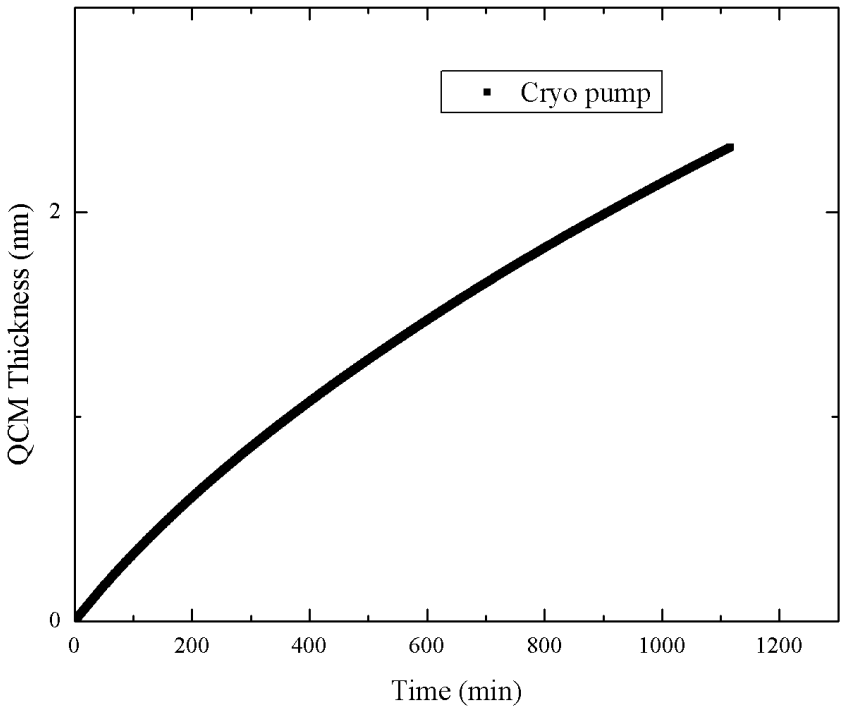

Figure 4.13: Thickness from QCM frequency convert

During 1100 minutes of growth, the QCM data indicate the thickness growth is 2.31nm. By examining the in-situ ellipsometric data, there is no obvious change in Ψ and Δ through the whole 1100 minutes deposition.

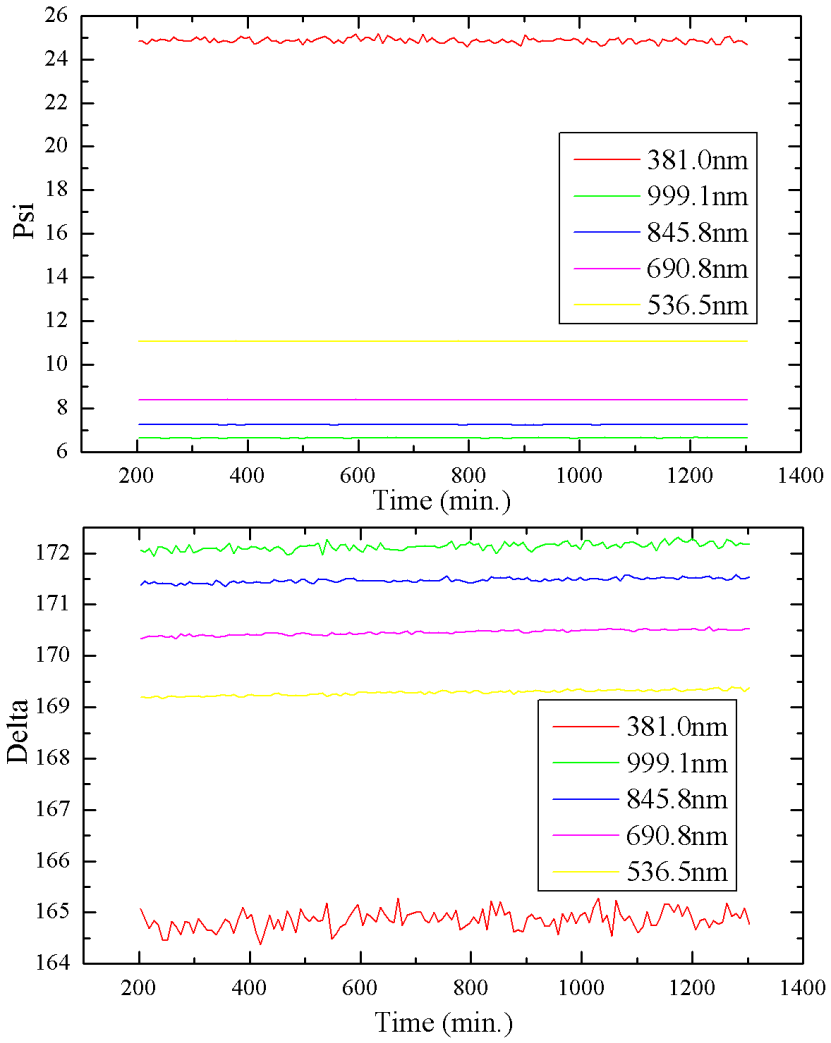

Figure 4.14: Dynamic SE data at 120K Cryo Pump

Using the same model as before (Cauchy layer + B-Spline substrate). The dynamic thickness is rarely changed through the deposition, see Fig. 4.15

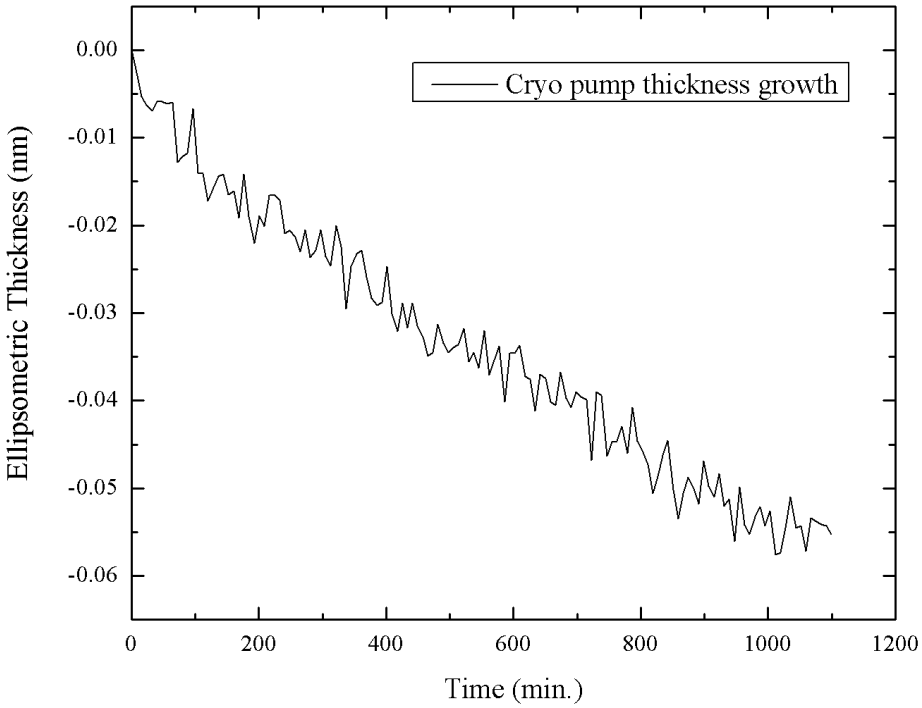

Figure 4.15: SE dynamic thickness fitting at 120K Cryo Pump

By using the cryo pump, there is no thickness growth indicated by in-situ ellipsometry. The thickness growth from the QCM may indicate frequency fluctuation with time. Due to the water vapor pumping capability of the cryo pump, ice condensation has effectively been eliminated.

Chapter 5

Data Analysis (RTV Outgassing)

With the help of the cryo pump, the water vapor in the system is kept to a low level. Nonetheless, the water molecules trapped within the silicone rubber are still a potential contaminate source when the silicone rubber is exposed to air.

The volatile components of the RTV materials are outgassing and condensing on the QCM substrate at cryogenic temperatures. The condensation mechanism is a complex process which is not investigated in this thesis. This work focuses on the optical properties of the condensed film. The reddish silicone material analyzed here is RTV566.

From previous research on photo-fixed VCM films [43], it is anticipated that the condensed VCM films are thin and weakly absorbing films.

Since the VCM film condenses at cryogenic temperature it cannot be removed from the chamber. Therefore *in-situ* ellipsometry and QCM measurements are employed to characterize and quantify the films.

The test list for RTV566 VCM are listed in Table 5.1

Table 5.1: RTV566 Tests List

Date	Label	Temperature	Duration	Thickness	Rate
1-31	r-l2-1	120K	73 hours	16.1nm	0.22 nm/hr
12-15	r-l5-1	150K	75 hours	11.4nm	0.15 nm/hr
1-12	r-l8-2	180K	72 hours	9.3nm	0.13 nm/hr

5.1 RTV566 QTGA Data

Before analyzing the optical constants of the films, the QTGA data is shown here to illustrate any potential difference in film composition across the condensation temperature range.

The procedure to derive the QTGA data is as follows: When the deposition is at a specified QCM temperature (for example 120K), the QCM substrate was heated up from that temperature, the VCM re-evaporates from the QCM substrate. The QCM substrate is heated up to 40°C or above at a specified ramp rate (2°C/min) which is precisely controlled by the QCM wired circuits. A plot of frequency change versus temperature can be obtained. The derivative of the frequency change versus temperature yields the QTGA plot. After the completion of the data collection, a bakeout temperature of 95°C will allow the QCM substrate to clean itself by driving off the residues on the substrate. There was no vacuum break from 120K deposition to 180K deposition.

The evaporation rate for films deposited at the three temperatures is shown in Fig. 5.1.

From the FTIR analysis of the outgassing of RTV566 material in flowing nitrogen[43], PDMS (polydimethylsiloxane) and NPS (Tetra-n-propylsilicate) are the main outgassing products. The humps from the QTGA data may come from these materials.

The QTGA data for the film condensed at 120K differs from those condensed at 150K and 180K. The characteristic peak seen around 273K is the largest peak observed from the 120K film, which is more than likely water. The water peak is not apparent in the other two films. Another characteristic peak around 140K does not exist in the 150K and 180K QTGA data. The 150K and 180K VCM apparently have very similar composition since they share almost the same characteristic peaks around 220K and 300K evaporation temperatures.

Therefore, due to the suspected ice peak for 120K VCM, the optical constants of 120K VCM should be different from 150K VCM and 180K VCM. The 150K VCM and 180K VCM may share some similarities in optical constants.

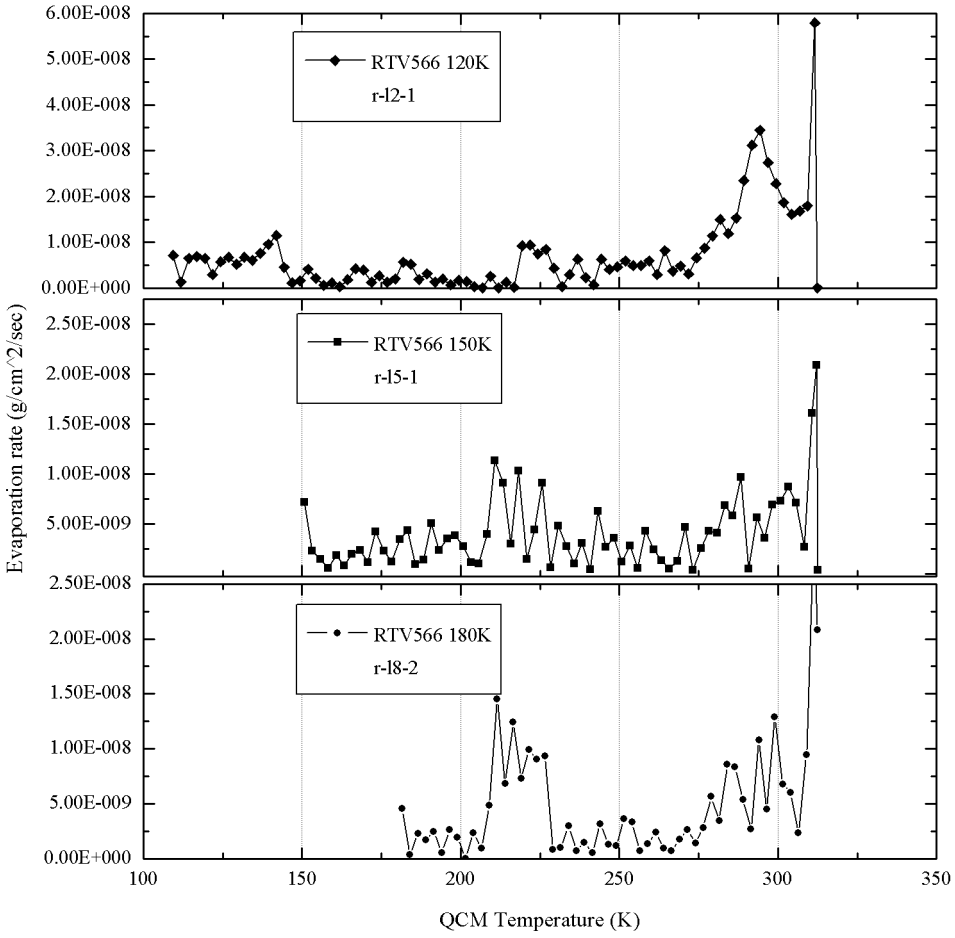

Figure 5.1: Evaporation rate of long duration RTV566 from QTGA

5.2 Initial Analysis for RTV566 VCM

In this section, basic optical models are employed for ellipsometric data analysis. The models are based on the assumption that all these VCM films are homogeneous at 120K, 150K and 180K respectively.

5.2.1 RTV566 120K VCM

The VCM film deposited at 120K will be analyzed in this section. Assuming the density of the film to be $1gm/cm^3$, the film deposited on the QCM substrate is approximately 18nm thick and accumulated over 73 hours.

The QCM thickness is then plotted in Fig. 5.2.

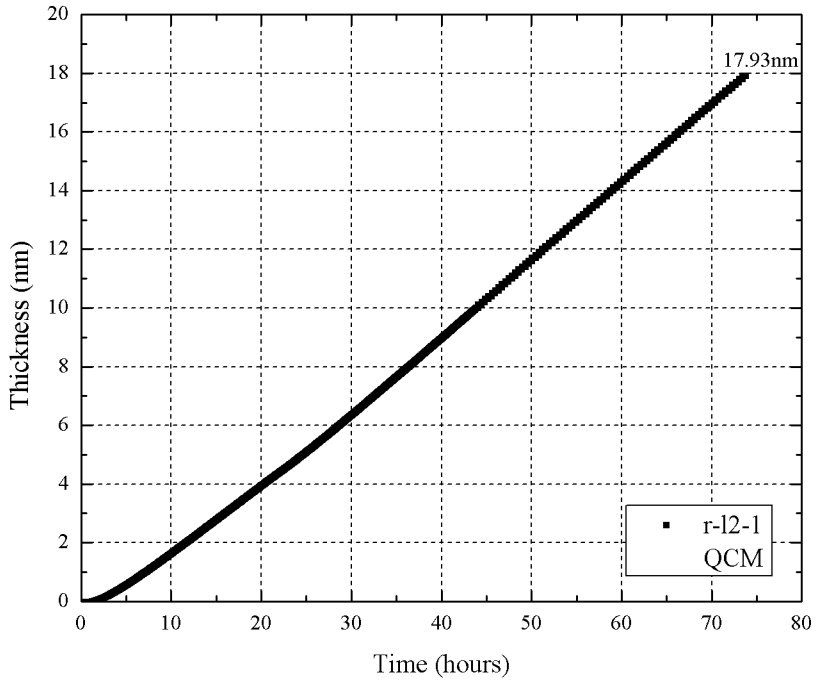

Figure 5.2: r-l2-1 QCM thickness versus time

From the QCM figure, the mass deposition rate is quite linear throughout the whole deposition except during the early stage of deposition. Although not definitive, the linear growth suggests a homogeneous film density.

5.2.1.1 RTV566 120K Cauchy model

The simplest optical model, the Cauchy model, is employed to fit the end point SE data. The QCM substrate is nominally Au and is fit on a B-Spline model. The Cauchy model on the B-Spline substrate is used to derive the optical constants where the film thickness is fixed at the QCM thickness (17.93nm).

The model for the end point SE data is shown in Fig. 5.3

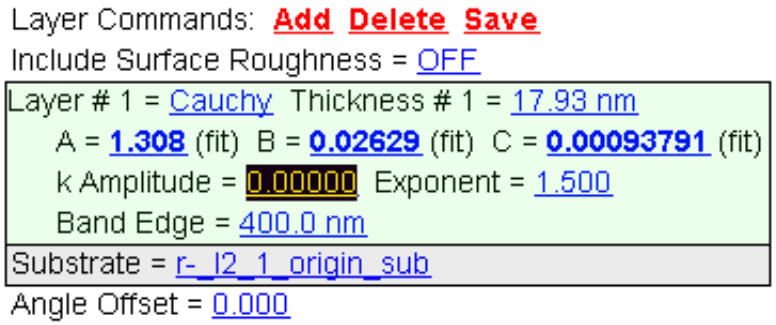

Figure 5.3: RTV566 VCM Cauchy model at end point SE data

The fitting results for the end point SE data are shown in Fig. 5.4

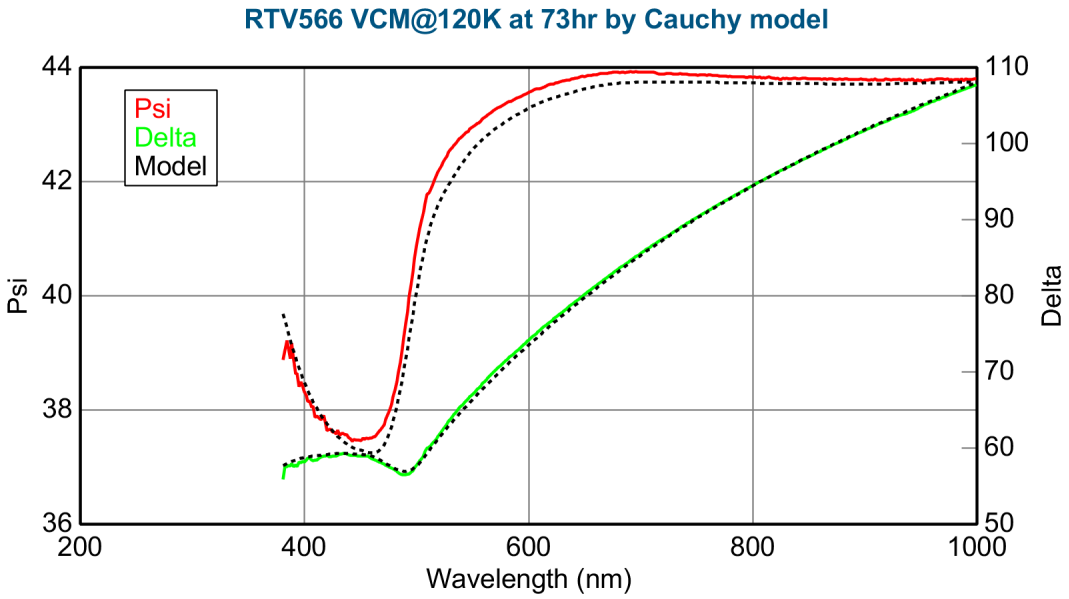

Figure 5.4: RTV566 120K VCM end point fitting by Cauchy model

The MSE is 6.598 which is not considered to be an adequate fit to the data.

5.2.1.2 RTV566 120K Gen-Osc model

As seen from previous section, the Cauchy model is not a good fit to the end point SE data. In view of this, the more sophisticated Gen-Osc is employed to achieve a better fit. The general oscillator model employs basic oscillators to fit the dielectric constants for materials. For polymer materials, the molecular oscillation within the VCM film may be fit by the Gen-Osc model.

The fitting procedure is illustrated in Fig. 5.5

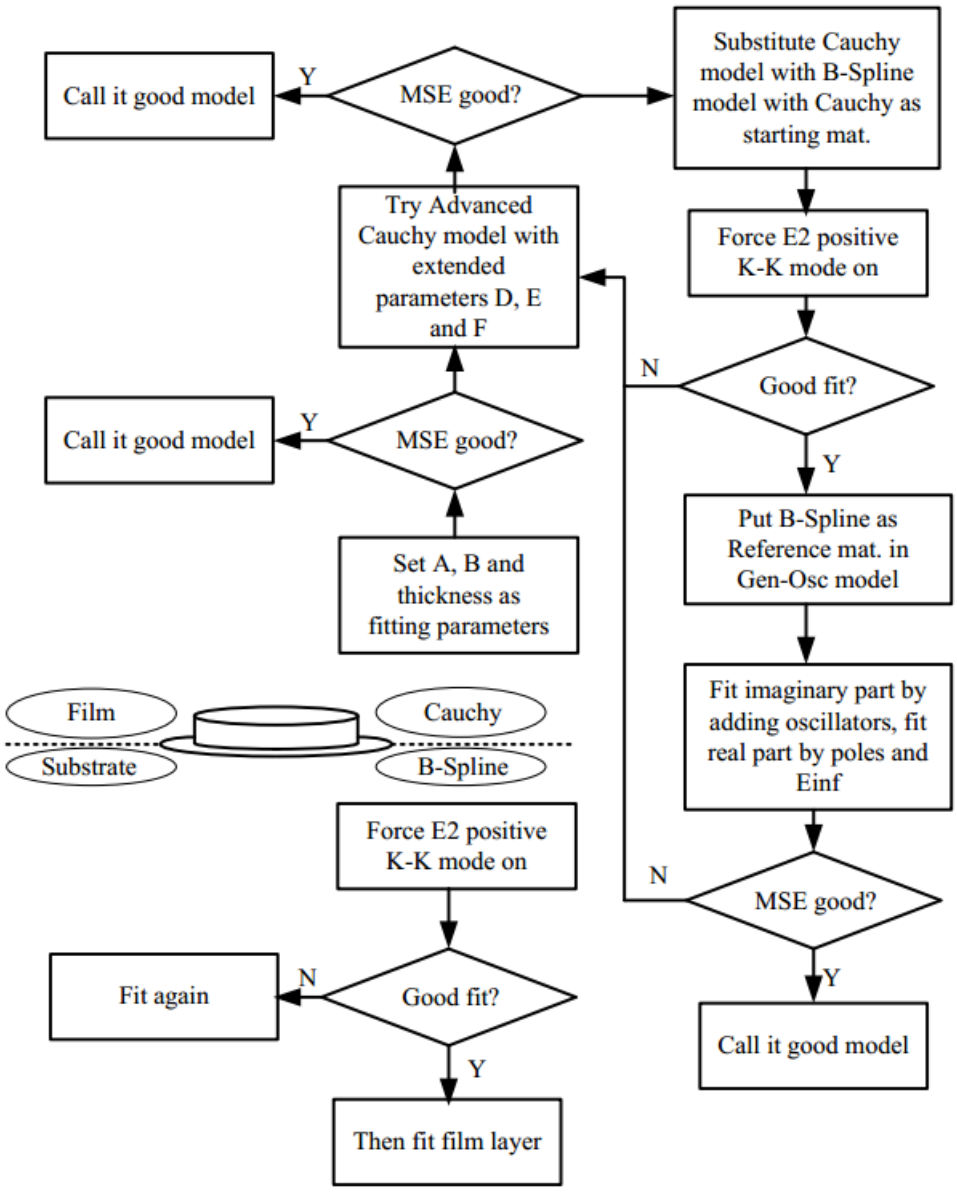

Figure 5.5: Gen-Osc model fitting procedure

By fixing the end point thickness to be 17.93nm, the optical constants derived from the Gen-Osc model are shown in Fig. 5.6

Layer Commands: Add Delete Save
Include Surface Roughness = OFF
Layer # 1 = Gen-Osc Thickness # 1 = 17.93 nm
Add Oscillator Show Dialog Fast Gaussian Calc = ON
Einf = 0.000 (fit)
UV Pole Amp. = 73.7575 (fit) UV Pole En. = 6.850 (fit)
IR Pole Amp. = 0.1008 (fit)
Fit All Clear All Add Amp. Add Br. Add En.
1: Type = Gaussian Amp1 = 0.416962 (fit) Br1 = 0.3596 (fit) En1 = 2.509 (fit)
2: Type = Lorentz Amp2 = 0.347665 (fit) Br2 = 0.3668 (fit) En2 = 2.897 (fit)
3: Type = Lorentz Amp3 = 0.480249 (fit) Br3 = 0.4460 (fit) En3 = 3.262 (fit)
Substrate = r-_I2_1_origin_sub
Angle Offset = 0.000

Figure 5.6: RTV566 VCM Gen-Osc model at end point SE data

The model consists of one Gaussian oscillator and two Lorentz oscillators. The fitting results for the end point SE data by the model is shown in Fig. 5.7.

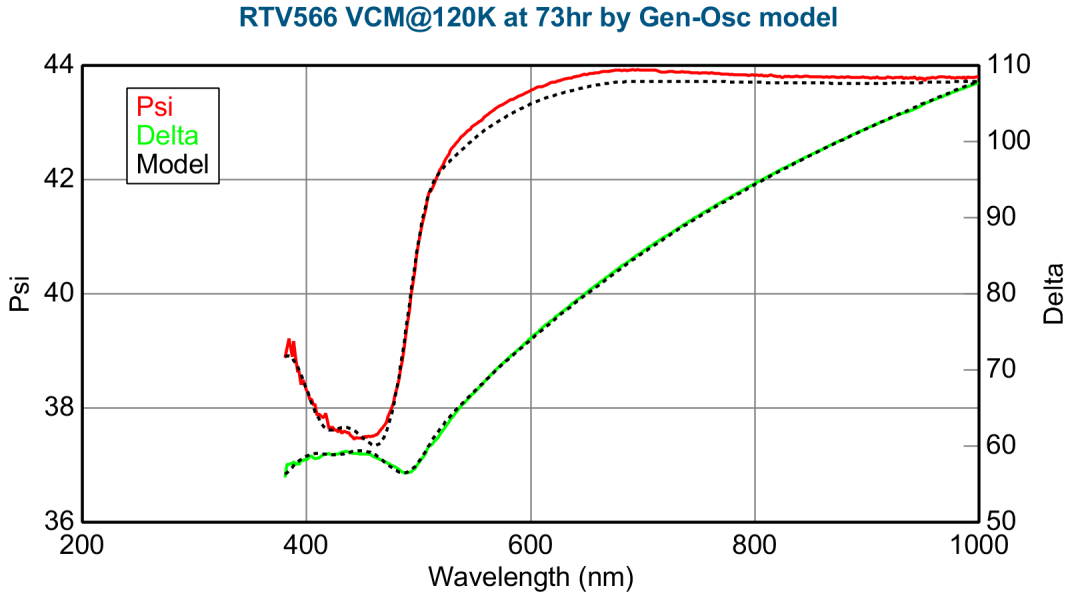

Figure 5.7: RTV566 120K VCM end point fitting by Gen-Osc model

The MSE is improved (3.958) over the Cauchy model. However, there still exists

an offset between the Gen-Osc model and the experimental SE data for Ψ.

The optical constants derived from Gen-Osc model at the end point are shown in Fig. 5.8

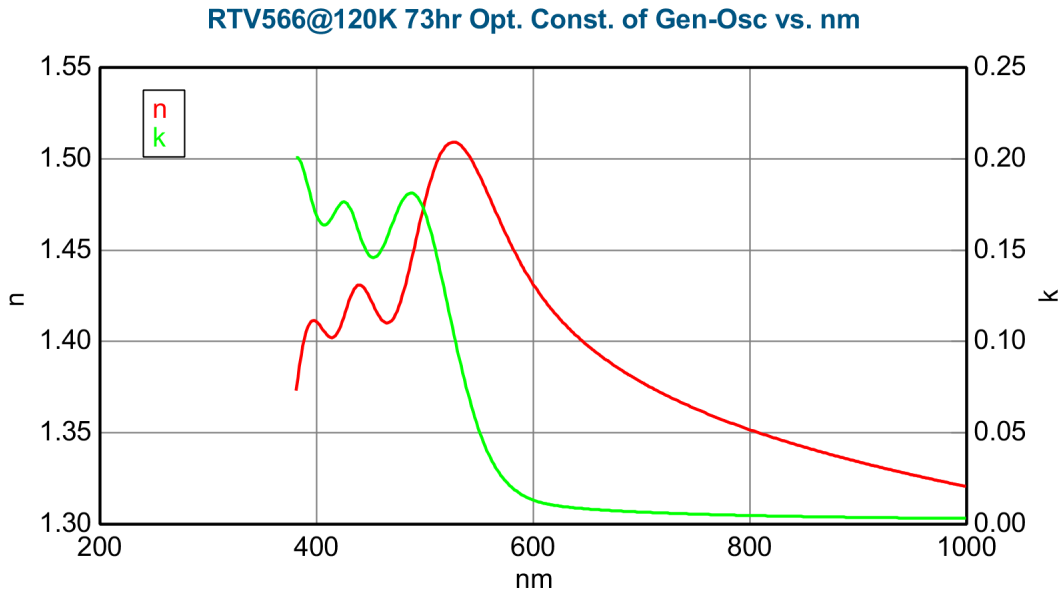

Figure 5.8: RTV566 120K VCM end point optical constants by Gen-Osc model

If this model is accurate and the film is homogeneous, fitting the real time SE data using this model and calculating the thickness should yield a low MSE at every point in time and a film growth curve that matches the QCM curve.

The thickness at multiple time points and fitting MSE are shown in Table 5.2

Table 5.2: RTV566 VCM film thickness at 120K fitted by end point gen-osc model optical constants at each time point

Time Slice	Fitted Thickness (nm)	MSE
10	0.67	1.642
20	2.75	1.788
30	4.88	2.108
40	7.60	2.475
50	10.59	3.035
60	13.63	3.427
70	16.67	3.795

Figure 5.9 is a graph of the SE derived thickness growth curve and the QCM thickness growth. The SE and QCM thickness are in reasonable agreement over the entire process with a small offset especially at the early stages of deposition. However, the MSE does increase with time.

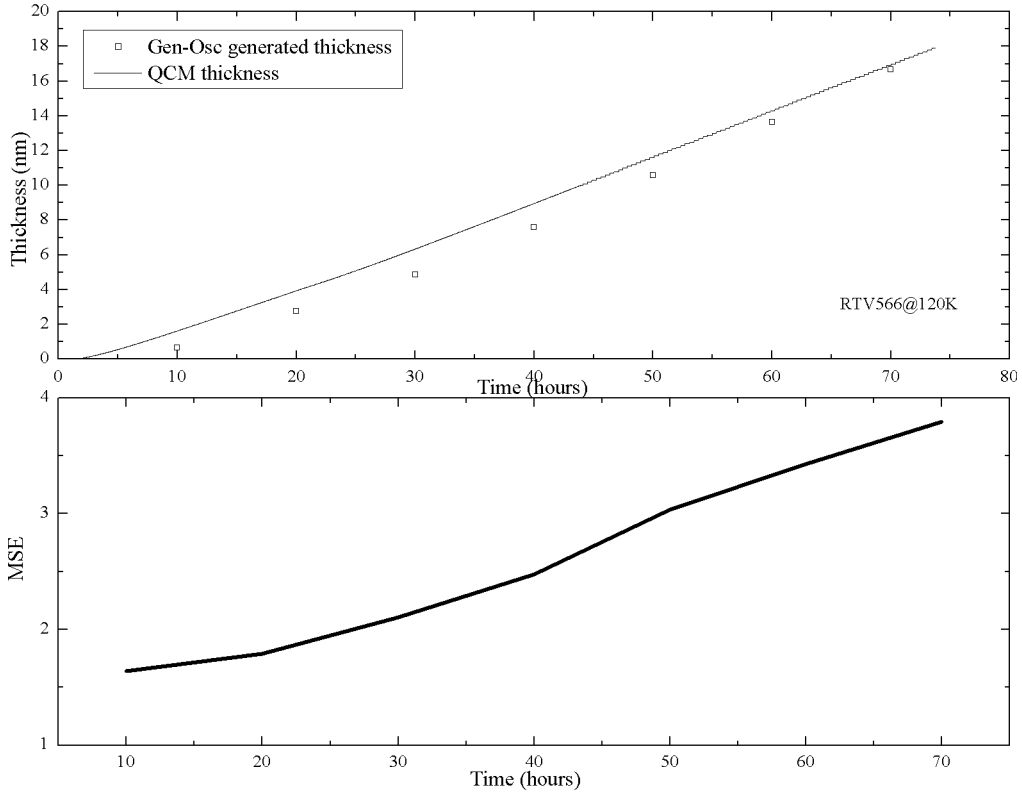

Figure 5.9: RTV566 120K VCM thickness at multiple time points with QCM thickness

5.2.1.3 RTV566 120K WvlByWvl model

The Gen-Osc model calculated at the end point does provide a reasonably good fit to the data over the entire deposition process. This is good indication that the film is homogeneous, however it does introduce oscillations in the ellipsometric parameters that are not present in the data.

In order to further improve the fit, the end point data is modeled using the point by point approach.

The Gen-Osc model is a physical and Kramers-Kronig consistent model which can describe various types of materials including polymers and organic films, however, the information from the ellipsometric data is so complex that the Gen-Osc model with

several oscillators cannot precisely fit the data.

A 'wavelength-by-wavelength' (also refers as 'point-by-point') fit is performed for each wavelength which is independent from all other wavelengths of the spectrum to extract the dielectric constants from the experimental data [44]. The point-by-point fitting can provide minimum fitting error, however, point-by-point fitting needs a physical connection to the measured data, otherwise, random measurement error from point-by-point fitting will contribute to the derivation of dielectric constants. In some case, Kramers-Kronig consistency will force the model to have some physical meaning to avoid systematic errors [39].

The point by point approach is applied in the following manner:

- Select the end point ellipsometric data for 'r-l2-1', choose 'WvlByWvl.mat' for film layer, force E2 to be positive
- Fix the thickness value from the QCM thickness, then fit the optical constants.
- Save the 'WvlByWvl' layer optical constants as the end point optical constants.
- Select other time point SE data, choose the film layer from previously saved end point optical constants.
- Fit the only parameter 'thickness', and do the same procedure to fit other time point's thickness.

The optical constants at the end point fitted by 'WvlByWvl' are shown are Fig. 5.10

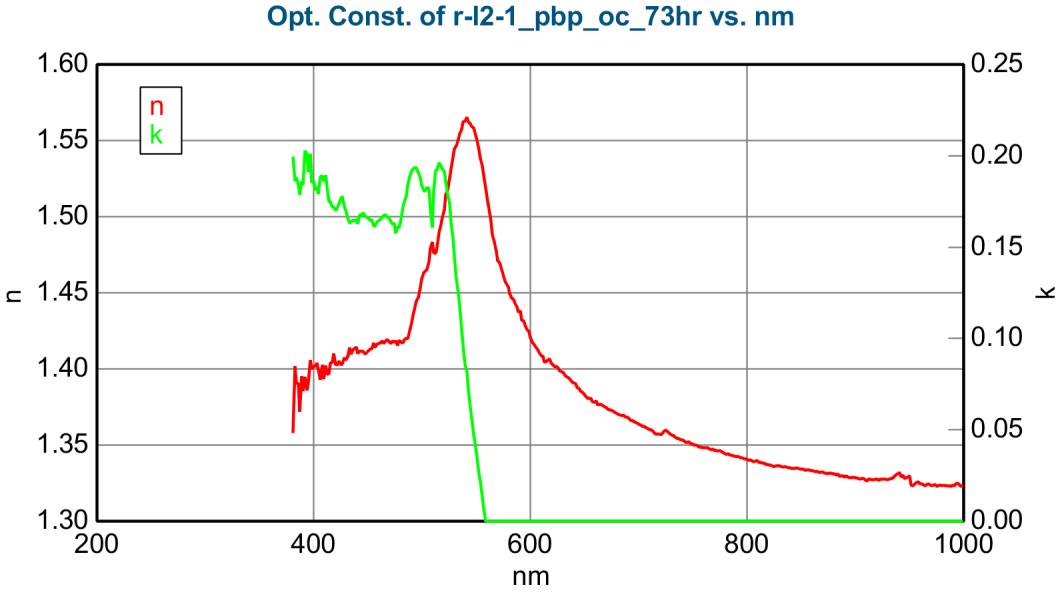

Figure 5.10: End point optical constants of RTV566 at 120K deposition

Observing the optical constants derived from the end point SE data, the optical constants from 'wavelength-by-wavelength' fitting have a similar wavelength dependence and similar n/k values as compared with the ones derived from the 'gen-osc' model which has physicality. However the oscillations in the short wavelength region have been substantially reduced. Thus, the 'wavelength-by-wavelength' fitting is preferable in modeling the end point optical constants for 120K VCM.

By substituting the end point optical constants into other time slices, the thickness will be obtained. These time slices include '10hr', '20hr', '30hr', '40hr', '50hr', '60hr', '70hr'. The fitting MSE and thickness are shown in Table 5.3

Table 5.3: RTV566 VCM film thickness at 120K fitted by end point optical constants at each time point

Time Slice	Fitted Thickness (nm)	MSE
10	0.66	1.577
20	2.79	1.582
30	4.96	1.664
40	7.74	1.778
50	10.79	2.038
60	13.88	1.926
70	16.97	1.968

The SE data fitting results for each time slice is shown in 5.11.

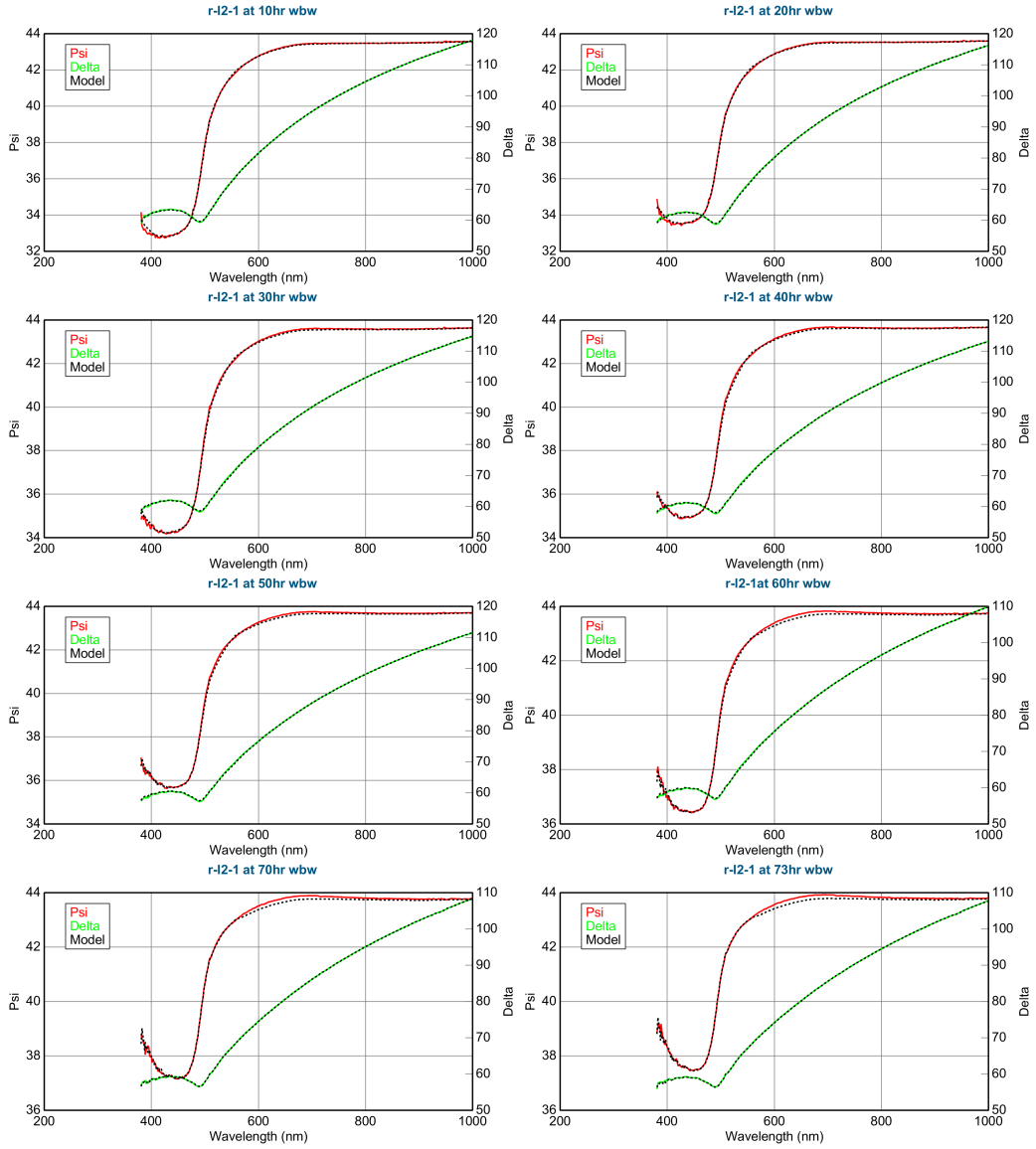

Figure 5.11: RTV566 VCM fitting results at 120K by 'WvlByWvl' derived optical constants at each time point

The fitted thickness versus time are compared to the QCM thickness in Fig. 5.12.

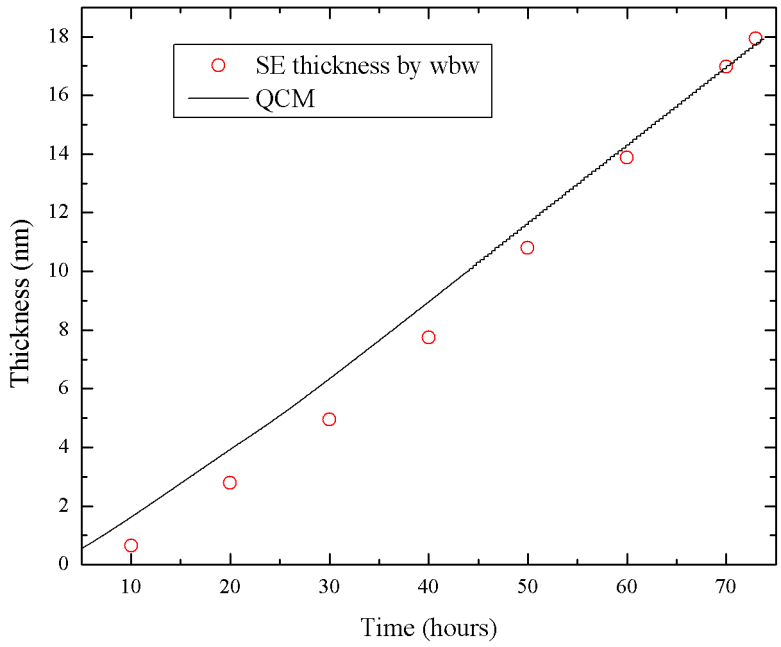

Figure 5.12: Thickness versus time fitted by end point optical constants comparing with QCM thickness (RTV566 VCM at 120K)

The deviation between the SE data and QCM thickness exists most apparently in the early stages of growth.

5.2.2 RTV566 150K VCM

The VCM film deposited at 150K will be analyzed in this section. Assuming the density of the film to be $1gm/cm^3$, the film deposited on the QCM substrate is approximately 11nm thick and accumulated over 75 hours. The QTGA data of the condensed films at three different temperatures implies that the condensed VCM at 120K contains water and possible material that evaporates just below 150K (see Fig.

5.1). In view of this, the optical constants at the end point of 120K VCM may be different from the optical constants at the end point of 150K and 180K.

The QCM thickness is plotted in Fig. 5.13.

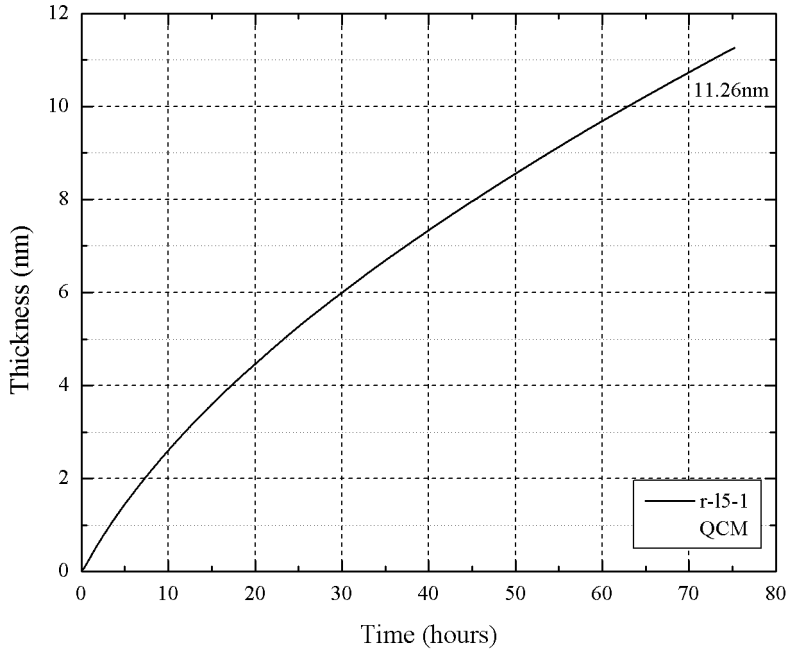

Figure 5.13: r-l5-1 QCM thickness versus time

From the figure, the thickness growth curve has higher growth rate at the early stage, then becomes linear with time.

5.2.2.1 RTV566 150K WvlByWvl model

As WvlByWvl model seems to be an effective model for the 120K VCM with a physical meaning and better MSE. The Cauchy modeling and Gen-Osc modeling are therefore not employed to analyze data at these higher condensation temperatures.

For the 150K VCM, it's been assumed from observation of the QTGA data that the 120K VCM differs from 150K VCM and 180K VCM by the unique temperature peak at the 275K evaporation point, and of course the absence of the peak at 140K. Therefore, the optical constants of 120K VCM may also be different from 150K VCM.

To test the validity of 120K VCM optical constants fit to the 150K VCM data, the optical constants from the 120K VCM are substituted into the end point SE data of the 150K VCM. The end point thickness is set at the QCM thickness. By generating the SE model data given the value of thickness and optical constants, the model generated and the raw SE data are shown in Fig. 5.14

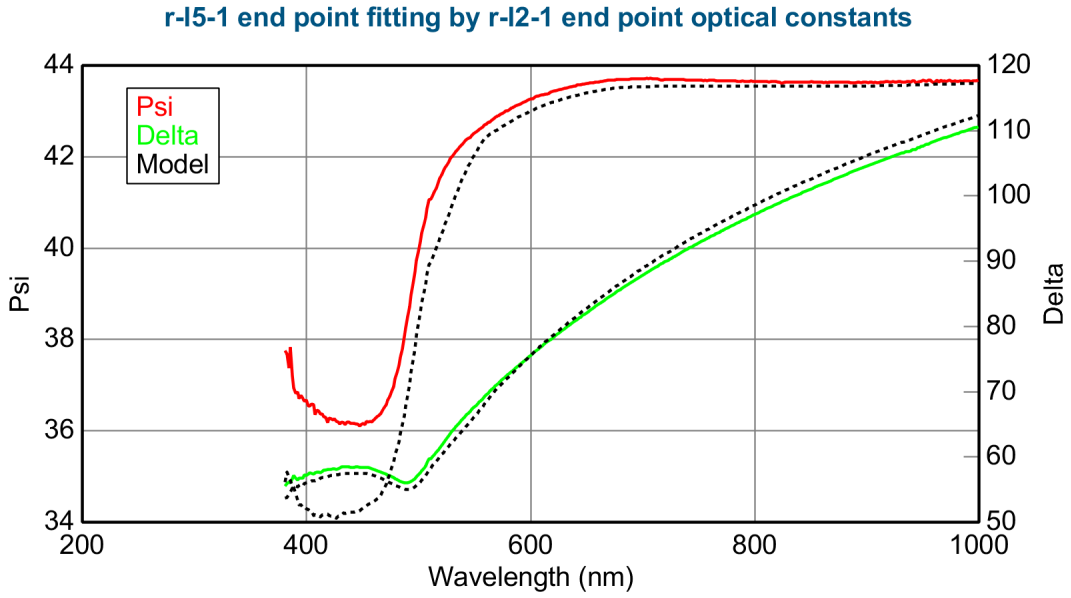

Figure 5.14: RTV566 150K end point fitting by 120K end point optical constants

The generated SE data from the QCM thickness and the optical constants of the 120K VCM while having the same general shape are different from the raw SE data with a large MSE of 28. The optical constants of 120K VCM cannot fit the 150K data effectively.

In view of this the 150K VCM end point SE data is independently fit employing the point by point approach. The fitting procedure for the 150K VCM is the same as that employed to fit the 120K VCM.

The end point optical constants of the 150K VCM are shown in Fig. 5.15. The MSE is 1.134.

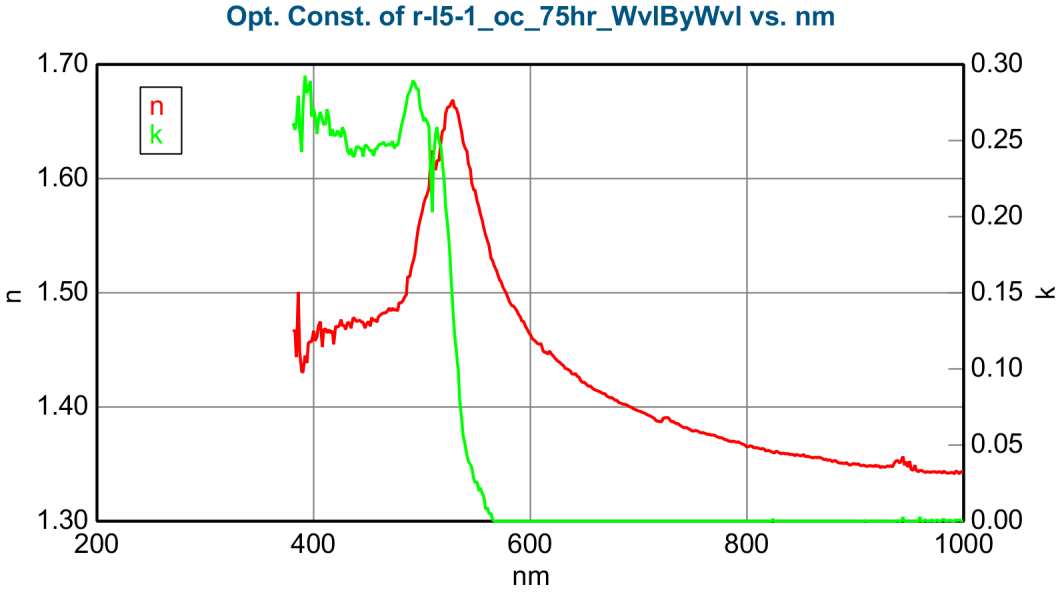

Figure 5.15: End point optical constants of RTV566 by 'WvlByWvl' at 150K deposition

The n and k of the 150K VCM are generally larger than the 120K VCM.

The thickness versus time for the 150K in-situ data are derived in the same manner as the 120K data. By substituting the end point optical constants of the 150K VCM at various times, the thickness can be obtained. The MSE and thickness for various times are shown in Table 5.4.

Table 5.4: RTV566 VCM film thickness at 150K fitted by end point optical constants at each time slice

Time Slice	Fitted Thickness (nm)	MSE
10	1.86	1.327
20	3.64	1.345
30	5.17	1.229
40	6.63	1.036
50	8.04	1.250
60	9.36	1.189
70	10.65	1.108

The SE data fitting results for each time slice is shown in 5.16.

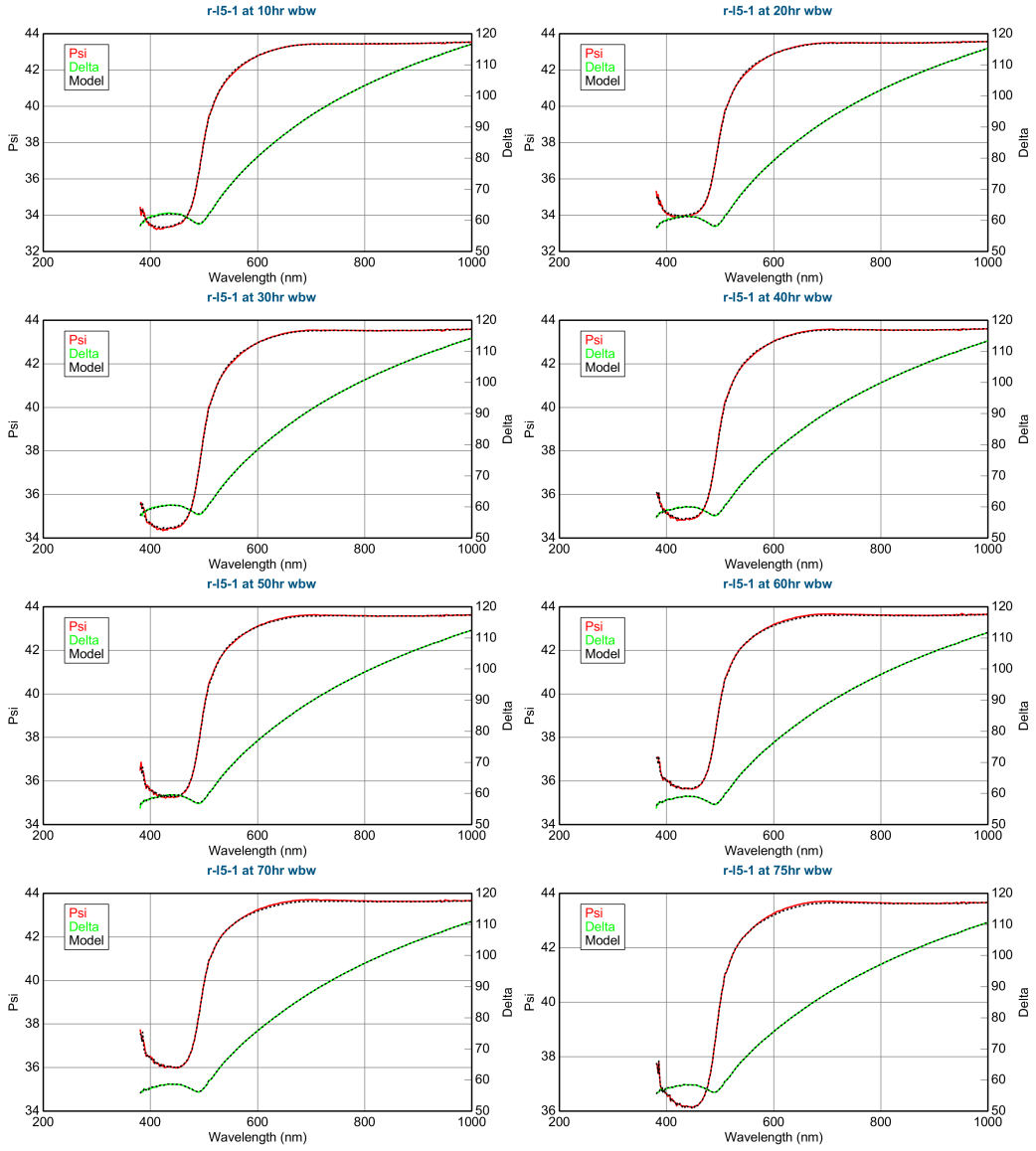

Figure 5.16: RTV566 VCM fitting results at 150K by 'WvlByWvl' derived optical constants at each time slice

The fitted thickness versus time for 150K VCM are compared to the QCM thickness in Fig. 5.17.

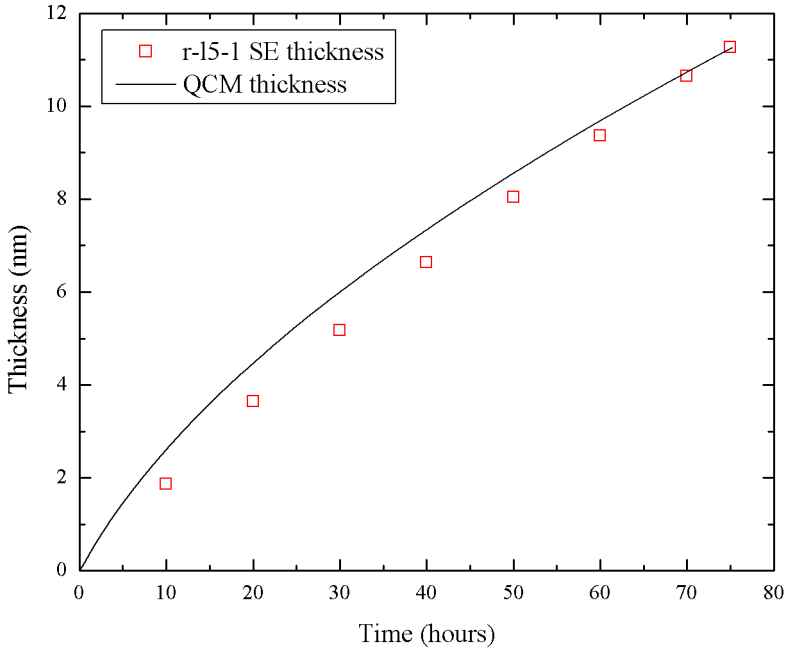

Figure 5.17: Thickness versus time fitted by end point optical constants comparing with QCM thickness (RTV566 VCM at 150K)

The SE fitted thickness is less than the QCM thickness during the initial stages of the deposition, a result identical to that observed for the 120K deposition.

5.2.3 RTV566 180K VCM

Assuming the density of the film to be $1gm/cm^3$, the film deposited on the QCM substrate is approximately 9nm thick and accumulated over 72 hours.

The QCM thickness is plotted in Fig. 5.18.

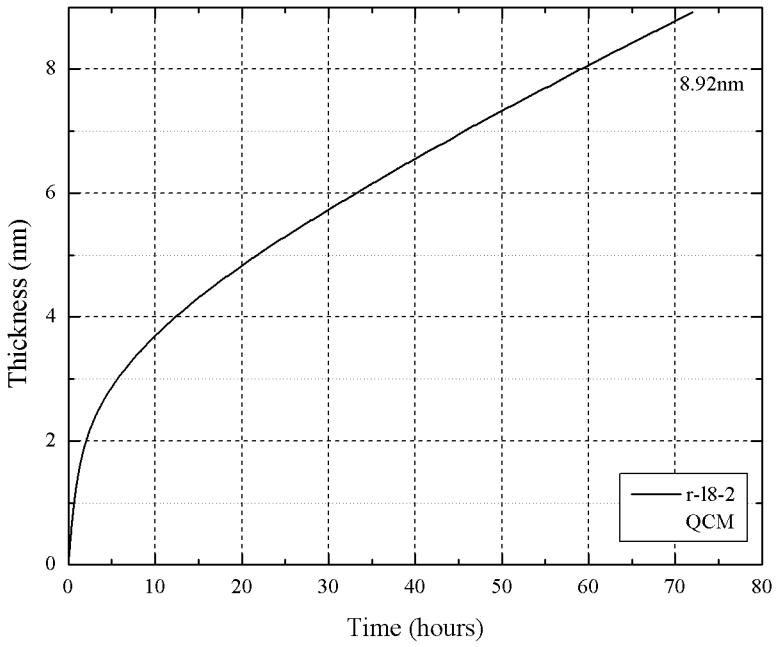

Figure 5.18: r-l8-2 QCM thickness versus time

5.2.3.1 RTV566 180K WvlByWvl model

The QTGA data (Fig. 5.1) clearly shows the films condensed at 150K and 180K have very similar if not identical composition. Therefore, the end point optical constants of the 150K VCM may provide a good fit to the 180K VCM.

By substituting the end point optical constants of the 150K VCM into the end point of the 180K VCM SE data, the fitted thickness is 8.75nm which is very close to the QCM thickness of 180K VCM - 8.92nm. The fit is shown in Fig. 5.19, where the MSE is 2.020.

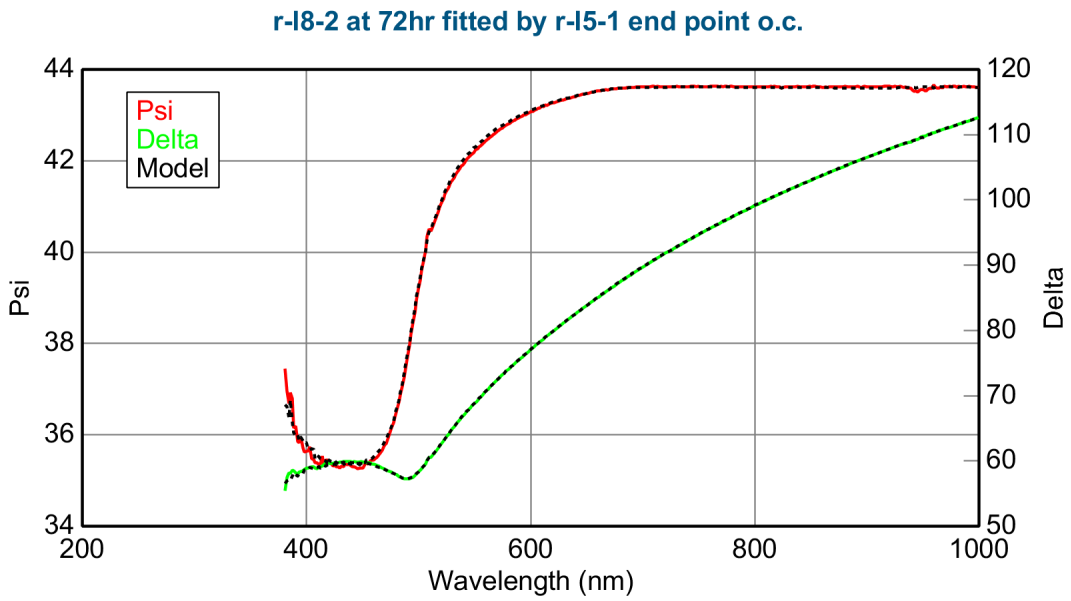

Figure 5.19: RTV566 180K end point fitting by 150K end point optical constants

Although the fit above is reasonable, the 'WvlByWvl.mat' model of the 180K VCM is generated in order to improve the MSE. This model yields an MSE of 0.547 at the 180K VCM end point when fixing the thickness to the QCM value of 8.92nm. The end point optical constants of the 180K VCM are compared to the end point optical constants of the 150K VCM in Fig. 5.20.

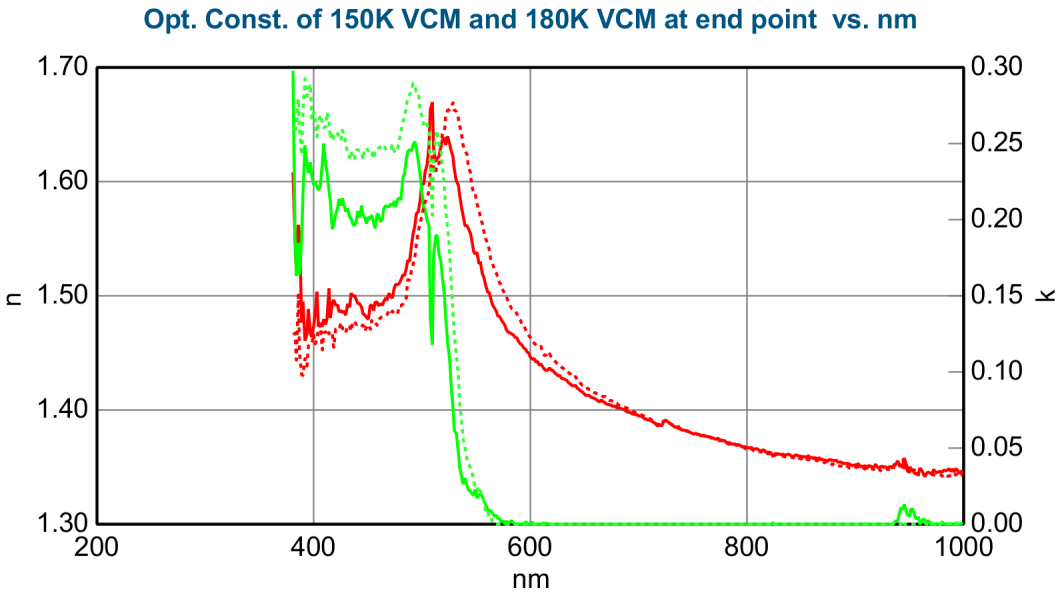

Figure 5.20: RTV566 180K end point optical constants comparing with 150K VCM end point optical constants (solid: 180K, dashed: 150K)

The optical constants of 180K VCM end point are very close the optical constants of 150K VCM end point. The 150K constants are slightly larger than the 180K constants, indicating that the film at 180K may not be as dense as the 150K film.

In order to provide the best fit, the thickness at each time slice are fitted by the 180K VCM end point optical constants. The fitting MSE and thickness are shown in Table. 5.5.

Table 5.5: RTV566 VCM film thickness at 180K fitted by end point optical constants at each time slice

Time Slice	Fitted Thickness (nm)	MSE
10	3.14	1.532
20	4.36	1.551
30	5.29	1.881
40	6.11	1.990
50	7.10	0.933
60	8.00	0.876
70	8.77	2.484
72(e.p.)	8.92	0.547

The SE data fitting results for each time slice is shown in 5.21.

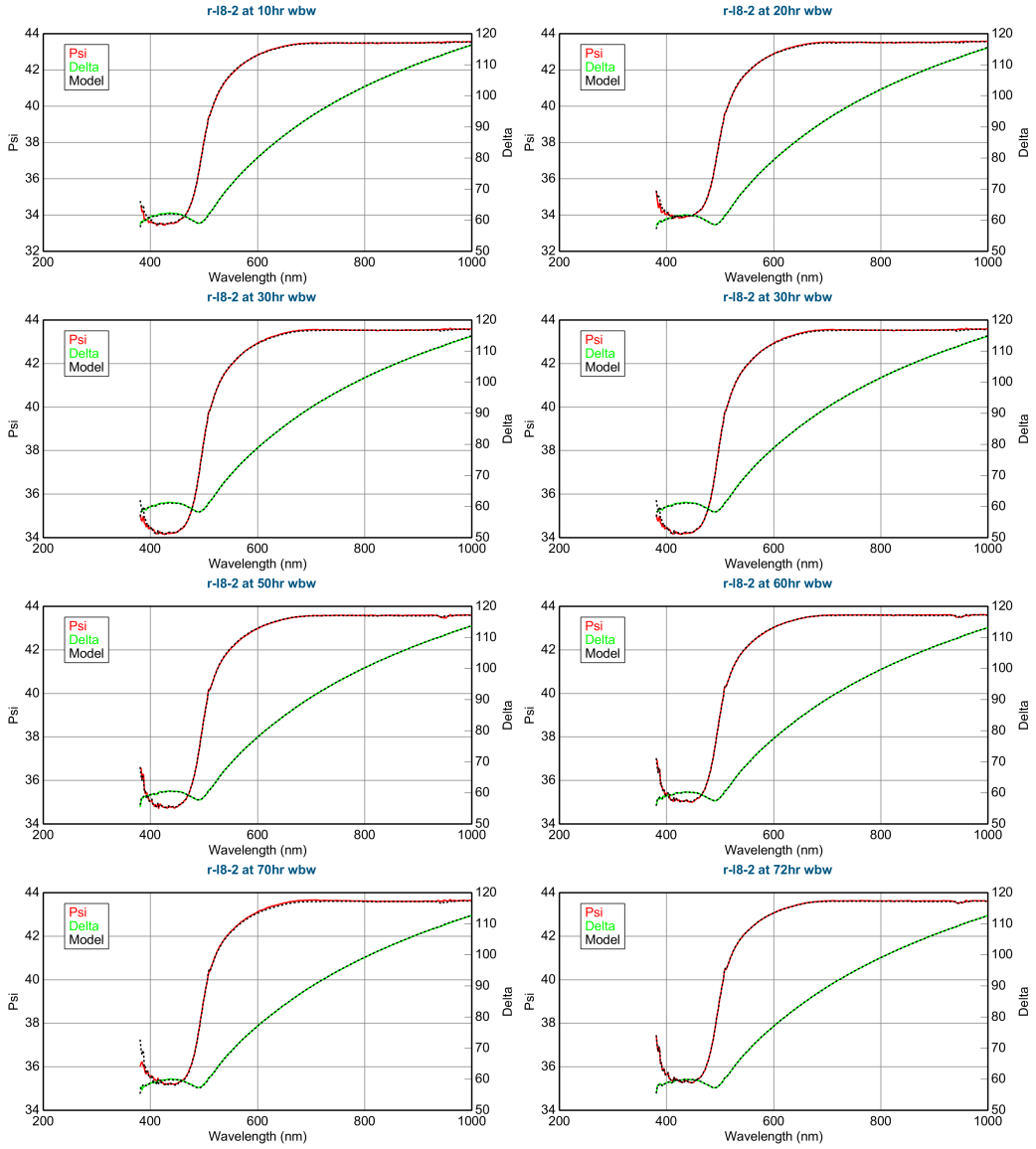

Figure 5.21: RTV566 VCM fitting results at 180K by 'WvlByWvl' derived optical constants at each time slice

The fitted thickness by the end point optical constants are compared to the QCM thickness in Fig. 5.22.

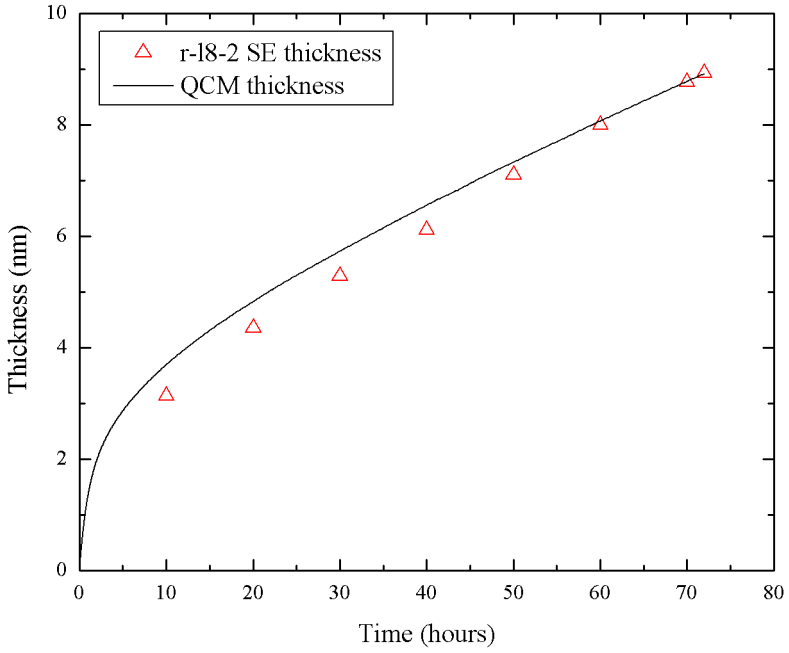

Figure 5.22: Thickness versus time fitted by end point optical constants comparing with QCM thickness (RTV566 VCM at 180K)

The SE fitted thickness is less than the QCM thickness during the initial stages of the deposition, a result identical to that observed for the 120K and 150K deposition.

5.2.4 Summary

The QTGA plot indicates that the major characteristic peak existing in the 120K VCM is around 273K which is more than likely water. The water peak along with another characteristic peak around 140K are not present in 150K VCM and 180K VCM. This difference more than likely contributes to the optical differences observed from the SE analysis.

The Cauchy model and Gen-Osc model provide a reasonably good fit to the data over the entire deposition. The WavelengthByWavelength model further improved the fitting results while still maintaining the K-K relationship. The assumption of film homogeneity in both density and optical properties is shown to be valid, at least to a first order, by the small absolute thickness differences between the calculated SE thickness, which is based on an optically homogeneous material, and the QCM thickness, which is based on a homogeneously dense material for all three temperatures.

The end point optical constants of the 120K VCM do not adequately fit the 150K VCM end point SE data. However, the end point optical constants of the 150K VCM can be fit to the 180K VCM with a reasonable MSE. The similarity for the 150K VCM and the 180K VCM exists in the QTGA data as well (Fig. 5.1), they share the same characteristic peaks.

All the fitted SE thicknesses deviate from the QCM thickness. Possible reasons for this include:

- The films are very thin, especially at the beginning 10 hr point, where the thickness of the deposited VCM is at most a few nanometers. The optical model may not be that accurate under these conditions.

- Ice contained in the 120K VCM. Based on the QTGA data, the 120K VCM does contain ice, which may result in an optically inhomogeneous film.

- The films may contain voids. During the initial stages of vapor deposition [45], polymer molecules tend to nucleate as islands, resulting in essentially porous films. The islands eventually coalesce and form a continuous films.

5.3 In-depth Analysis for RTV566 VCM

The previous section was a first order data analysis that indicated the homogeneous assumption was reasonable. However, the SE calculated thickness is always less than the QCM thickness, and this difference is most pronounced during the early stages of deposition in all three films.

In this section we will present an analysis based on inhomogeneous films in order to improve the data fits and provide physical insight into the time evolution of the depositing film

5.3.1 RTV566 120K VCM

There are several possible explanations for the deviation of the SE data from the QCM data during the initial stages of deposition. The films are extremely thin so the SE signals are small resulting in errors in the SE calculation.

The VCM film could be inhomogeneous during the early stages of deposition. Early stages of film growth are often characterized by nucleation / island formation resulting in porous films. If this is the case the density variation with film thickness (deposition time) would have to be taken into account when calculating thickness from the QCM frequency change. Qualitatively a less dense film would result in a larger thickness for a given frequency change, which would push the QCM thickness further away from the SE values. However, the SE data would have to be modeled using a graded EMA layer consisting of a set of material constants mixed with a void fraction, where the void fraction would be allowed to vary with film thickness. The problem here is that the film density and thickness are directly correlated in the QCM data and there is no physical model that allows prediction of the density versus thickness. Therefore it is possible to fit the QCM frequency data and SE data to

virtually any $\rho(x)$ function that is chosen.

That being said the thickness from the QCM data when assuming a fixed density is reasonably linear. Significant changes in density during deposition would result in a non-linear thickness curve if the density is assumed constant, which is not the case here. If the density variation is small, say on the order of 10% the QCM thickness would be minimally altered, while a graded EMA layer as discussed above may provide a better fit to the data.

5.3.1.1 Void Approach for 120K VCM

The end point optical constants from the SE data were generated by assuming the density of VCM film to be $1 gm/cm^3$ which is shown in Fig. 5.10. By substituting the end point optical constants into other time point while assuming the thickness to be identical to the QCM thickness, the fitting MSE can be evaluated.

The table below shows the fitting MSE when substituting the end point optical constants into the SE data at various time points, where the thickness in the SE model is fixed at the QCM thickness.

Table 5.6: RTV566 120K SE data fitting MSE using end point optical constants and QCM thickness

Time (hours)	QCM thickness (nm)	SE thickness (nm)	MSE
10	1.62	1.62	4.377
20	3.93	3.93	6.550
30	6.34	6.34	7.638
40	8.96	8.96	6.446
50	11.6	11.6	4.382
60	14.3	14.3	2.709

As can be seen from Table 5.6, the MSE is fairly large.

Using the graded layer model with void fraction while still fixing the thickness to be the QCM thickness, the void fraction and MSE are derived in Table 5.7 for each time point respectively.

Table 5.7: RTV566 120K SE data fitting MSE and void fraction by graded model using end point optical constants and QCM thickness

Time (hours)	QCM thickness (nm)	SE thickness (nm)	MSE	Void (%)
10	1.62	1.62	1.554	45.9
20	3.93	3.93	1.514	27.9
30	6.34	6.34	1.851	22.7
40	8.96	8.96	1.999	15.7
50	11.6	11.6	2.149	8.7
60	14.3	14.3	1.957	7.8

Comparing to Table 5.6, the MSE is reduced by introducing a void fraction. However, the void fraction is large at the early stages of deposition.

When the 'void' fraction is introduced to the optical model of film, the density of $1g/cm^3$ needs to be changed because the VCM film is modeled as a porous one. For example, at the 10 hour time point, the density of the film is changed to $0.459g/cm^3$ based on the void fraction (density of $0g/cm^3$). The QCM thickness needs to be altered to $1.62nm/(1-0.459) = 2.99nm$, once again, when substituting this thickness ($2.99nm$) into the EMA model, the void fraction will be fitted again, in this situation, the void fraction is modeled to be 61.6%. By doing this iteration again and again, the void fraction will converge to a single value, however, for the 120K VCM, the void fraction after several iterations is over 89%. This converged void fraction value is an unreasonable result. This self-consistent approach for this VCM film is not valid.

5.3.1.2 Ice Approach for the 120K VCM

From the QTGA data (Fig. 5.1), the VCM film at 120K has a water peak. Instead of putting 'void' into the EMA model as a second material, the optical constants of ice and the end point optical constants of the 150K VCM film are mixed together to model the VCM film at 120K. The 150K VCM film material is used since it does not have ice in it. The optical constants of ice are derived by Warren [46]. As the density of ice is very close to $1 g/cm^3$ at low temperature, the thickness converted from the QCM frequency change in Fig. 5.2 is still valid for the SE analysis.

The EMA model mixed with 150K VCM end point optical constants and ice is shown in Fig. 5.23

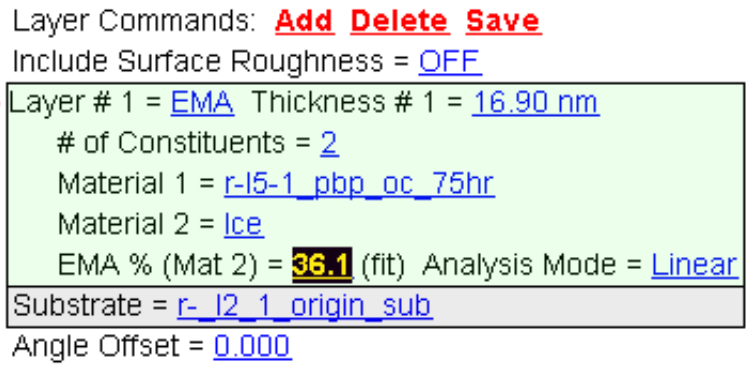

Figure 5.23: RTV566 VCM EMA Ice model at 70 hr

The fitting results for RTV566 120K VCM with 150K end point optical constants and ice are shown in Table 5.8

Table 5.8: RTV566 120K VCM modeled by EMA model with ice at various time points

Time (hours)	QCM thickness (nm)	SE thickness (nm)	MSE	Ice(%)
10	1.62	1.62	2.182	99.1
20	3.93	3.93	2.660	88.9
30	6.34	6.34	4.079	79.4
40	8.96	8.96	4.279	60.8
50	11.6	11.6	3.536	47.5
60	14.3	14.3	2.787	40.3
70	16.9	16.9	2.333	36.1

The equivalent (not physical or realistic) thickness for ice calculated from the material percentage in the EMA model is plotted in Fig. 5.24.

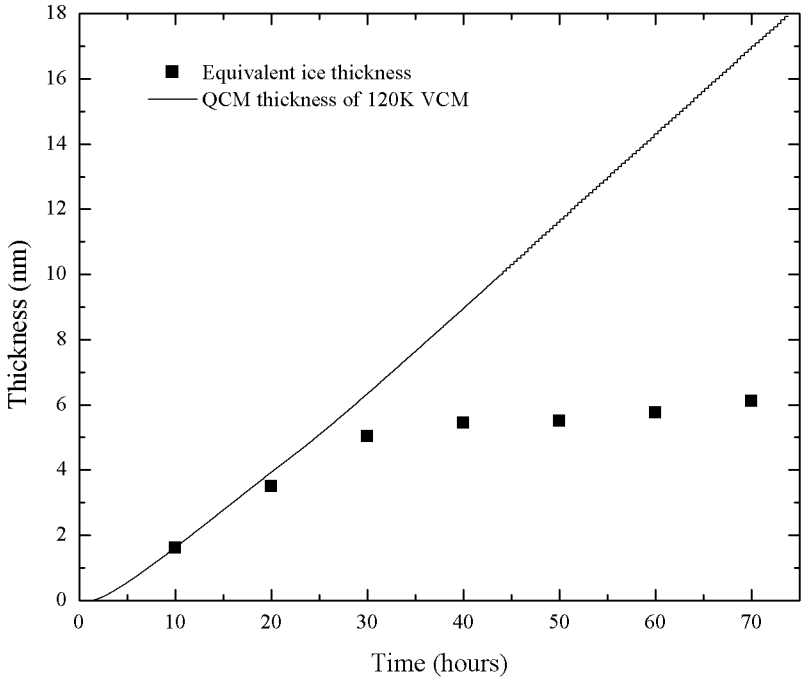

Figure 5.24: Calculated Ice equivalent thickness versus time for RTV566 120K VCM as compared with QCM thickness

This result indicates that ice dominated the deposition process in the early stages, where the ice/VCM ratio stabilizes at the later stages.

By modeling 120K VCM SE data with ice and pure material (150K VCM optical constants) in an EMA model, the modeled SE thickness and QCM thickness by unity density are overlapping, as calculated by assuming a density of $1 g/cm^3$, can be set equal and still result in a low MSE.

To improve the MSE, 150K VCM optical constants are put into the B-Spline model as a starting material, the thickness is fixed to the QCM thickness, and the percentage of ice is fixed as well.

The model is shown in Fig. 5.25

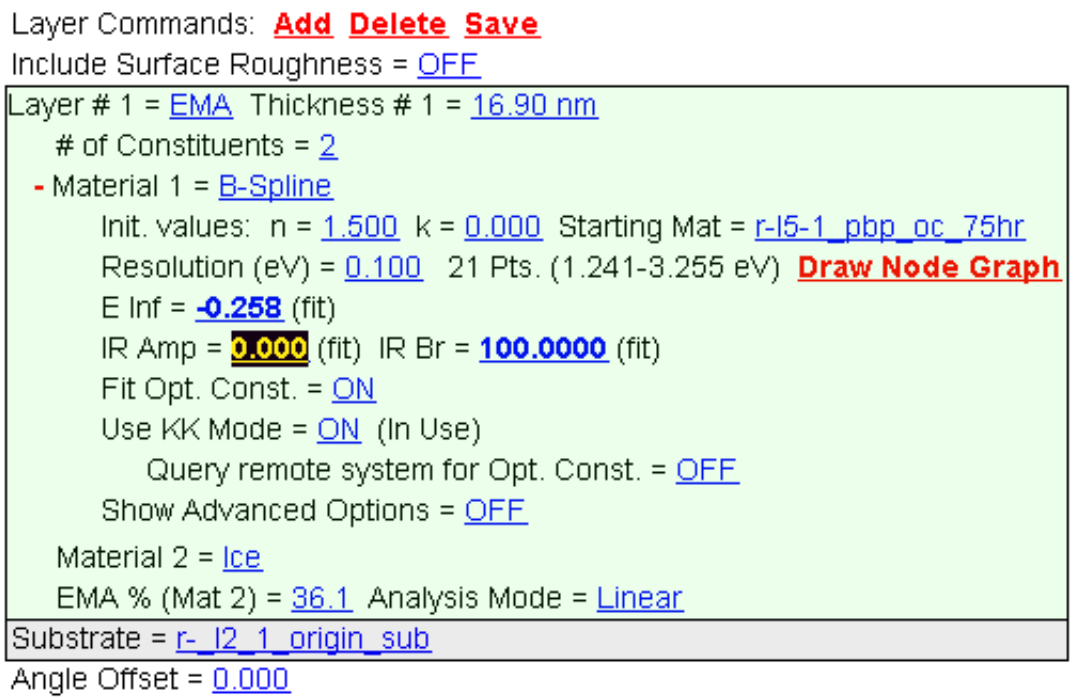

Figure 5.25: RTV566 VCM EMA Ice model at 70 hr revised by B-Spline model with starting material of 150K VCM end point optical constants

The EMA model is saved as tabulated optical constants are used to fit the SE data at other time points. The new model with revised optical constants provides a lower fitting MSE as shown in Table 5.9.

Table 5.9: RTV566 120K VCM modeled by EMA model consists of ice and B-Spline at various time points

Time (hours)	QCM thickness (nm)	SE thickness (nm)	MSE	Ice(%)
10	1.62	1.62	1.973	99.1
20	3.93	3.93	1.612	88.9
30	6.34	6.34	1.823	79.4
40	8.96	8.96	1.760	60.8
50	11.6	11.6	1.953	47.5
60	14.3	14.3	1.641	40.3
70	16.9	16.9	1.80	36.1

The EMA model with VCM and ice provides a close fit to the QCM thickness, while maintaining a connection to the physical data supplied by the QTGA analysis.

The optical constants of the EMA model with ice and optical constants of 'WvlByWvl.mat' are shown in Fig. 5.26.

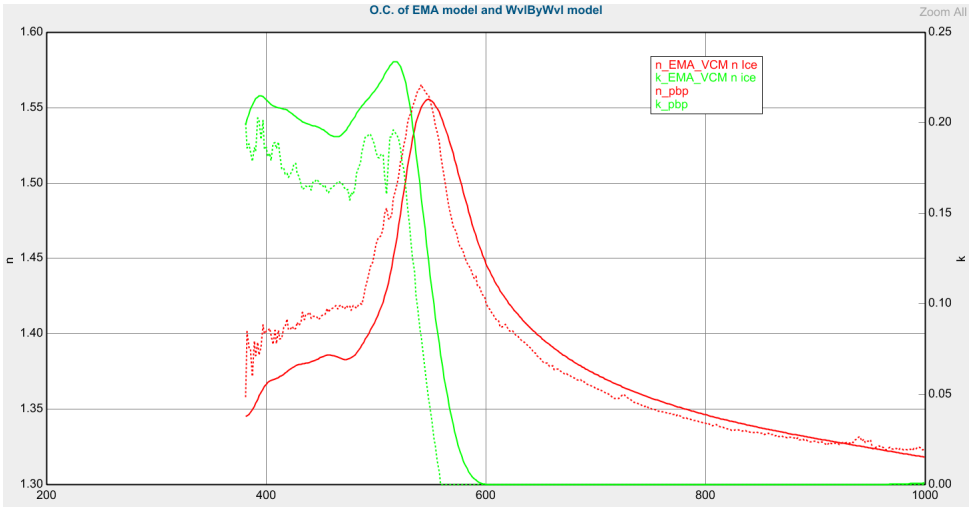

Figure 5.26: RTV566 120K VCM optical constants of EMA model and WvlByWvl model at the end point

The dashed lines represent the optical constants of the 'WvlByWvl' model at the end point, while the solid lines represent the optical constants of the EMA model with ice at the end point. These two models yield optical constants that have a similar shape and amplitude, where both can provide low MSEs, however, the ice composition model directly relates to the QTGA data.

5.3.2 RTV566 150K VCM

The 120K VCM can be fitted by 150K VCM optical constants with ice in EMA model since 120K VCM consists of RTV566 VCM and ice. Since the QTGA data does not indicate ice is present in the 150K VCM, it is assumed to be a pure material. However, the film may contain some void fraction, especially at the early stages of deposition, [45] [47] [48] which could result in the difference between the SE and QCM film thicknesses.

5.3.2.1 Void Approach for 150K VCM

In order to model the 150K VCM film using an EMA mixture with void, the end point film is modeled as a single homogeneous material. The EMA material then consists of end point 150K VCM material mixed with void fraction. This material is used to model the SE data at various time points where the thickness at the given time is set equal to the QCM thickness and the void fraction is allowed to vary. The void fraction and fitting MSE is shown in Table 5.10.

Table 5.10: RTV566 150K SE data fitting MSE and void fraction by EMA model using end point optical constants and QCM thickness

Time (hours)	QCM thickness (nm)	SE thickness (nm)	MSE	Void(%)
10	2.607	2.607	1.210	22.8
20	4.462	4.462	1.275	14.6
30	5.996	5.996	1.181	11.1
40	7.339	7.339	1.004	7.9
50	8.557	8.557	1.264	5
60	9.687	9.687	1.206	2.8
70	10.738	10.738	1.113	0.7

The biggest void fraction is at the initial time point at 10hr. The percentage is much less than obtained when this approach was applied to the 120K VCM. As discussed previously, the void fraction, film density and QCM thickness can be iterated until a self-consistent result between the QCM thickness and SE data is obtained. For example, at the 10 hr time point, the void percentage is 22.8, the thickness is $2.607nm$, the QCM thickness should be revised to $2.607/(1-0.228) = 3.377nm$, then set thickness to $3.377nm$ in the SE model, the void fraction and will be fitted again with this new thickness, and so on, until the QCM and thickness match.

The final thickness and void fraction at various time points is shown in Table 5.11

Table 5.11: RTV566 150K self-consistent void fraction and thickness with iteration

	QCM final (nm)	MSE	void final (%)
10hr	7.448	1.31	65
20hr	9.069	1.631	50.8
30hr	10.631	1.687	43.6
40hr	11.019	1.495	33.4
50hr	10.998	1.557	21.2
60hr	10.884	1.336	11
70hr	10.923	1.122	1.7

The self-consistent thickness is compared with the original QCM thickness when assuming the density of film is $1 gm/cm^3$ in Figure 5.27

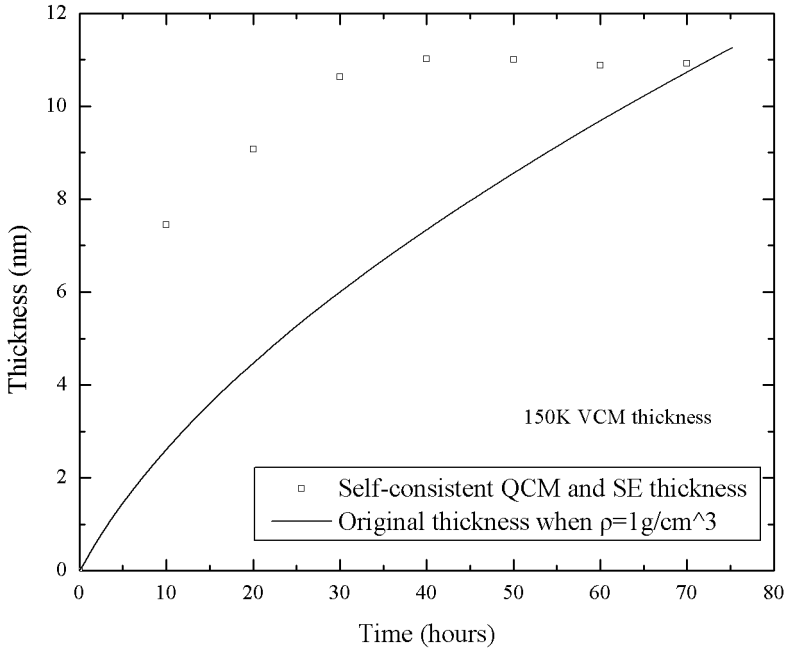

Figure 5.27: Self-consistent thickness for 150K VCM

The fitted SE thickness and QCM thickness correspond to the hollow square points while the solid line represent the QCM thickness when assuming the density of film is $1gm/cm^3$. The thickness based on the self-consistent approach is initially large because the void fraction is quite large (65%). However, based on this approach the growth slows and eventually appears to saturate around 40 hours. However, based on the self-consistent approach the films density increases even though the thickness remains constant.

The self-consistent optical constants are shown in Fig. 5.28 at wavelength of $582nm$ for various time points.

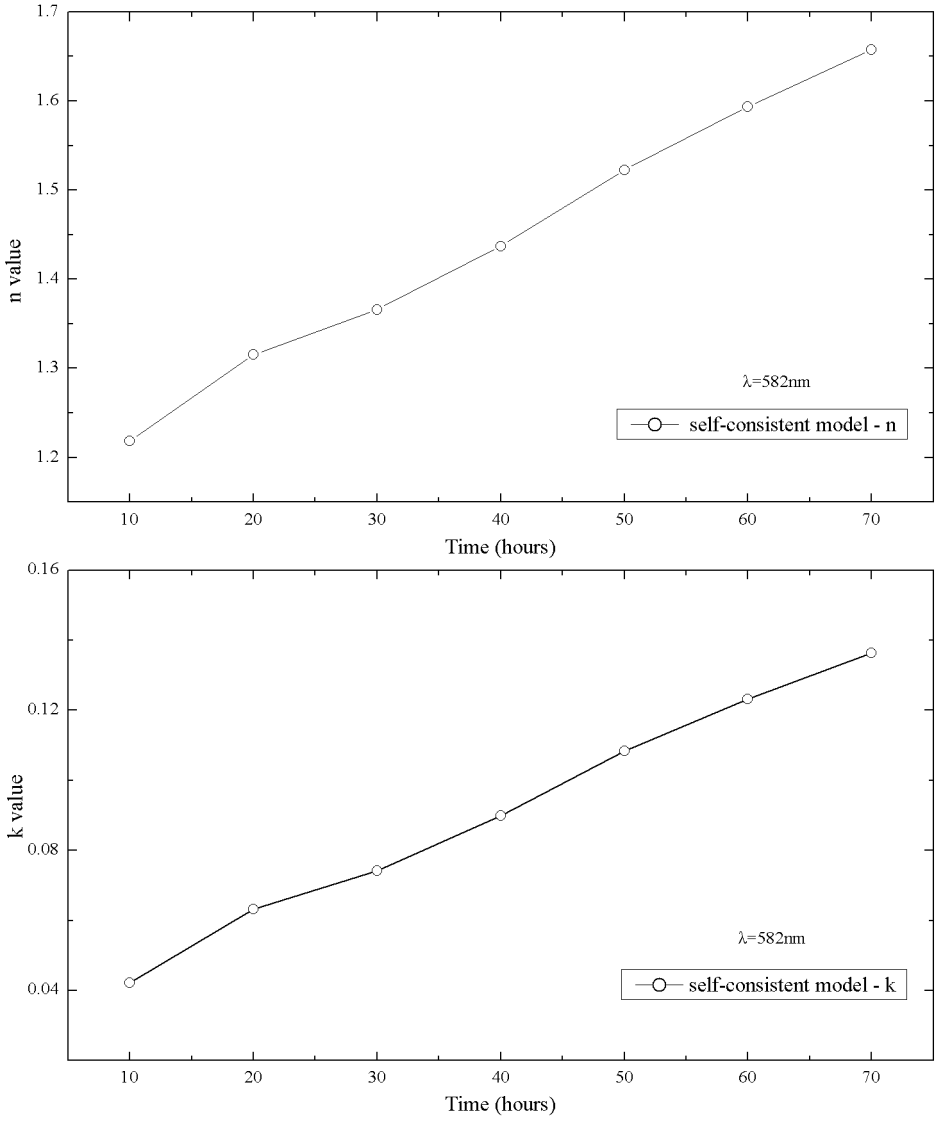

Figure 5.28: EMA model and self-consistent optical constants for 150K VCM

From Fig. 5.28, as the density increases from the beginning to the end point of deposition, the values of n and k increase as well.

As seen from Fig. 5.27, the thickness saturates at the later stage of VCM growth and the film densified which is consistent with results discussed in references [45] [47]

[48] in that polymer molecules tend to form isolated islands during the initial stages of growth, yielding porous films and the thickness growth rate slows down and stabilizes during the later stage of growth, yielding denser films and constant film thickness.

The EMA model consisting of void fraction and end point optical constants simulated the porosity change and optical constants change throughout the growth of the VCM film. The modeled thickness and porosity coincide with the explanations discussed in the references.

5.3.3 RTV566 180K VCM

The same approach used to analyze the 150K VCM is employed to analyze the 180K VCM.

5.3.3.1 Void Approach for 180K VCM

The offset between the QCM thickness and SE fitted thickness exists during the early stages of deposition for the 180K VCM. The same EMA approach employed to fit the 150K VCM will be used here to fit the 180K VCM. The EMA material will consist of the end point material, assuming it is a homogeneous material, mixed with void.

The fitted void fraction and MSE are shown in Table 5.12 with the QCM thickness at multiple time points.

Table 5.12: RTV566 VCM film thickness at 180K fitted by end point optical constants and EMA model at each time point

Time Point (hour)	QCM thickness (nm)	MSE	void %
10	3.695	1.445	12.8
20	4.83	1.481	8.3
30	5.73	1.828	6.6
40	6.56	1.938	5.9
50	7.33	0.945	2.7
60	8.07	0.877	0.7
70	8.78	0.912	0.2

The biggest void fraction is at time point 10hr with small MSE. The percentage is 12.9%.

Using the iteration procedure for thickness and void fraction for 180K VCM, the final thickness and void fraction at various time points is shown in Table 5.13

Table 5.13: RTV566 180K self-consistent void fraction and thickness with iteration

	QCM final (nm)	MSE	void final (%)
10hr	7.02	1.210	47.3
20hr	7.362	1.302	34.4
30hr	8.104	1.672	29.3
40hr	8.19	1.818	22.0
50hr	8.18	1.023	10.2
60hr	8.319	0.887	3
70hr	8.806	0.912	0.3

The self-consistent thickness is compared with original QCM thickness when as-

suming the density of film is $1gm/cm^3$ in Figure 5.29

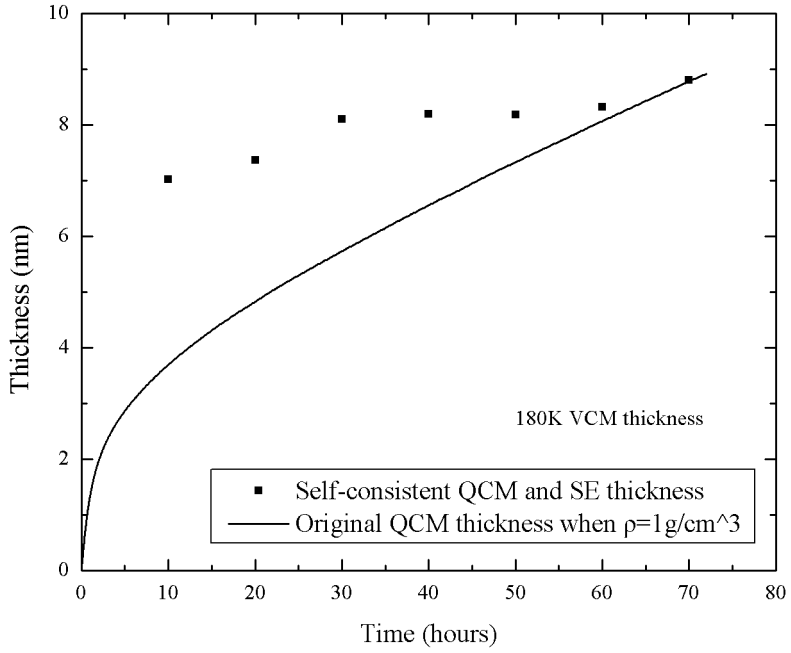

Figure 5.29: Self-consistent thickness for 180K VCM

The self-consistent thickness starts with a large value, then increased to a steady thickness value, meanwhile the void fraction decreased to almost zero at the end point.

The optical constants of self-consistent approach are plotted in Fig. 5.30

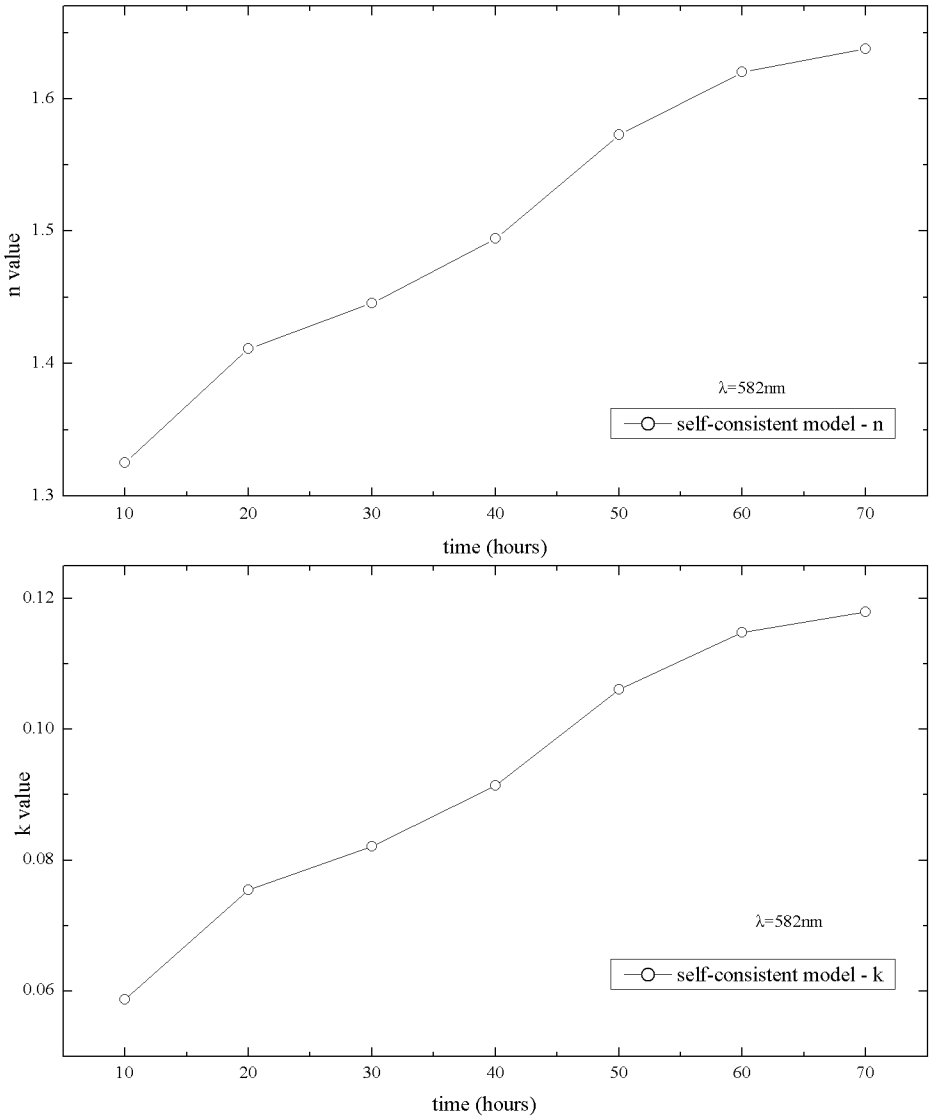

Figure 5.30: EMA model and self-consistent optical constants for 180K VCM

From Fig. 5.29 and Fig. 5.30, it also can be seen that the thickness saturates and film densified at later stage of growth. This can be explained in the same manner by the 150K VCM void approach in previous section.

5.3.4 Summary

In this chapter, two different approaches have been applied to analyze the data.

Assuming a homogeneous VCM film with a density of $1g/cm^3$, reasonable results are obtained by the basic Cauchy and Gen-Osc optical models. However, the deviation between the QCM thickness and the derived SE thickness exists in the early stage of deposition.

The consistent deviation between the QCM and SE thickness in the initial stages of growth for all three condensation temperatures may indicate that either the model needs to be revised or the assumption of film density needs to be altered. The film condensed at 120K clearly contains ice, and as seen from Chapter 4, ice condenses uniformly and homogeneously at 120K. Without forfeiting the assumption of $1g/cm^3$ density, an EMA model combining ice along with VCM optical constants of the 150K VCM provide an excellent fit to the data. For 150K VCM and 180K VCM, there is no ice observed in the QTGA data. However it is known that [45] [47] [48], polymer molecules tend to form islands during the initial stages of growth, yielding porous films. As the growth process continues the islands coalesce into a continuous film while the thickness remains roughly constant. In view of this, and EMA layer consisting of void fraction and end point optical constants was applied to the 150K and 180K films. A self-consistent approach based on iterating the QCM thickness and void fraction yields an excellent fit to the data.

Chapter 6

Atomic Oxygen Influence on VCM deposition

Atomic oxygen (AO) is produced by photo-dissociation of diatomic oxygen molecules by solar ultra violet radiation. The AO bombardment of spacecraft surfaces by AO may drive physical and chemical reactions on the surfaces [6]. Reactions of AO with different polymeric materials has been shown to occur by various mechanisms[49] including abstraction, addition, elimination, insertion and replacement. It is likely that simultaneous AO exposure and CVCM deposition occurs in LEO. The first report of simultaneous CVCM deposition during AO exposure is discussed in this chapter.

The experiments can be divided into two parts.

- The effect of AO on existing VCM films.
- VCM film deposition in the presence of AO.

6.1 The effect of AO on photo-fixed RTV566 VCM films

In this section, the photofixed VCM films are obtained on one side of a silicon wafer in a cyro-pumped small volume chamber via the simultaneous exposure of the room temperature substrate to a UV source and the outgassing particle flux impingement of RTV566 held at 100 °C [43]. Then this photofixed VCM film is transferred into

AO chamber. The optical constants of the film are measured before and after AO exposure.

6.1.1 Experimental Apparatus

The deposition chamber setup shown in Fig. 6.1, consists of a small volume stainless chamber pumped by a cryo-pump to minimize the water vapor background. The UV light spectrum in the 150-190 nm range was produced by microwave excitation of a high pressure Xe filled UV lamp with a MgF_2 window. A MgF_2 window is placed on top of the UV lamp output window to prevent contamination of the lamp window, the window needs to be cleaned after each deposition. The cured, cubic pieces of RTV566 were placed in the effusion cell. The effusion cell was controlled to a fixed temperature of 100 °C.

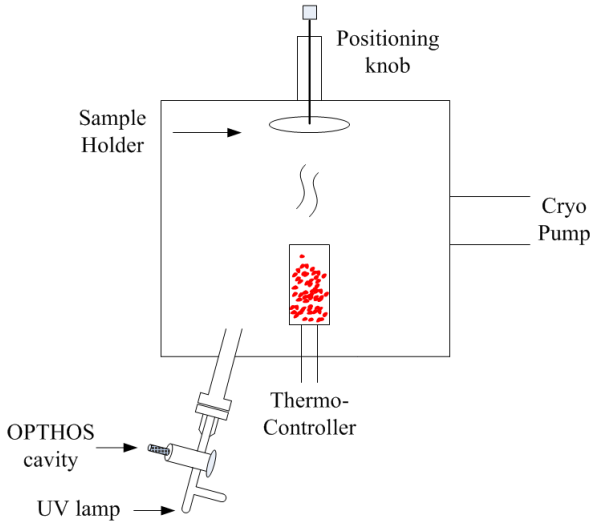

Figure 6.1: Photo-fixing chamber setup

The Xe-filled UV lamp provides the illumination to photofix the depositing VCM.

The AO setup, as seen in Fig. 6.2, consists of a stainless steel chamber pumped by a turbo pump (TURBOVAC 600C) down to a base pressure of of $1 \times 10^{-6} Torr$, the turbo pump is backed by a Fomblin oil filled mechanical pump.

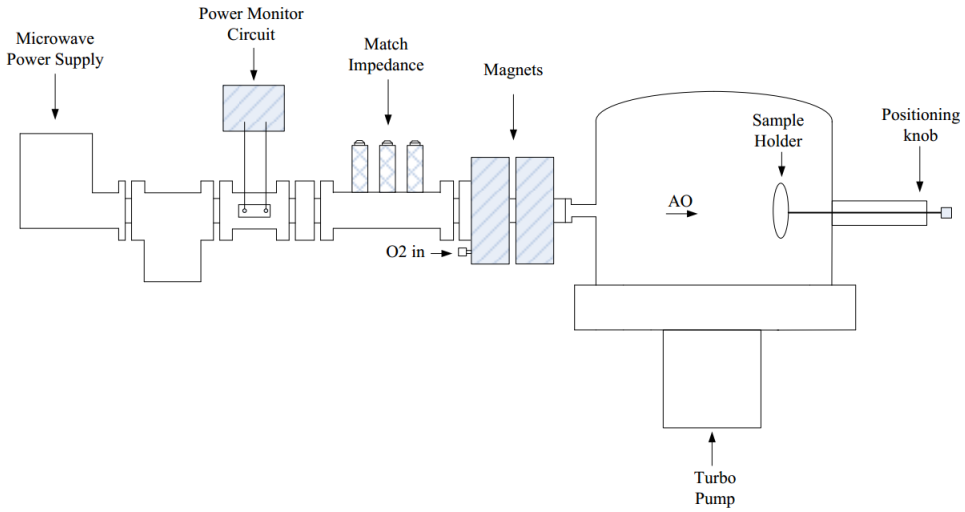

Figure 6.2: ECR setup for chamber

The typical operating condition for the chamber are 400W input power, gas flow $10 sccm O_2$, and pressure $9 \times 10^{-4} Torr$. An electron cyclotron resonance source (ECR) was used to simulate the LEO environment.

6.1.2 Sample preparation

Step 1.

A virgin silicon wafer was cleaned by the procedure discussed in [43]. Then it is put into the chamber (Fig. 6.1), where it is held by a sample holder located on the top inside of the chamber, and the height of the sample holder was adjusted to align the sample to be illuminated by the UV lamp. This step is essential. If the light beam cannot reach the surface of the silicon wafer, there will be no photo-fixed VCM

films made. The photofixed VCM film can be taken out of the deposition chamber for characterization by an ex-situ ellipsometer. The thin film is smooth, and uniform.

Step 2.

The photo-fixed RTV566 VCM film is transported into the AO simulation chamber (Fig. 6.2). The ECR oxygen plasma is initiated and the film is exposed for a preset time. It should be pointed out that the oxygen plasma produces 135nm radiation which also illuminated the film along with the AO. The exposed film is characterized by *ex-situ* ellipsometry.

6.1.3 Fitting procedure for photofixed VCM films

Two sample VCM films of RTV566 material were made. Before each deposition, the native oxide thickness was determined by *ex-situ* ellipsometry. After completion of the deposition, three points on the sample were ellipsometrically measured by employing the focusing probe at multiple angles. The overall optical model for the VCM film on the substrate is a Cauchy layer on native oxide on silicon wafer. After the exposure of AO, the samples were measured again at three different points by using the focusing probe.

Multi-sample analysis (MSA) is used to determine the overall optical constants of three spots on the same sample with only one variable - the thickness at each of the spots.

The fitting procedure for VCM films before and after AO is illustrated in Fig. 6.3.

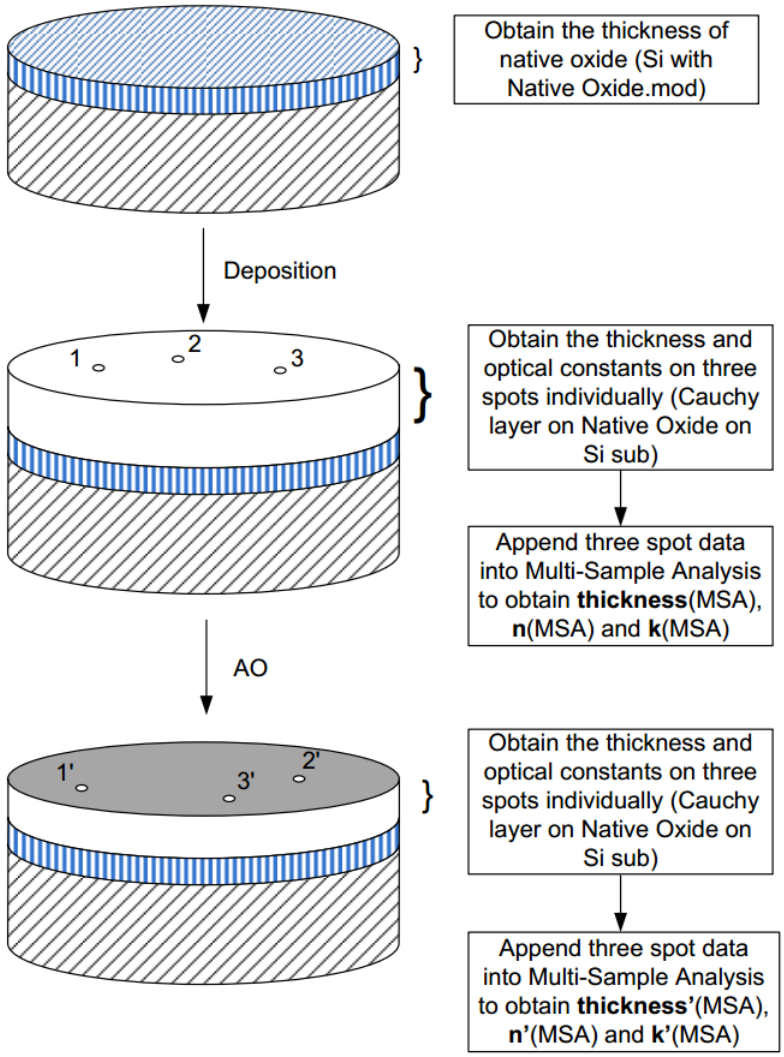

Figure 6.3: Fitting procedure for VCM films before and after AO

6.1.4 AO exposure of photofixed RTV566 VCM films

The ellipsometric data were obtained after film deposition process and also after the AO exposure.

Two separate bulk RTV566 samples were used to form VCM films on two different silicon wafers. The details of the deposition and exposure process are shown in Table

6.1. The ellipsometric results for each individual spot from the two samples of RTV566 ($Si03$ and $Si04$) are also shown in Table 6.1, where the film thickness is derived from the ellipsometric data fit using the Cauchy model.

Table 6.1: RTV566 Tests Results List - AO Part1

Label	Spot	Nat. Oxide	Dep. Time	AO Time	MSE	Film (nm)
Si03	1	2.03nm	24 hours		6.144	283.01
	2				8.546	269.03
	3				7.656	282.26
Si03_AO	1			12 hours	8.97	242.09
	2				6.774	246.07
	3				7.009	237.35
Si04	1	1.90nm	6 hours		1.247	55.53
	2				1.086	53.73
	3				1.288	52.15
Si04_AO	1			6 hours	1.088	38.35
	2				0.951	38.75
	3				0.928	36.24

The VASE data fitting result for RTV566 Si03 and Si04 are shown in Fig. G.1, Fig. G.2, Fig. G.3 and Fig. G.4.

The optical constants of each spot on RTV566 VCM sample before AO and after AO for Si03 and Si04 are shown in Fig. E.1, Fig. E.2, Fig. E.3 and Fig. E.4.

The thickness was reduced by the AO exposure for both of samples. The similar thicknesses at three different spots of the sample before AO exposure indicates the deposited VCM film is reasonably uniform. After several hours of AO exposure, the film maintains its uniformity, indicating the AO exposure is also uniform. The

etch rate for Si03 is approximately $(278.1 - 241.83)nm/12hours \approx 3nm/hour$. The etch rate for Si04 is approximately $(53.8nm - 37.78nm)/12hours \approx 2.67nm/hour$. Therefore, the etch rate for each sample is almost identical regardless of how thick the initial film is. This indicates the consistency of the films and the AO process. In addition, this implies the film can be completely etched off if the AO exposure duration is long enough.

The derivation of the thickness and optical constants of the films is based on employing the MSA approach while using a Cauchy model for the material.

Multi-sample analysis can be used to quantify films with different thicknesses. MSA can work on the same sample at different locations, or it can be applied to different samples of the same material [50].

For example, for sample Si03, the optical constants can be derived from the ellipsometric data taken at three different spots because the optical constants are the same everywhere on the sample since it is an optically uniform film, however there does exist a small variation in thickness at different spots.

The optical constants based on multi-sample analysis (n_{MSA}, k_{MSA}) for these three spots on samples Si03 and Si04 are shown in Fig. 6.4.

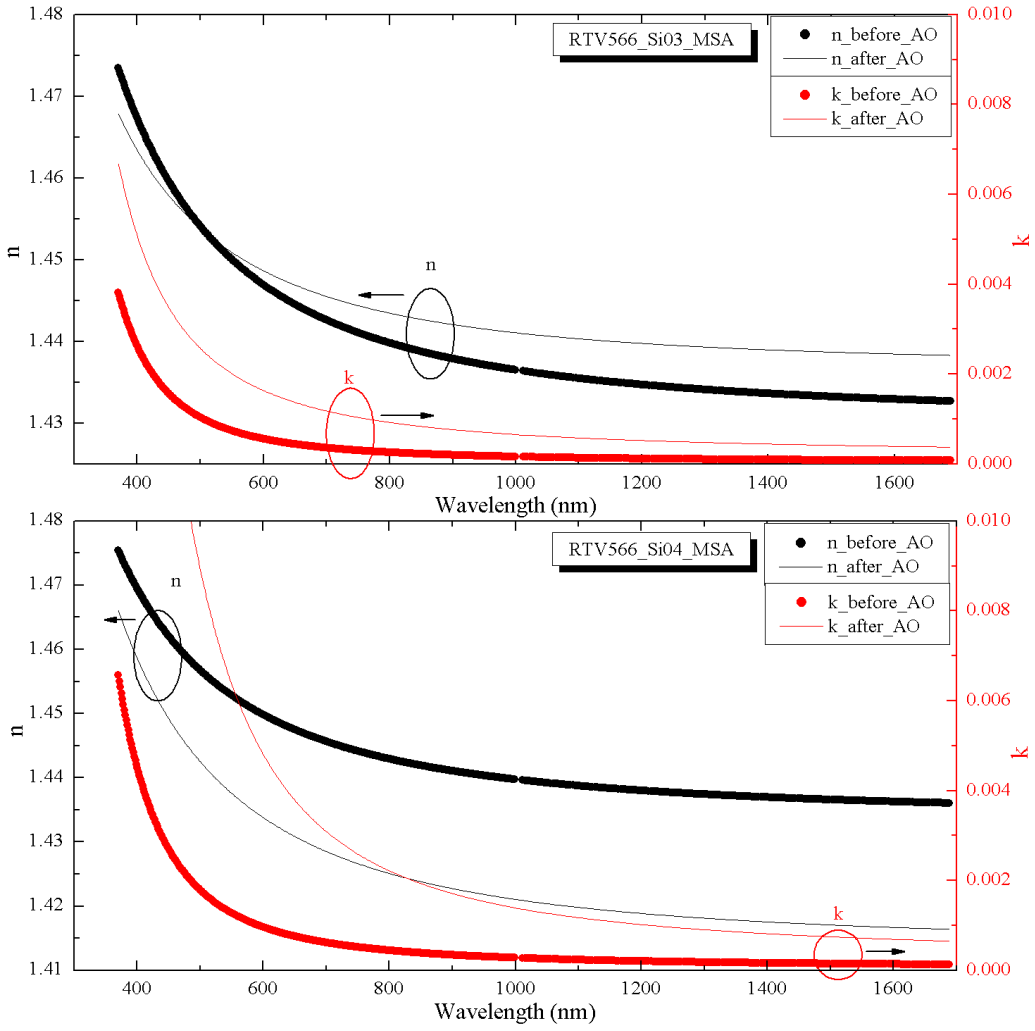

Figure 6.4: RTV566 VCM optical constants before and after AO

In Fig. 6.4, the thick lines represent the optical constants after deposition or before AO exposure, the thin lines represent the optical constants after AO exposure. The black lines are refractive index while the red lines are extinction coefficient.

For Si03, the biggest difference between n before and after AO exposure exists at a wavelength of 1690nm, which is approximately 0.39% difference. For Si04, the

biggest difference between n before and after AO exposure also exists at a wavelength of 1690nm, and is approximately 1.38%. It also can be seen that n values for Si03 and Si04 are almost the same before AO exposure. Therefore, it can be concluded that the refractive index doesn't change much through the AO exposure.

For Si03, the biggest change in k as a result of AO exposure is approximately a factor of 1.75 at a wavelength of 370nm. For Si04, the biggest change in k as a result of AO exposure is approximately a factor of 5 at a wavelength of 370nm. The key result here is that k increases with AO exposure, and the most significant increases occur at shorter wavelengths.

6.2 The effect of simultaneous AO exposure and photofixing RTV566 VCM deposition

In this section, the AO exposure and photofixing deposition occurred simultaneously. A virgin silicon wafer substrate was placed in the chamber for both atomic oxygen bombardment and VCM deposition. The optical constants of the films is determined by *ex-situ* ellipsometry after removal from the chamber.

The previous section covering VCM film deposition in a vacuum environment followed by AO exposure has performed by others as well [22] [51] [17] [19] [13] [6]. However, VCM deposition with simultaneous AO exposure has not been reported in the literature to date. The following sections present the results of photofixed VCM film deposition in the presence of AO.

6.2.1 Experimental Apparatus

Simultaneous AO exposure and VCM film deposition occurred in the chamber setup as shown in Fig. 6.5.

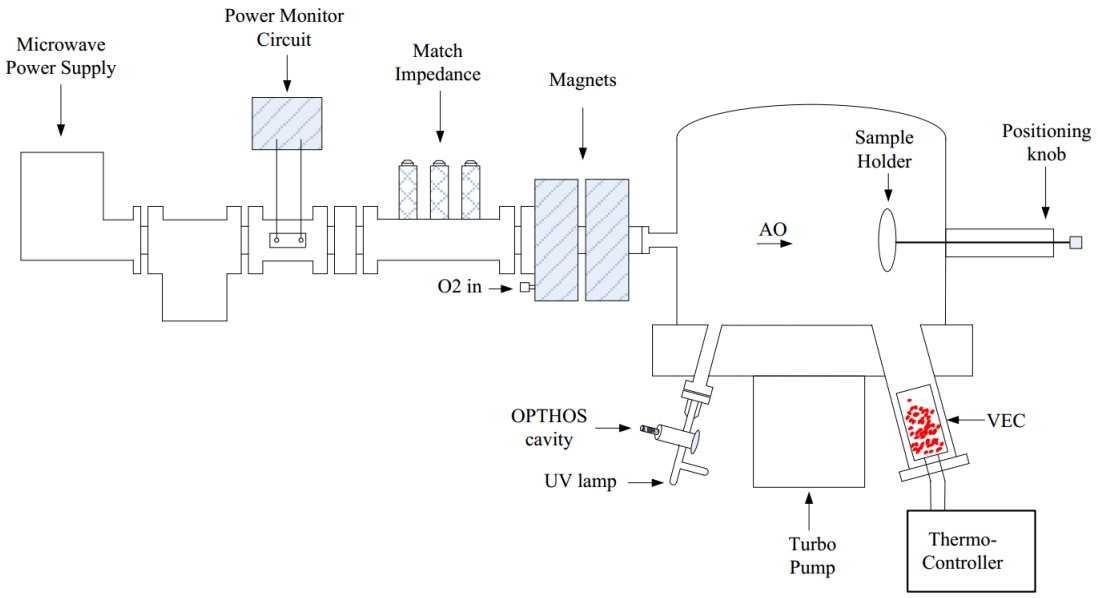

Figure 6.5: Simultaneous AO and photofixing chamber

The chamber is a modified version of the system seen in Fig. 6.2. A UV lamp and effusion cell (VEC) are added as seen in Fig. 6.5. The UV lamp setup and power output are identical to that used in the VCM deposition chamber setup described in the previous section (Fig. 6.1). The linear feed-through was used to position the sample holder to receive both the UV beam and the evaporation material from the effusion cell.

Typical operating condition for this chamber are 400W input power, gas flow 10 sccm O_2, and pressure $9 \times 10^{-4} Torr$. During the VCM film deposition, an AO flux of approximately 1×10^{16} oxygen atoms/$cm^2 \cdot sec$ by the ECR discharge system incident on the sample while being illuminated by the UV photons.

6.2.2 Sample preparation

In this section, a virgin silicon wafer was cleaned and prepared as discussed previously. In this simultaneous growth and AO exposure experimental apparatus (Fig. 6.5),

the RTV566 materials are cut into cubes and contained within the VEC, where the temperature is set to $100°C$.

After aligning the silicon wafer on the sample holder, the chamber was then pumped down for more than 12 hours to a base pressure around 1×10^{-6}Torr, the VEC was heated to $100°C$, the AO plasma initiated and the UV lamp ignited. When the deposition and AO exposure finished, the VCM sample is taken out for ellipsometric characterization.

6.2.3 Fitting procedure for VCM films

Two sample VCM films of RTV566 material were made in this section as well. Before each deposition, the native oxide thickness on the silicon wafer was derived from ellipsometric characterization. Then the silicon wafer was put into the chamber for deposition simultaneously with AO exposure. After exposure, the sample was removed for *ex-situ* ellipsometric measurement. Three spots were tested at multiple angles in the M2000 with focusing probes on. The optical model for the sample is 'Cauchy layer on native oxide on silicon wafer'. By appending three data sets into one analysis window, multi-sample analysis (MSA) can be performed to obtain the average optical constants of the film along with the thicknesses at the three locations.

The fitting procedure for VCM films with AO exposure is illustrated in Fig. 6.6.

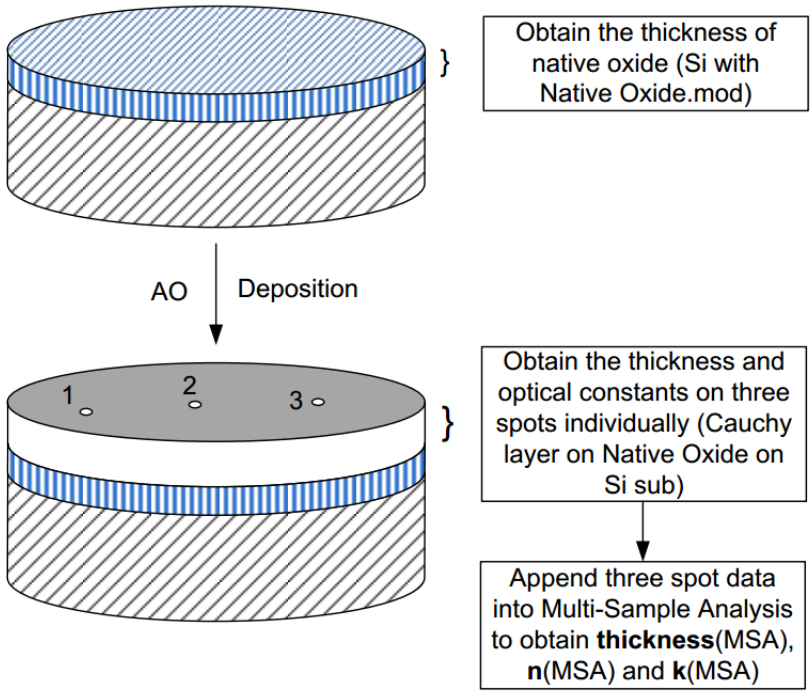

Figure 6.6: Fitting procedure for VCM films with AO exposure

6.2.4 Simultaneous AO exposure and photofixing RTV566 VCM films results

The ellipsometric results for two samples of RTV566 (Si48 and Si49) are shown in Table 6.2

Table 6.2: RTV566 Tests Results List - AO Part2

Label	Spot	Nat. Oxide	Duration	MSE	Film (nm)
Si48	1	2.3nm	2 hours	3.512	17.91
	2			3.423	18.13
	3			3.484	17.48
Si49	1	2.39nm	3 hours	3.692	24.32
	2			3.67	24.52
	3			3.705	24.22

Under the same experimental condition (same oxygen flow rate - 10sccm, same UV lamp power), the film thickness of Si49 is approximately 6nm more than the thickness of Si48 due to its longer deposition duration. The average deposition rate for Si48 is approximately $17.84nm/2hours \approx 9nm/hour$, the average deposition rate for Si49 is approximately $24.35nm/3hours \approx 8nm/hour$. The deposition rates are very close indicating the process is consistent from run to run.

The VASE data fitting result for RTV566 Si48 and Si49 are shown in Fig. H.1 and Fig. H.2.

The optical constants of each spot on RTV566 VCM films with AO exposure for Si48 and Si49 are shown in Fig. F.1 and Fig. F.2

The optical constants of multi-sample analysis for three spots (n_{MSA}, k_{MSA}) for Si48 and Si49 are shown in Fig. 6.7.

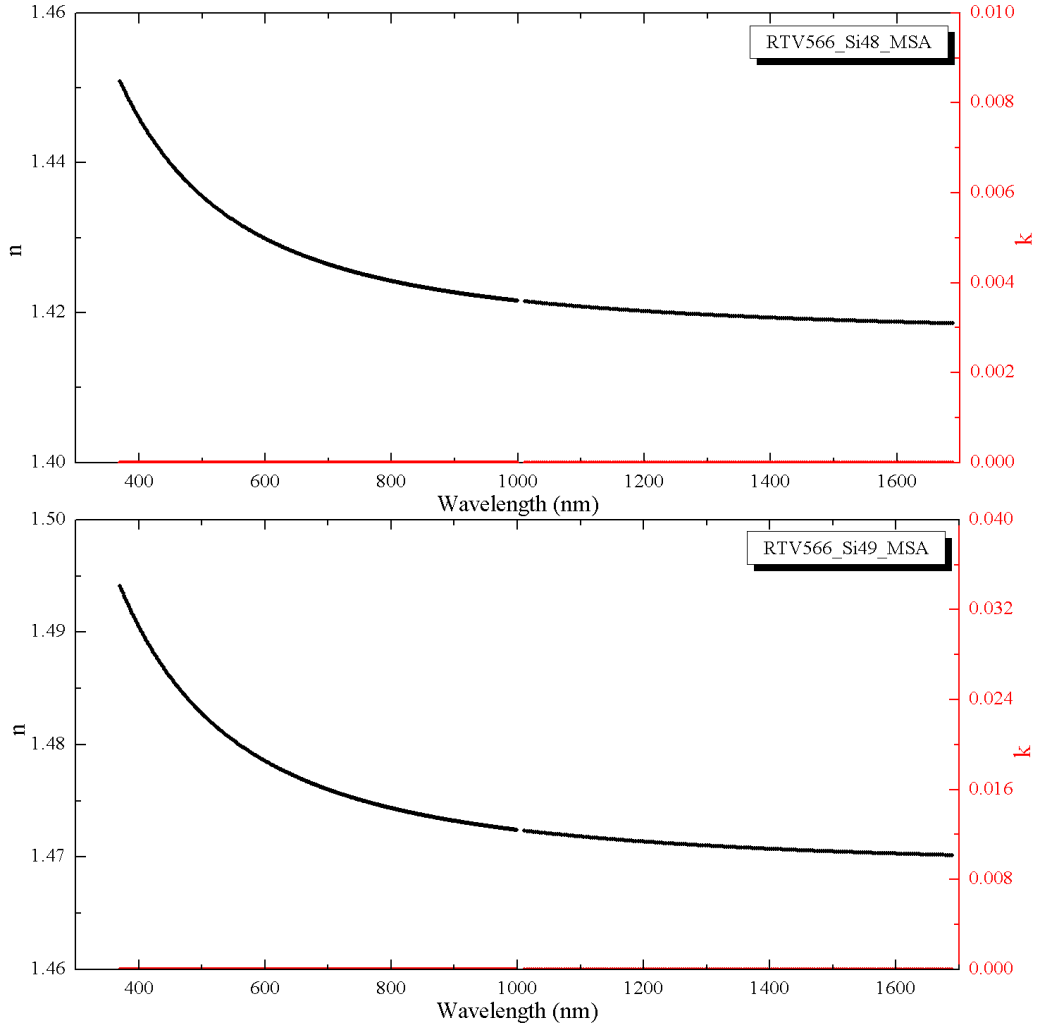

Figure 6.7: RTV566 VCM optical constants with AO exposure

Although not identical, the optical constants of these two films are very similar in that the extinction coefficient is essentially zero, and the index of refraction differs by less than 3.6% at any given wavelength.

6.3 Comparison of AO effects on existing films with AO effects during growth

The photo-fixed VCM films deposited under vacuum in the first section simulates contamination in GEO, while simultaneous VCM deposition and AO exposure simulates contamination in LEO which has been performed in the second section.

6.3.1 GEO films without AO exposure compared to LEO films

The optical constants of VCM films without AO exposure in GEO and LEO simulation are compared in Fig. 6.8.

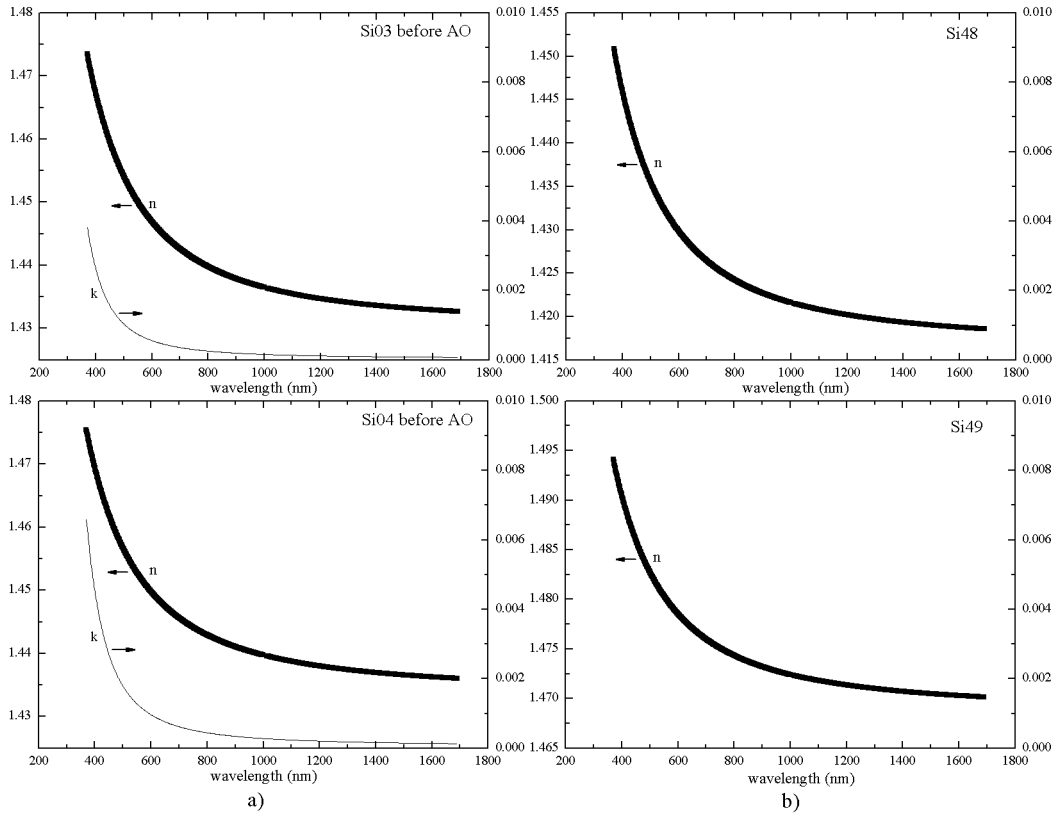

Figure 6.8: GEO LEO simulated VCM optical constants. a). GEO films without AO b). LEO films

The deposited VCM films simulate the photofixing films in GEO environment without AO exposure. It is clear that the extinction coefficient of the GEO films is non-zero throughout the spectral range with the largest values existing in the UV region while the LEO films are essentially transparent across the spectral range. The index of refraction is similar for both sets of films.

6.3.2 GEO films with AO exposure against LEO films

The optical constants of VCM films grown in GEO simulation followed by AO exposure and LEO simulation are compared in Fig. 6.9.

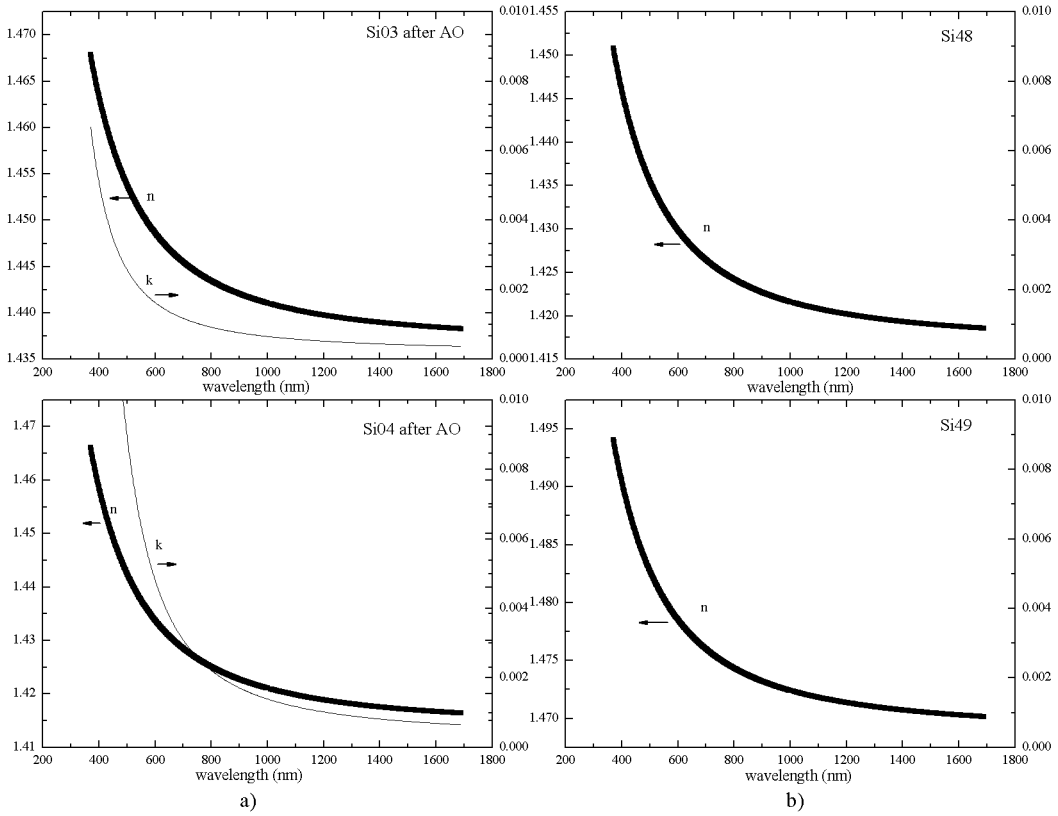

Figure 6.9: GEO LEO simulated VCM optical constants. a). GEO films with AO b). LEO films

The optical constants of Si03 and Si04 (GEO films) after AO exposure are shown on the left, the optical constants of Si48 and Si49 are shown on the right.

In GEO simulated results, a clear non-zero extinction coefficient exists, however the extinction coefficient is zero for films deposited with simultaneous AO exposure. The key result here is that sequential photofixing and AO exposure do not yield the same films as simultaneous photofixing and AO exposure.

6.4 Summary

The GEO films are optically reproducible to within less than 1%. These films have a non-zero extinction coefficient throughout the UV to near IR spectral region, with maximum values in the UV range. This type of film can substantially alter satellite solar cell performance by absorbing energetic UV photons. AO exposure has little effect on the GEO film index of refraction, but substantially increases the extinction coefficient in the UV region. The LEO films are also optically reproducible to within 3%, however they exhibit a zero extinction coefficient across the measured spectral range, in direct contrast to the unexposed/exposed GEO films.

Chapter 7

Conclusions

7.1 Summary of the present work

RTV materials are commonly used to bond components of communication satellites and other types of spacecraft. The elevated satellite operating temperature will cause the species within the RTV material to outgas Volatile Condensable Material (VCM) that deposits or re-condenses onto spacecraft surfaces, therefore degrading the performance of many components and shortening the lifetime of spacecraft.

In this dissertation, a cryogenic shrouded chamber was used to simulate the effects of the GEO environment in a laboratory system. A quartz crystal microbalance (QCM) was used to monitor the volatile condensable material (VCM) mass accumulation from the outgassing of heated silicone materials. Meanwhile, the optical properties of cryogenic temperature deposited VCM films were analyzed by the *in-situ* ellipsometer.

RTV566 silicone VCM films were deposited on QCM substrate at three different temperatures while *in-situ* ellipsometry collected the optical data at the same time. The QTGA data indicates that the 120K VCM is different from the the 150K VCM and the 180K VCM. The 120K VCM QTGA data clearly shows a peak at 140K and one at 273K, which has been shown to be water. An initial and in-depth analysis was

performed as described below:

- Initial analysis. Assuming a homogeneous film, the Cauchy model and Gen-Osc model provided a reasonably good fit to the data for 120K VCM, and the Wvl-ByWvl model further improved the fitting results while still maintaining the K-K relationship. The end point optical constants of 120K VCM do not adequately fit the 150K VCM end point, however, the end point optical constants of the 150K VCM can be fit to the 180K VCM with a reasonable MSE.

- Although the homogeneous assumption yielded reasonable results, at each condensation temperature the SE calculated film thickness was less than the QCM film thickness during the early stages of deposition. Possible reasons for this include:

    1. Very thin films at beginning time points when optical model may not be that accurate.

    2. In 120K VCM, the existence of ice will result in an optically inhomogeneous film.

    3. Early stages of deposition are commonly driven by island formation, resulting in porous films during the early stages of growth. This can yield an inhomogeneous film.

- In-depth analysis:

    1. For the 120K VCM, the QTGA analysis clearly shows the film contains ice as well as a condensed effluent. An EMA model including ice and the end point WvlByWvl 120K VCM model optical constants can be made to fit the QCM data exactly, with no modification to the film density.

This is a result of the fact that the density of ice is essentially $1 gm/cm^3$. This approach links the QTGA data, QCM and SE data in a consistent manner. It should be pointed out that in Chapter 4 ice has been shown to condense as a homogeneous film without voids, even from the initial stages of growth.

2. For the 150K VCM and the 180K VCM, the QTGA data does not indicate ice is present in the film, therefore a more typical effluent condensation process is expected to occur. This process is driven by island nucleation, [47] [48] followed by coalescence into a continuous film. Clearly island nucleation gives rise to a porous film during the early stages of deposition. A self-consistent approach employing the QCM ad SE data was developed to yield a potentially more realistic result. The self-consistent approach yields the fact that void fraction decreases with time and thickness growth rate slows down during later stages of deposition. This is in agreement with existing results [45].

In order to study the LEO environment, an electron cyclotron resonance (ECR) based system was used to simulate the effect of AO in a laboratory system. The first experiment was designed to show the effect of AO on an existing photofixed VCM, while the second set of experiments was designed to simulate the LEO environment by photofixing VCM films in the presence of AO.

These results are summarized below:

- The GEO films have a non-zero extinction coefficient from the UV through the near IR spectral region. The AO exposure has little effect on the index of refraction of the GEO films, but can increase the extinction coefficient values.

- The GEO films are etched by the AO, which may indicate they can be completely removed.

- For the first time VCM photofixed films were deposited in an AO atmosphere, accurately simulating the LEO environment. In contrast to the GEO films exposed to AO, the LEO films had essentially a zero extinction coefficient. This demonstrates that photofixed VCM films in LEO cannot be accurately simulated by photofixing films in vacuum followed by AO exposure.

7.2 Suggested future work

It would be beneficial to quantify the composition of the VCM at various condensation temperatures by Gas Chromatography Mass Spectrometry (GC-MS) since the unidentified peak around 140K of 120K VCM QTGA data does not exist in other two VCMs' QTGA data.

Since the GEO films with AO exposure are optically different from the LEO films, it would also be helpful to investigate the molecular bonds with *ex-situ* IR ellipsometry, in order to understand how AO alters the deposition process.

The various surface temperatures on a satellite in space lead to different outgassing components. This will alter the composition of the condensed VCM films. A study of the condensed VCM as a function of outgassing temperature will indicate the importance of this effect.

Appendix A

Form Factor

Form factor (or view factor) F_{12} is the fraction of energy $\frac{E_1}{E_2}$from surface 1 which emit or reflect energy (E_1), that directly impinges on surface 2 which absorb or reflect energy (E_2). The analytical expression can be deduced from following. From Fig. A.1 the geometry of two infinitesimal surface patches (dA_1 and dA_2) for defining view factors, the distance between these two patch is L, and their respective tilting angle to normals are α_1 and α_2, with $0 \leq \alpha_1 \leq \pi/2$ and $0 \leq \alpha_2 \leq \pi/2$.

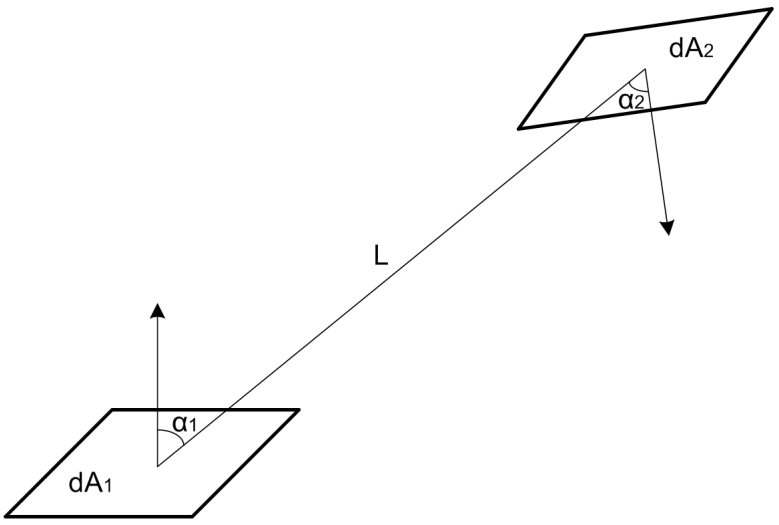

Figure A.1: Geometry for form factor definition

The view factor of two differential areas of dA_1 and dA_2 at a distance L is given

by

$$F_{1\to 2} = \frac{cos\alpha_1 cos\alpha_2}{\pi r^2} dA_2 = \frac{1}{A_1}\int_{A_1}(\int_{A_2} \frac{cos\alpha_1 cos\alpha_2}{\pi r^2} dA_2) dA_1$$

The emitting surface 1 is isothermal, opaque, and Lambertian (cosine flux distribution), form factor can be calculated by integration. For the case in CATC, the distance between VEC orifice and QCM surface is $L = 13 \times 25.4mm \simeq 330mm$, the radius of VEC orifice is $R_1 = 22.5mm$, the radius of QCM expose crystal is $R_2 = 5.9mm$

For parallel configuration, the orifice of VEC can be considered as disk-like emitter, the QCM crystal can also be considered as disk-like accpetor, which this case can be drawn in the figure below A.2

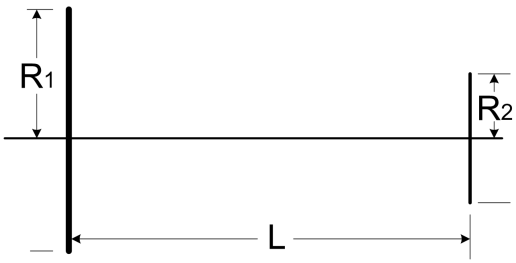

Figure A.2: Unequal discs case

The form factor is

$$F_{1\to 2} = \frac{x - y}{2}$$

where $x = 1 + \frac{1}{r_1^2} + \frac{r_2^2}{r_1^2}$, and $y = \sqrt{x^2 - 4\frac{r_2^2}{r_1^2}}$ and $r_1 = R_1/L$, $r_2 = R_2/L$

Using the configuration parameters in above, the form factor is calculated as $F_{1\to 2} = 3.18 \times 10^{-4}$

Appendix B

Outgassing Model

Outgassing data can be analyzed with diffusion theory which has been examined thoroughly with physical equations. Outgassing in vacuum occurs by diffusion of principle outgassing species through the bulk material to the free surface, where they evaporate. The outgassing rate data can be modeled by diffusion theory to yield diffusion properties of each species. Bulk diffusion is assumed as predominant mechanism to determine the diffusion properties and furthermore to compare measured and modeled outgassing rates of samples of different temperature.

The outgassing rate, R_{og}, in mass per unit area per unit time leaving the free surface, is given by:

$$R_{og} = -D\frac{dc}{dx} \tag{B.1}$$

where D is the diffusion coefficient, which depends on temperature exponentially,

$$D = D_0 exp(-E/kT)$$

where k is the Boltzmann constant; E is the activation energy for diffusion and D_0 is a constant.

Equation B.1 can be solved for boundary conditions to determine the concentration distribution as a function of time and position. In this silicone rubber diffusion model, the diffusive flow is assumed to be one-dimensional in rectangular coordinates as shown in Fig. B.1

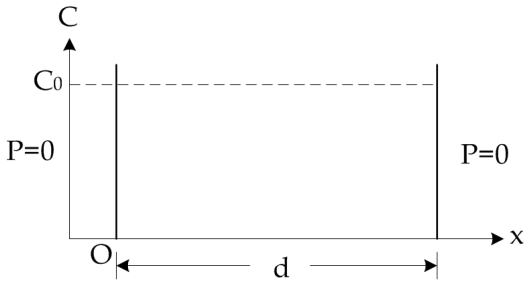

Figure B.1: Bulk diffusion in plane of thickness d

By Fick's second law, diffusion of one species molecules through a bulk can be expressed as,

$$\frac{\partial C}{\partial t} = -D\frac{\partial^2 C}{\partial x^2} \tag{B.2}$$

The boundary conditions are:

$$C = C_0 \quad 0 < x < d \quad t = 0$$

$$C = 0 \quad x = 0, x = d \quad t > 0$$

The outgassing rate at the free surface $x = d$, can be solved as

$$R_{og} = D(\frac{\partial C}{\partial x})_{x=d} = \frac{2C_0 D}{d}\sum_{i=0}^{\infty} exp(-\frac{(2i+1)\pi^2 Dt}{4d^2}) \tag{B.3}$$

According to the large valve of time with respect to $t_0 = \dfrac{2d^2}{\pi^2 D}$, the outgassing rate can be rewritten as

$$R_{og} = \frac{2DC_0}{d} exp(-\frac{\pi^2 D}{4d^2}t), \quad t > t_0 \tag{B.4}$$

As time value is larger than t_0, the experimental outgassing data versus time are plotted in log-plot mode, slope of straight line ($\pi^2 D/4d^2$) and intercept on outgassing rate ($2DC_0/d$) can be obtained, from which D and C_0 can be calculated, therefore, molecular species can be deduced from these calculations.

Appendix C

Fitting results for Self Growth In Chapter 4

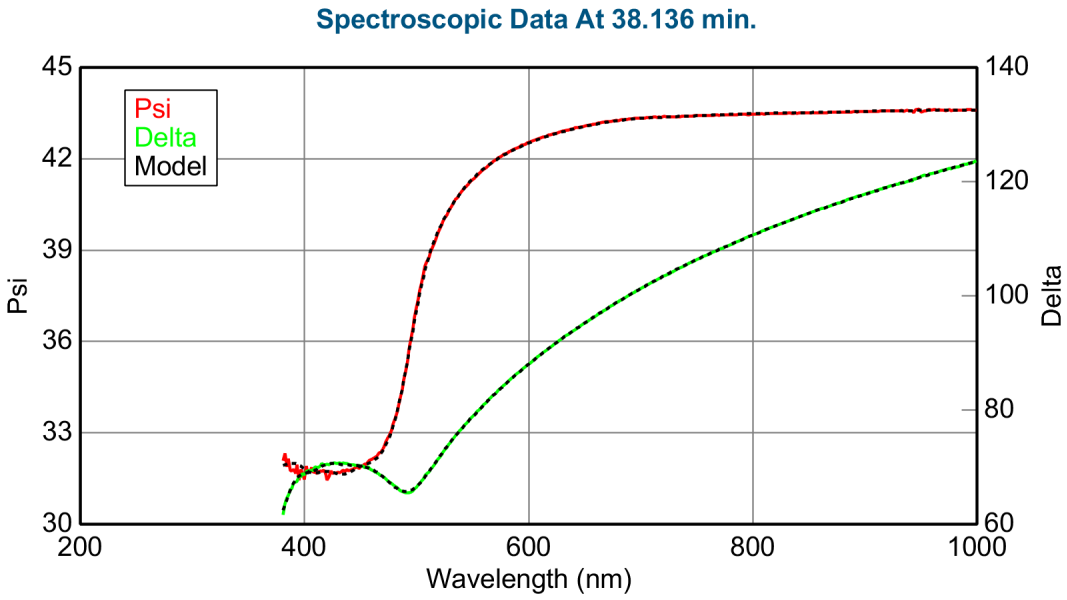

Figure C.1: Fitting results for gold substrate b-2

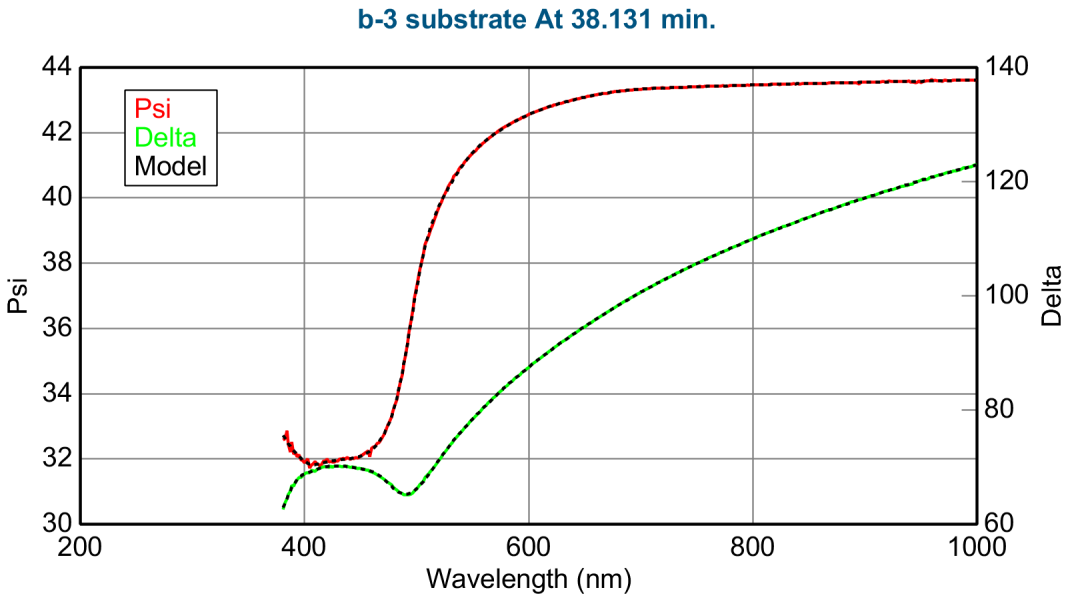

Figure C.2: Fitting results for gold substrate b-3

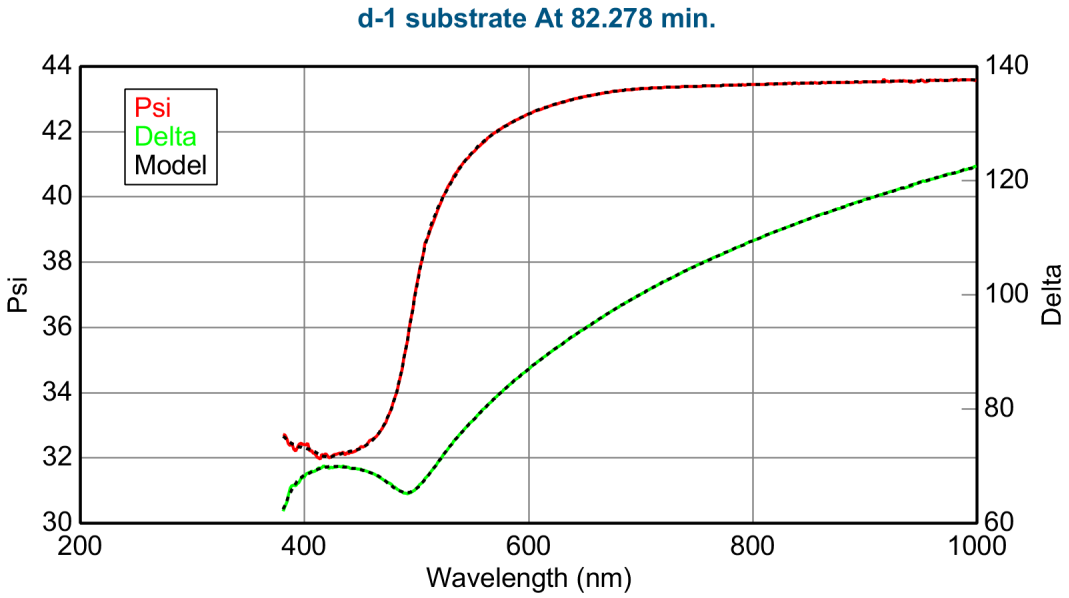

Figure C.3: Fitting results for gold substrate d-1

Appendix D

FTIR and Ramen refenrece results

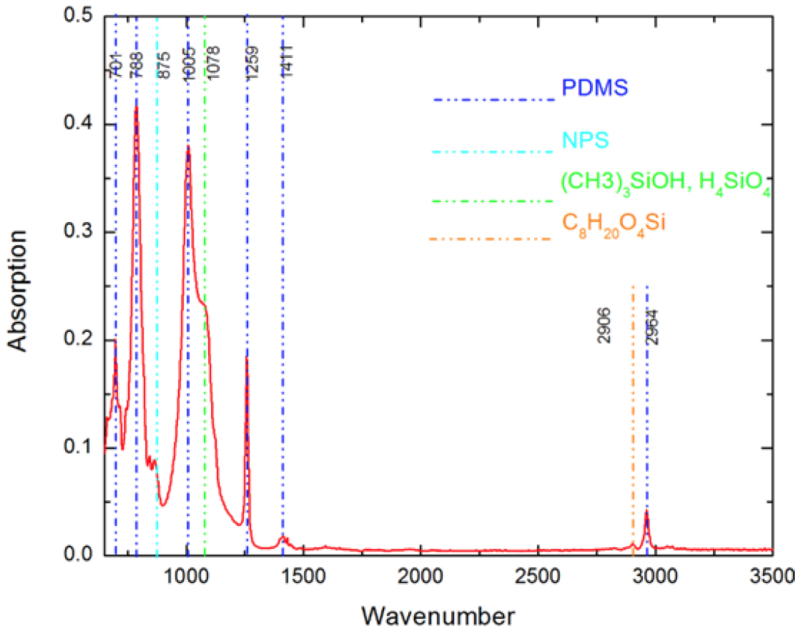

Figure D.1: FTIR spectrum of RTV566 film

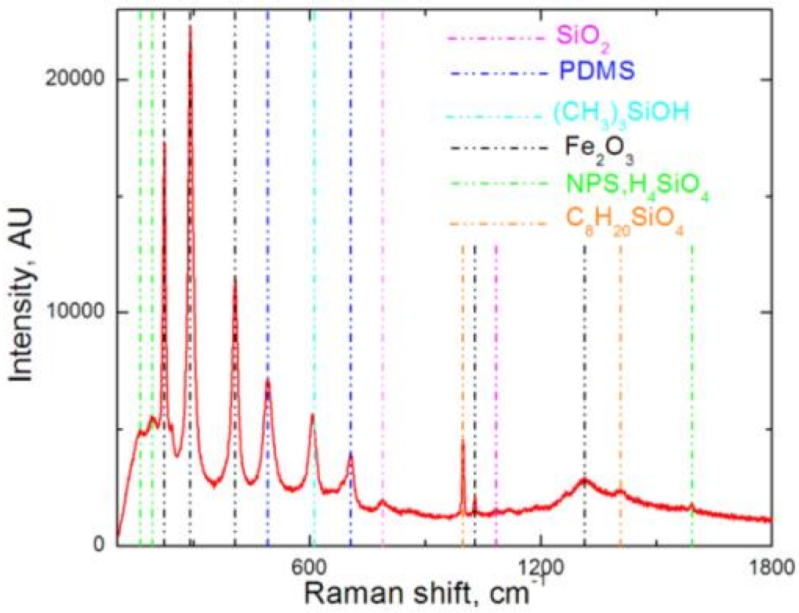

Figure D.2: Raman spectrum of bulk RTV566

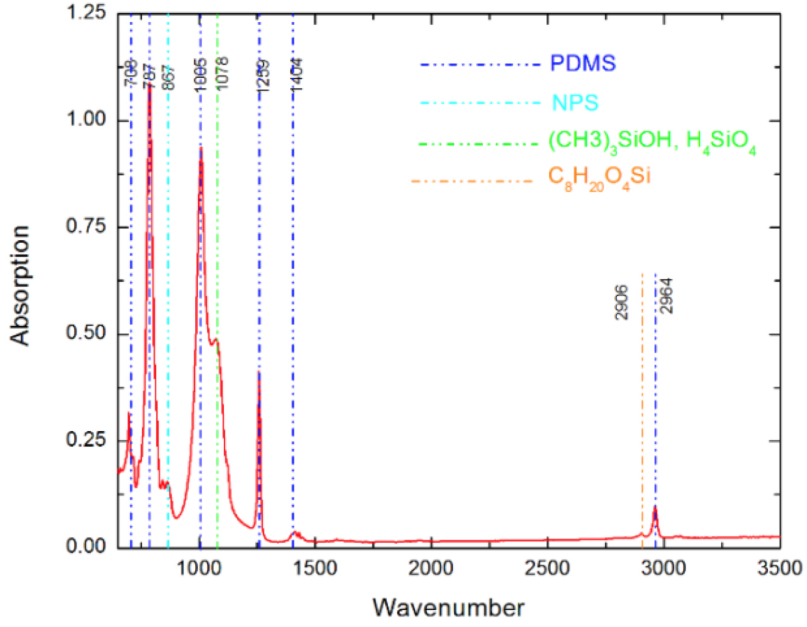

Figure D.3: FTIR spectrum of CV2568 film

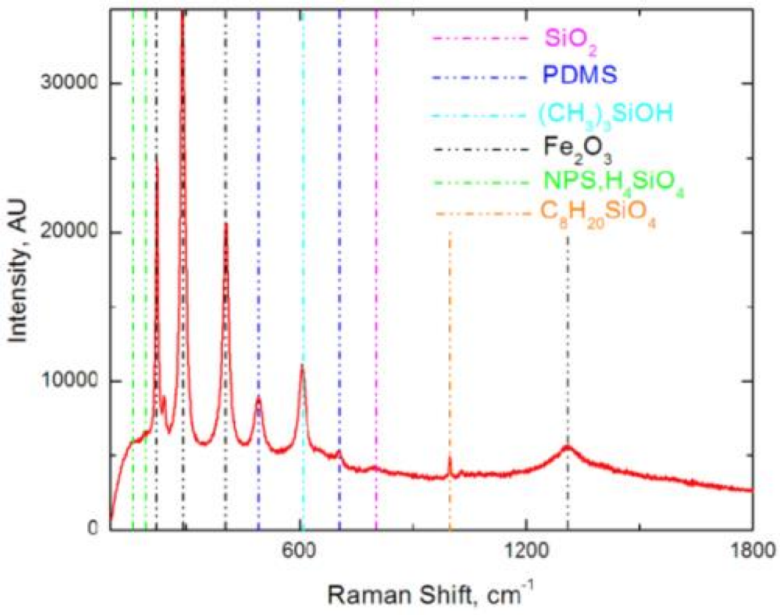

Figure D.4: Raman spectrum of bulk CV2568

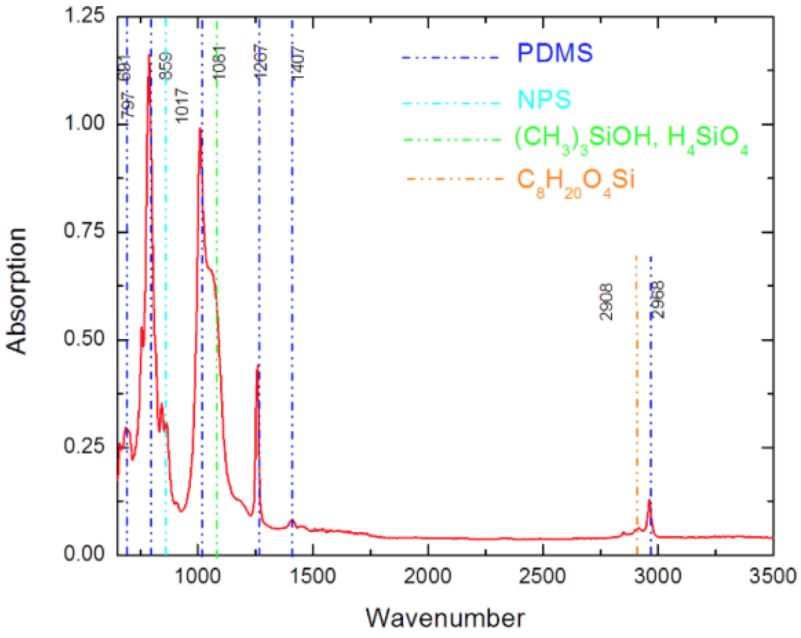

Figure D.5: FTIR spectrum of DC93-500 film

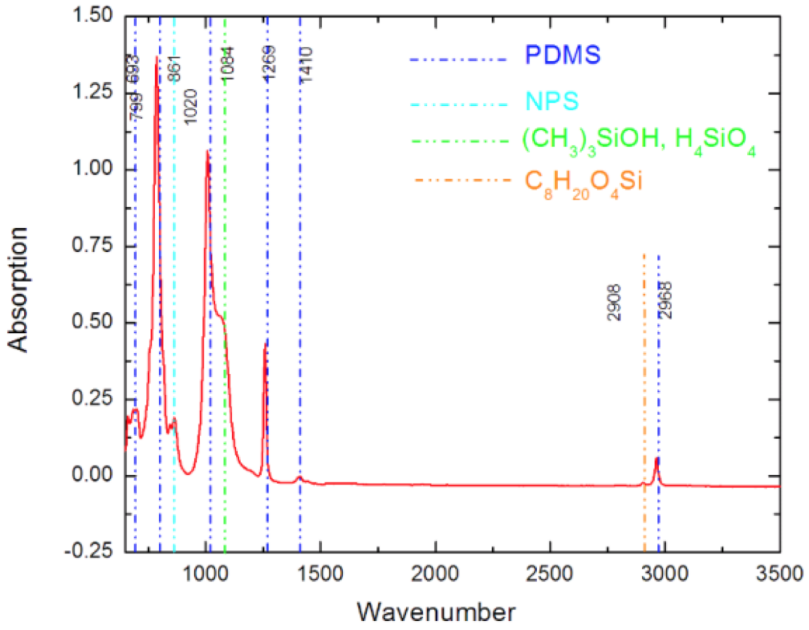

Figure D.6: FTIR spectrum of SCV2590 film

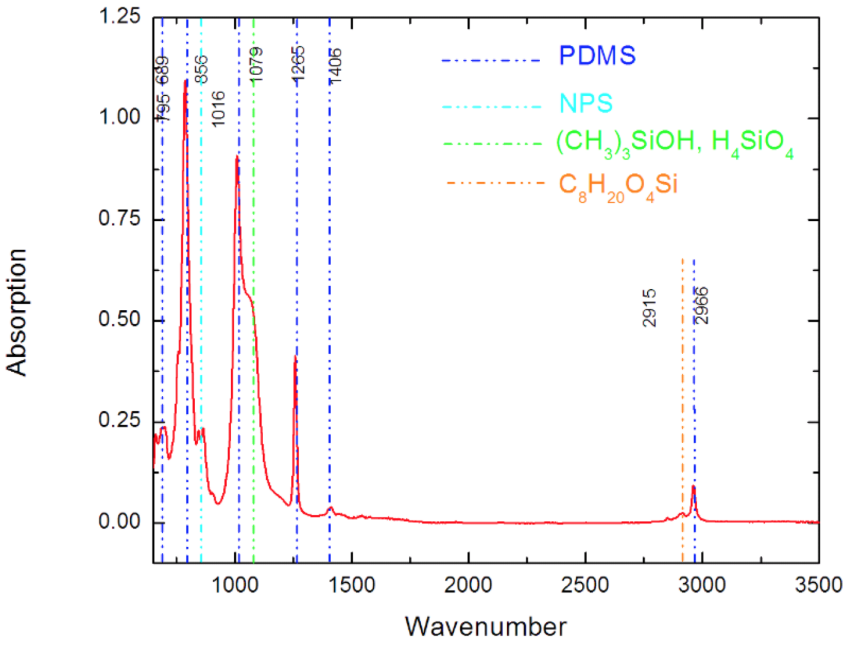

Figure D.7: FTIR spectrum of SCV2590-2 film

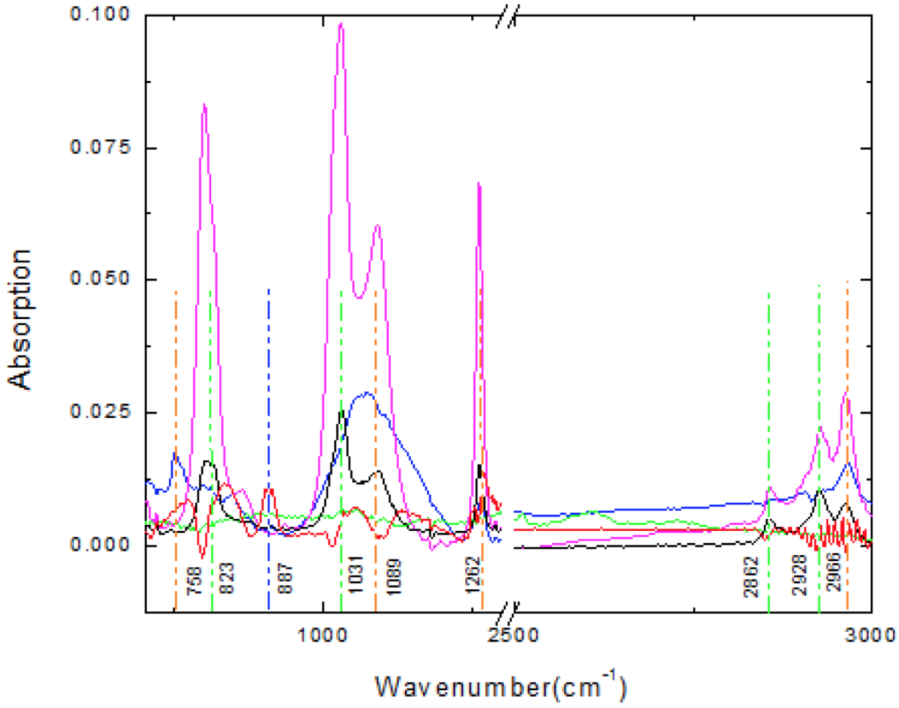

Figure D.8: FTIR spectrum of outgassing products from DC93-500 (blue), SCV2590 (green), SCV2590-2 (red), RTV566 (magenta) and CV2568 (black)

Appendix E

Optical Constants for Chapter 6 Part I

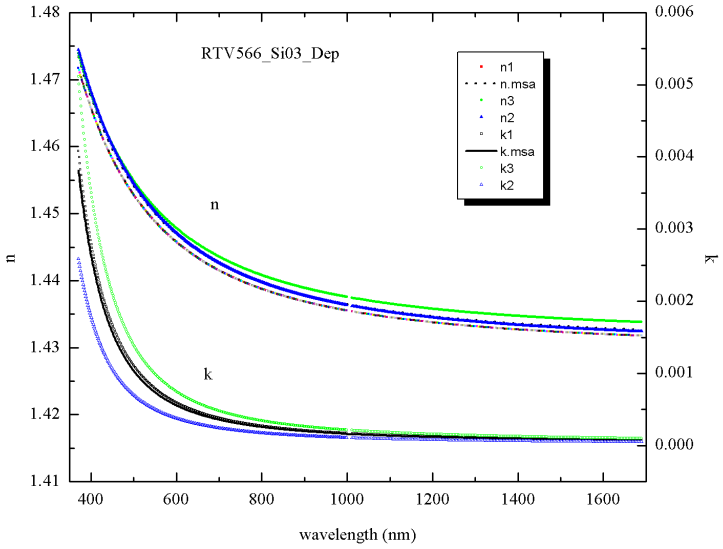

Figure E.1: RTV566 Si03 optical constants before AO

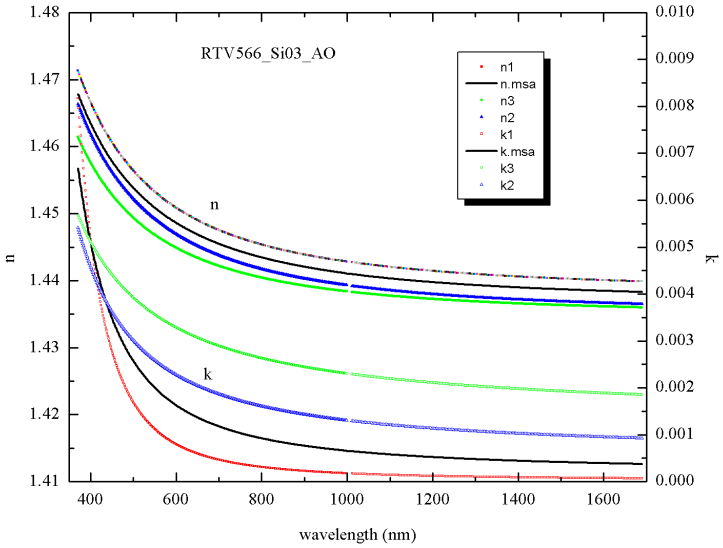

Figure E.2: RTV566 Si03 optical constants after AO

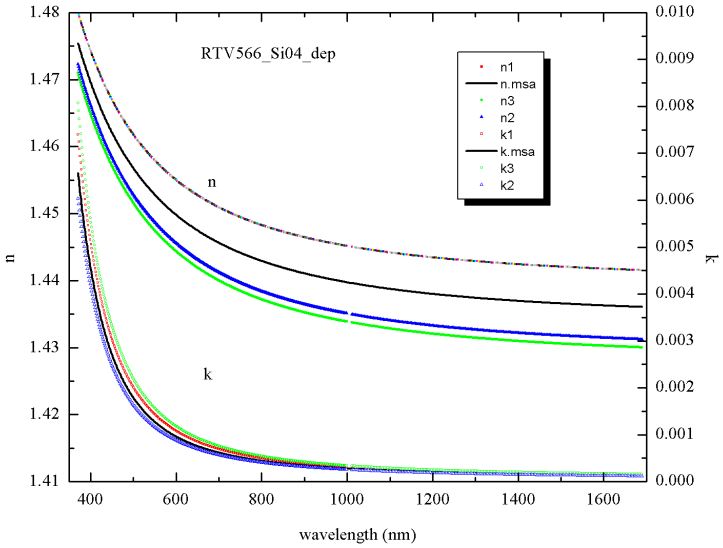

Figure E.3: RTV566 Si04 optical constants before AO

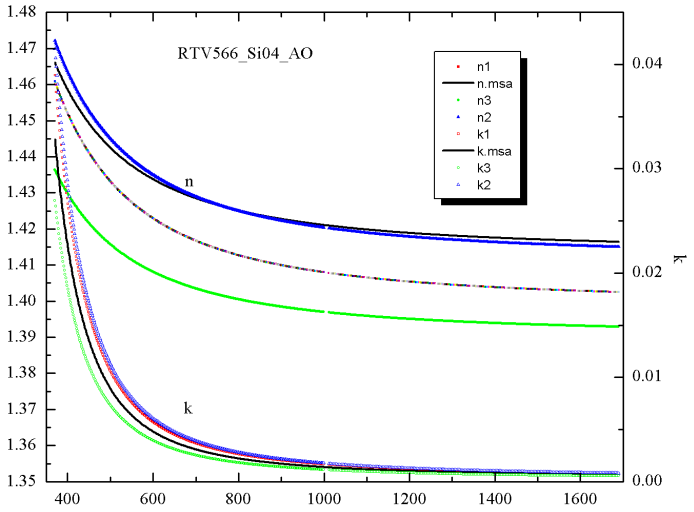

Figure E.4: RTV566 Si04 optical constants after AO

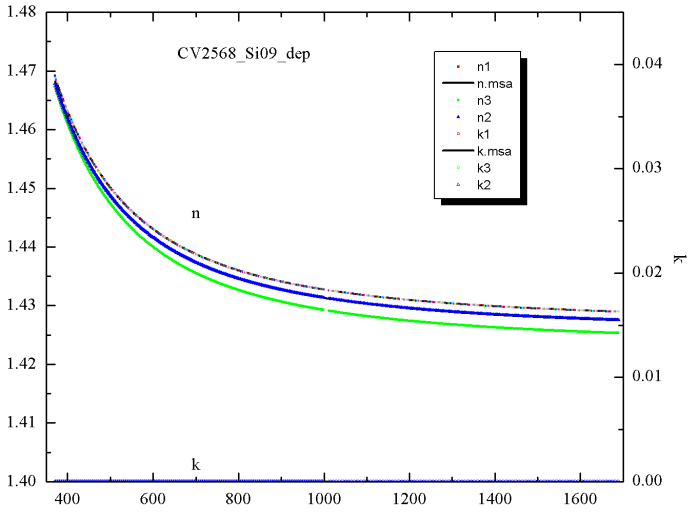

Figure E.5: CV2568 Si09 optical constants after deposition

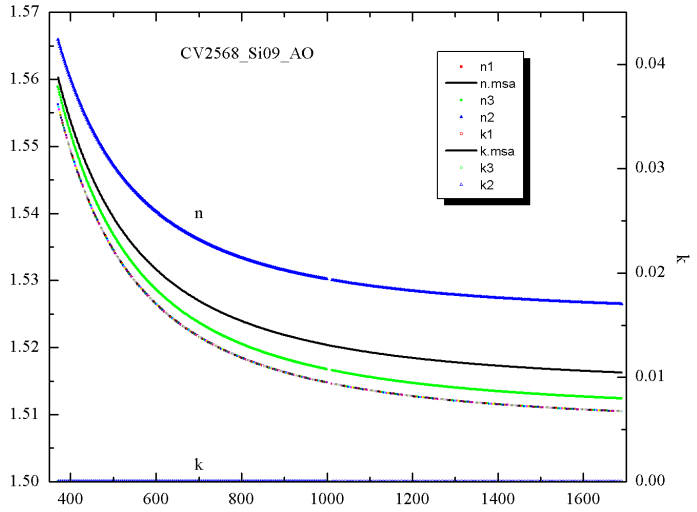

Figure E.6: CV2568 Si09 optical constants after AO

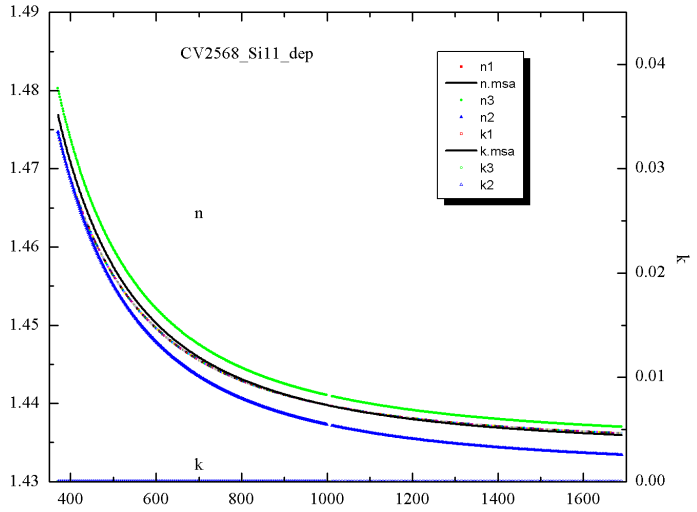

Figure E.7: CV2568 Si11 optical constants after deposition

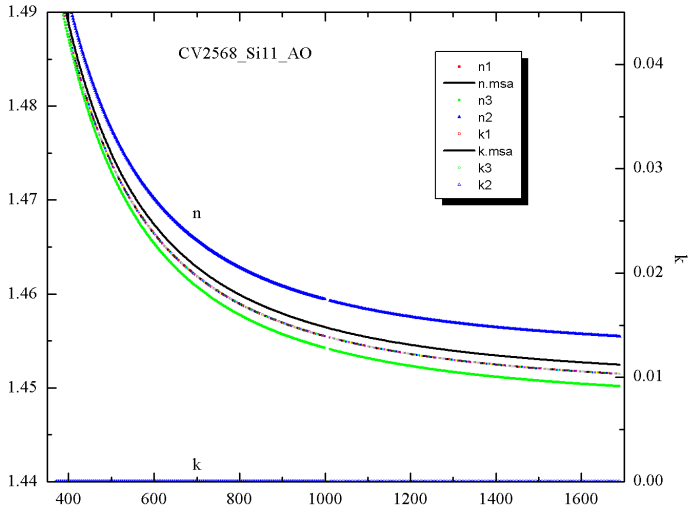

Figure E.8: CV2568 Si11 optical constants after AO

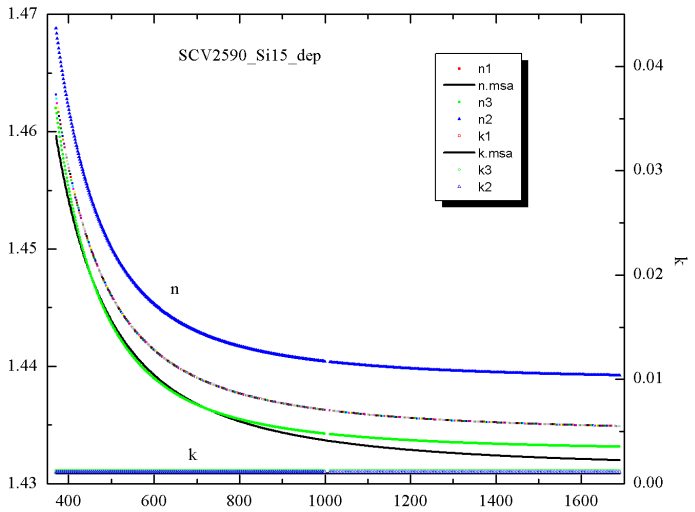

Figure E.9: SCV2590 Si15 optical constants after deposition

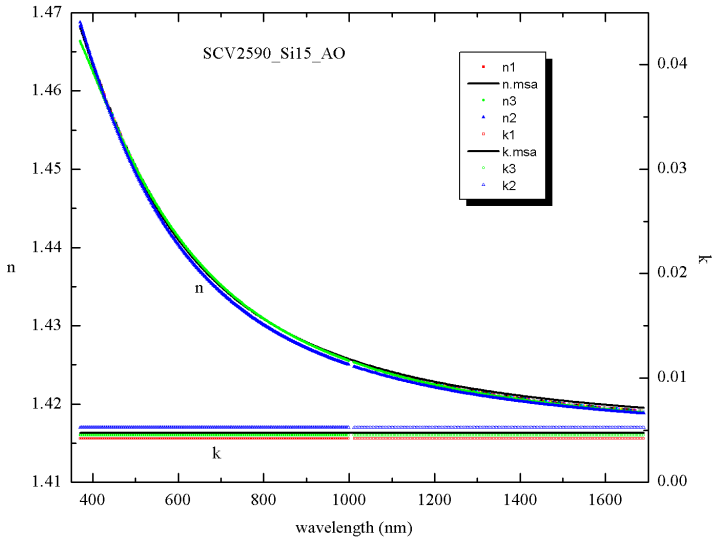

Figure E.10: SCV2590 Si15 optical constants after AO

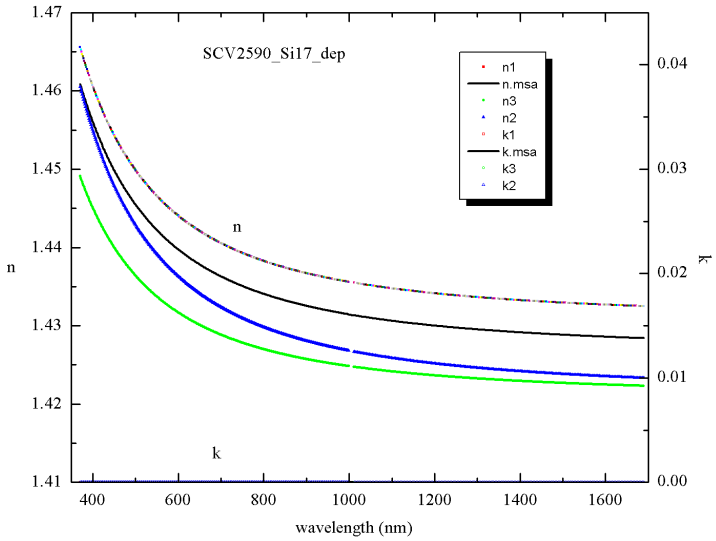

Figure E.11: SCV2590 Si17 optical constants after deposition

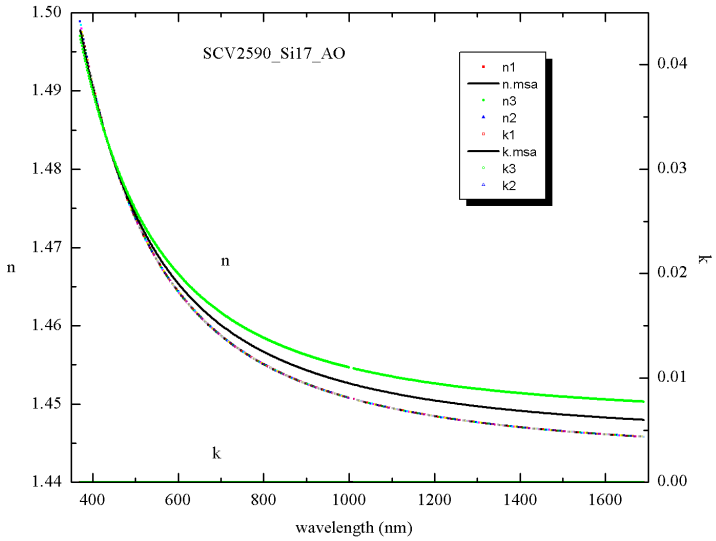

Figure E.12: SCV2590 Si17 optical constants after AO

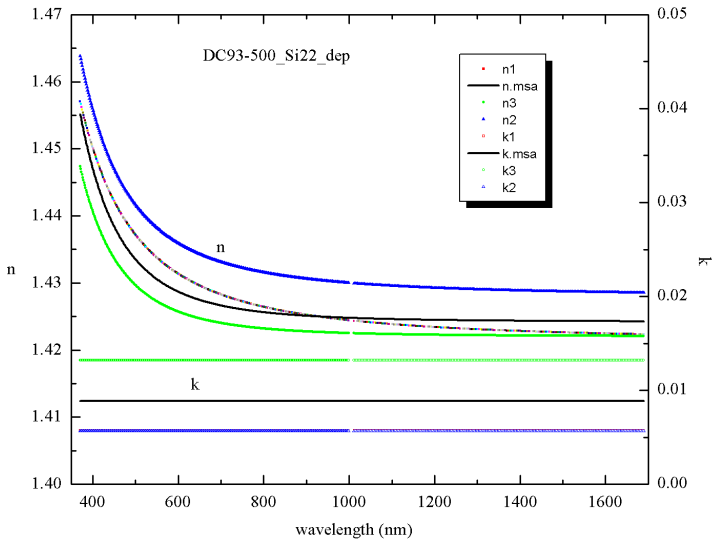

Figure E.13: DC93500 Si22 optical constants after deposition

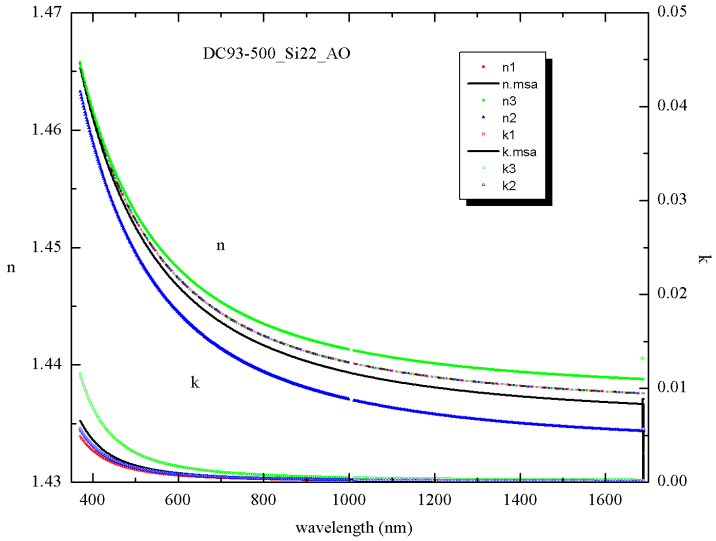

Figure E.14: DC93500 Si22 optical constants after AO

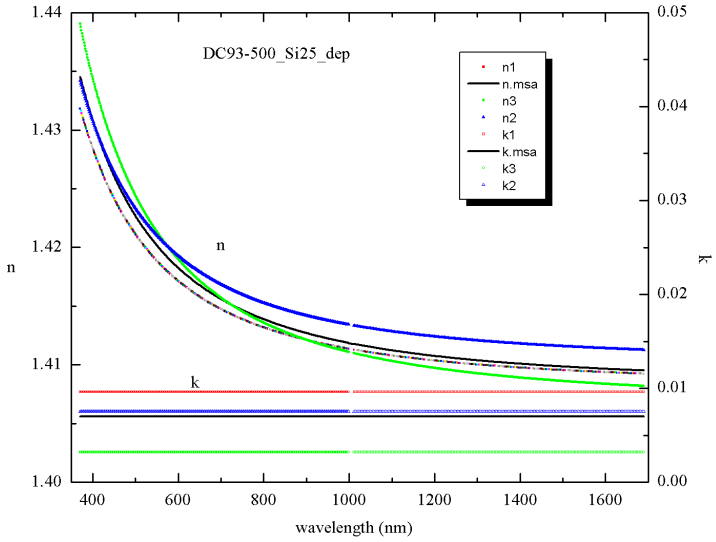

Figure E.15: DC93500 Si25 optical constants after deposition

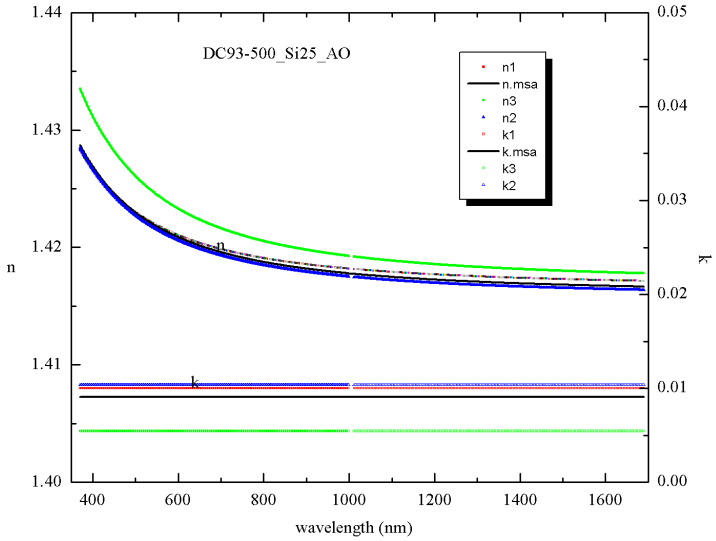

Figure E.16: DC93500 Si25 optical constants after AO

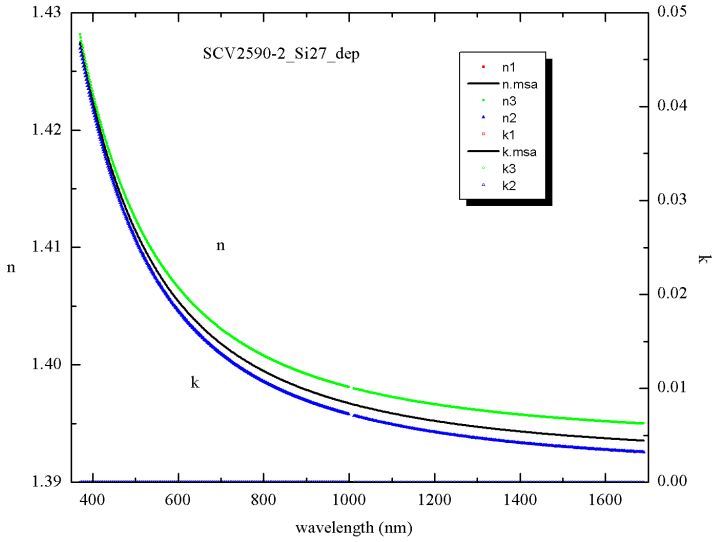

Figure E.17: SCV2590-2 Si27 optical constants after deposition

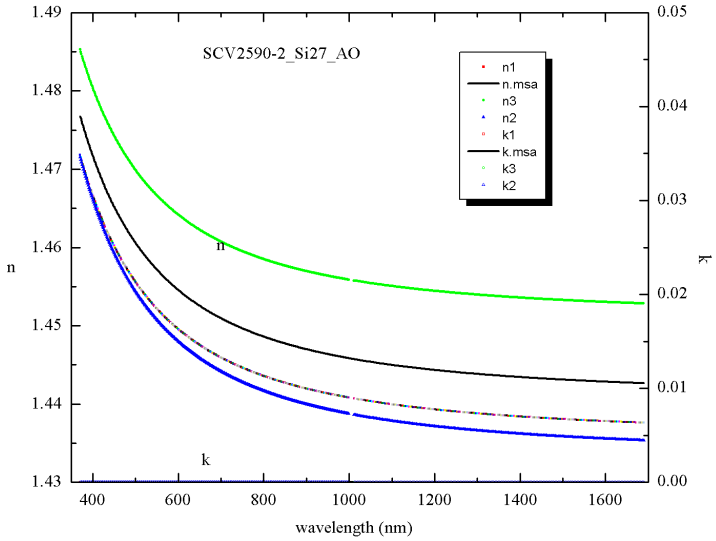

Figure E.18: SCV2590-2 Si27 optical constants after AO

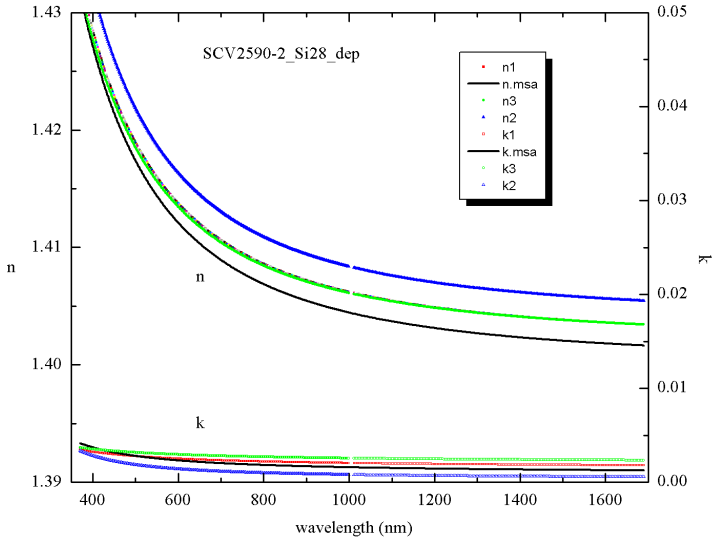

Figure E.19: SCV2590-2 Si28 optical constants after deposition

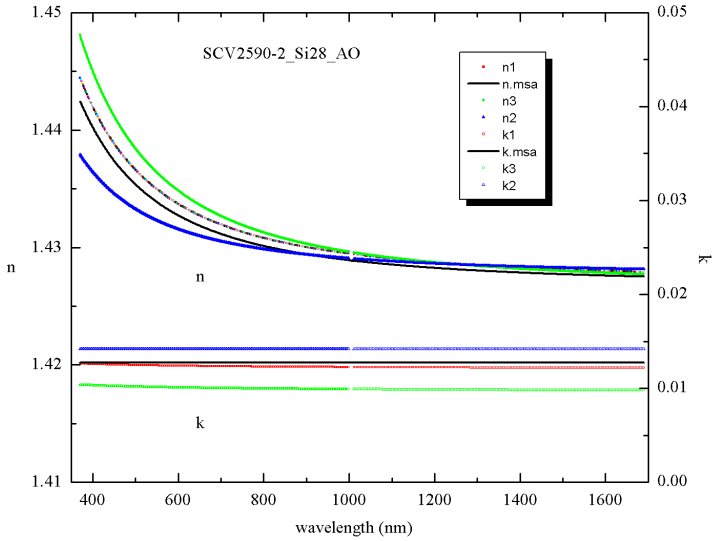

Figure E.20: SCV2590-2 Si28 optical constants after AO

Appendix F

Optical Constants for Chapter 6 Part 2

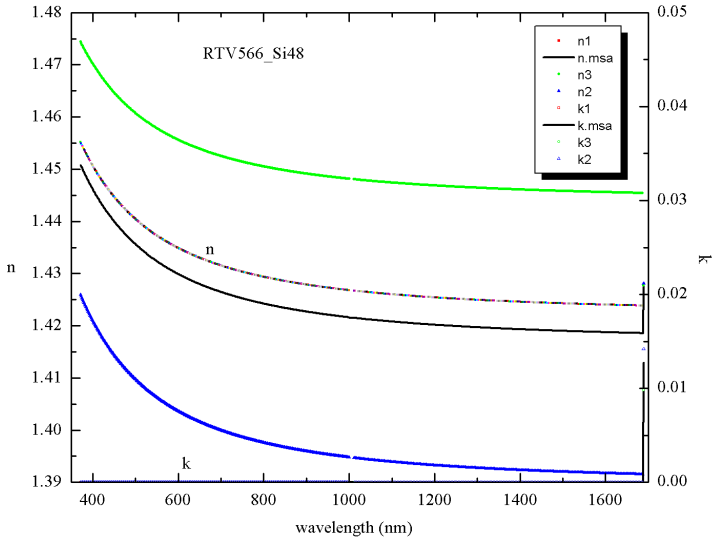

Figure F.1: RTV566 Si48 optical constants after AO and deposition

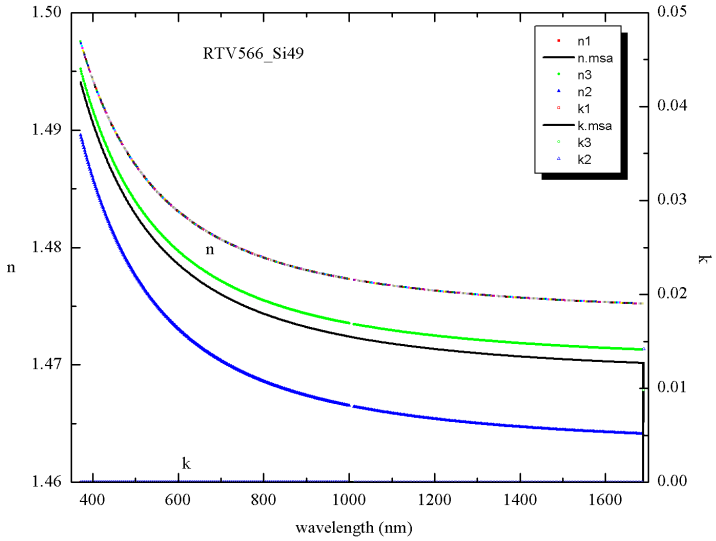

Figure F.2: RTV566 Si49 optical constants after AO and deposition

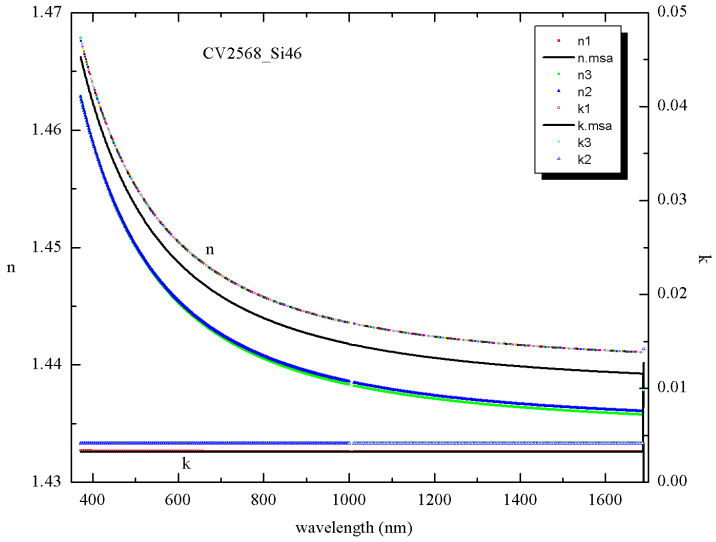

Figure F.3: CV2568 Si46 optical constants after AO and deposition

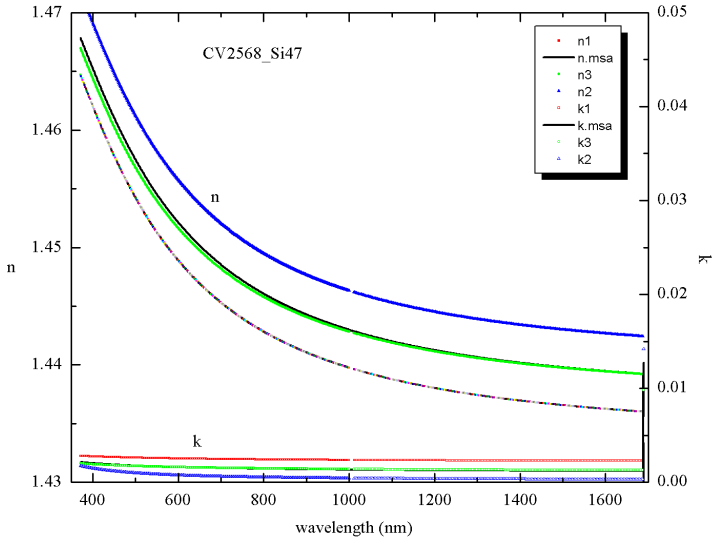

Figure F.4: CV2568 Si47 optical constants after AO and deposition

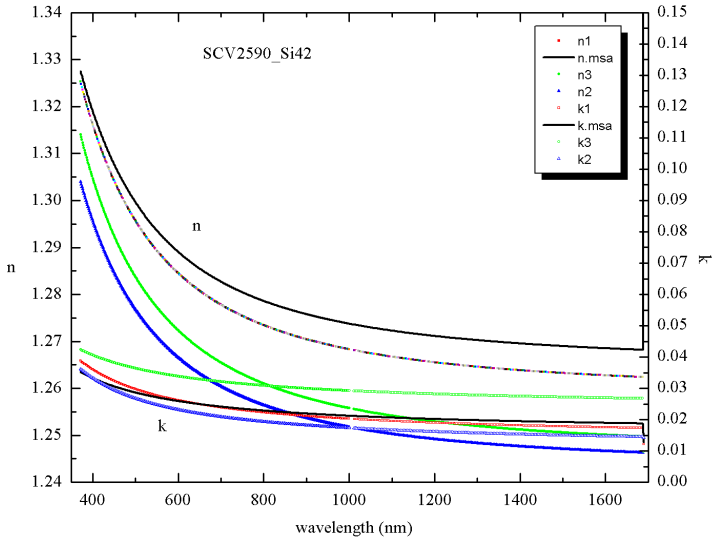

Figure F.5: SCV2590 Si42 optical constants after AO and deposition

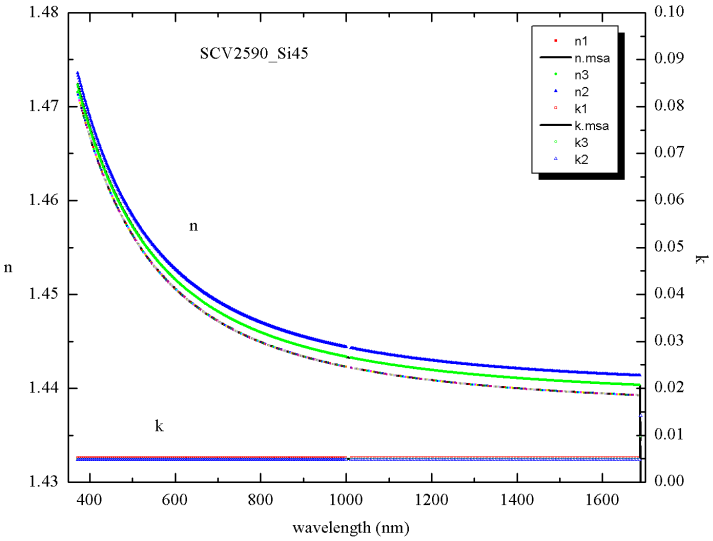

Figure F.6: SCV2590 Si45 optical constants after AO and deposition

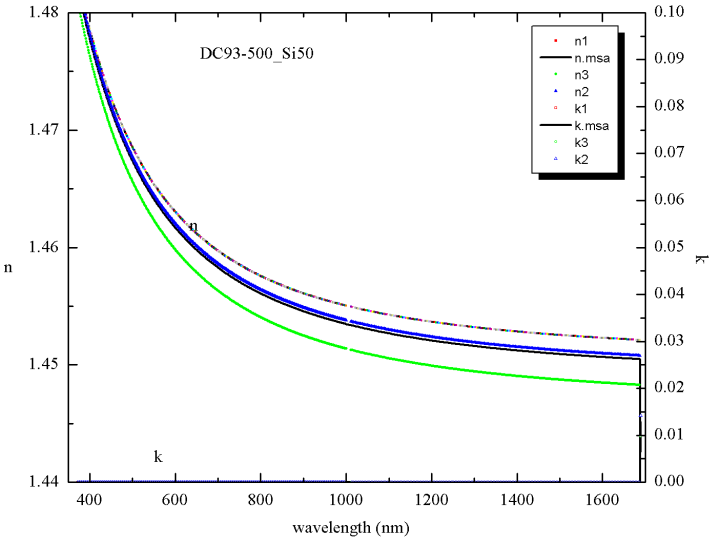

Figure F.7: DC93-500 Si50 optical constants after AO and deposition

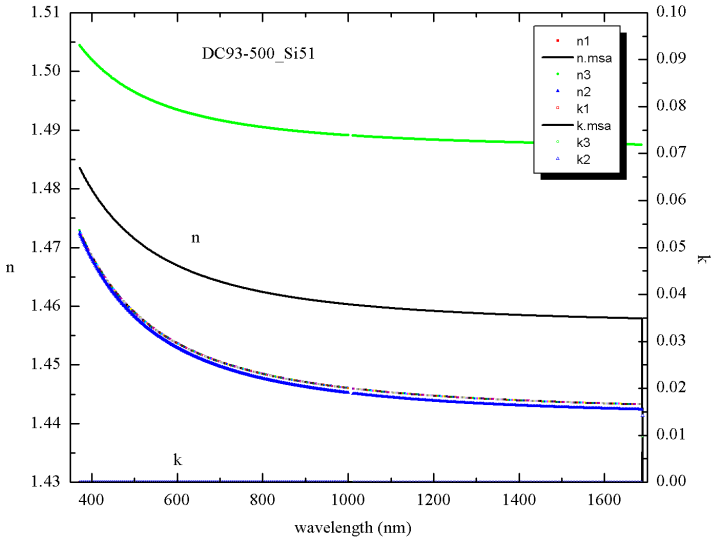

Figure F.8: DC93-500 Si51 optical constants after AO and deposition

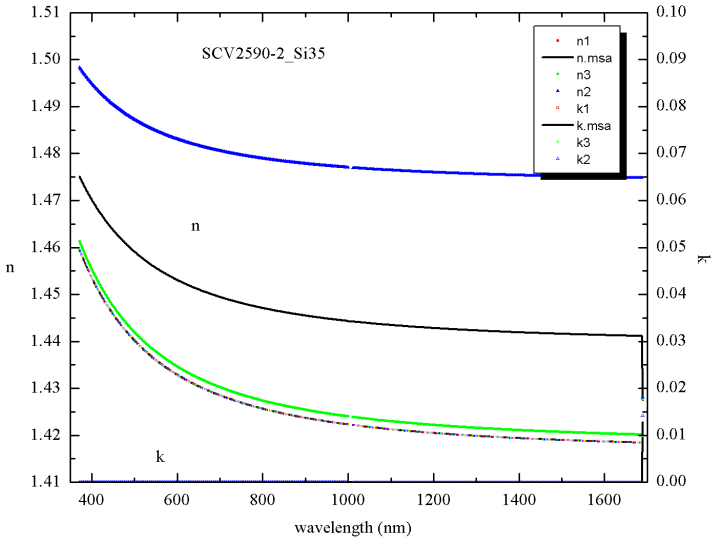

Figure F.9: SCV2590-2 Si35 optical constants after AO and deposition

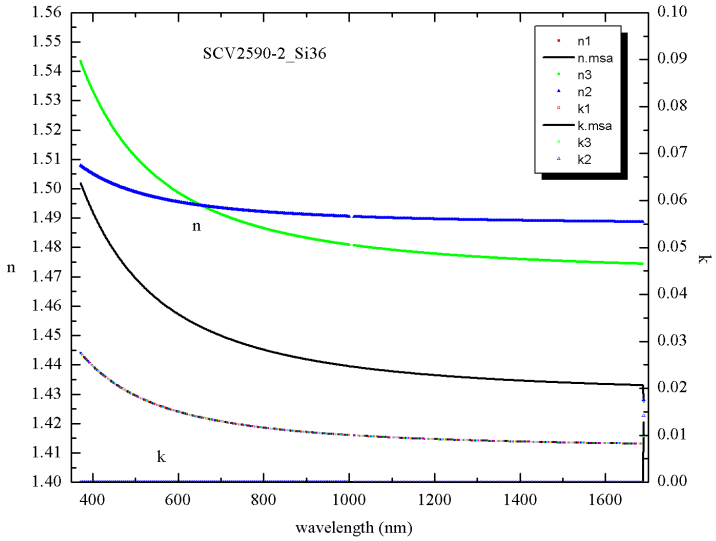

Figure F.10: SCV2590-2 Si36 optical constants after AO and deposition

Appendix G

VASE Fitting results for Chapter 6 Part I

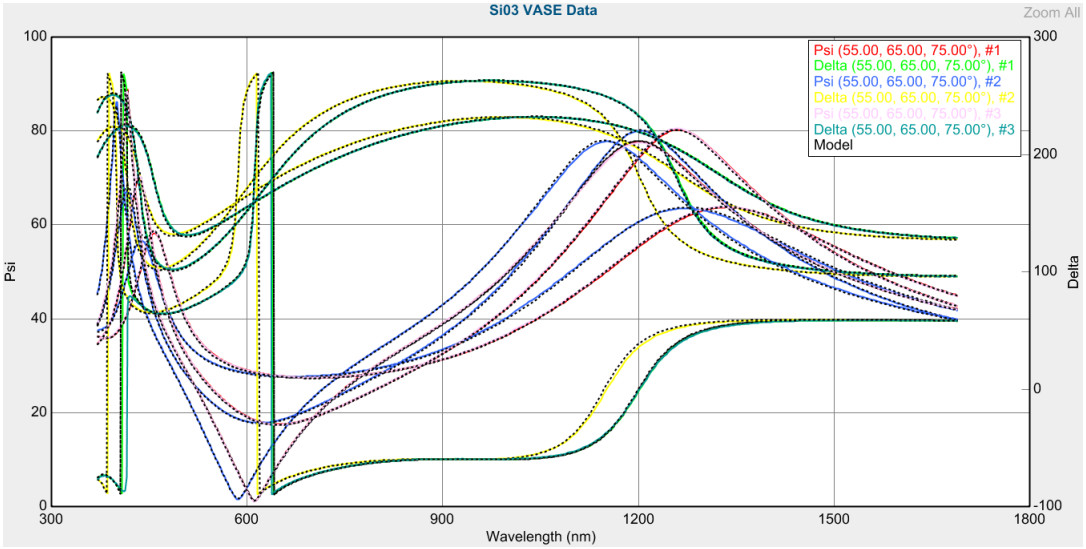

Figure G.1: RTV566 Si03 VASE Data before AO

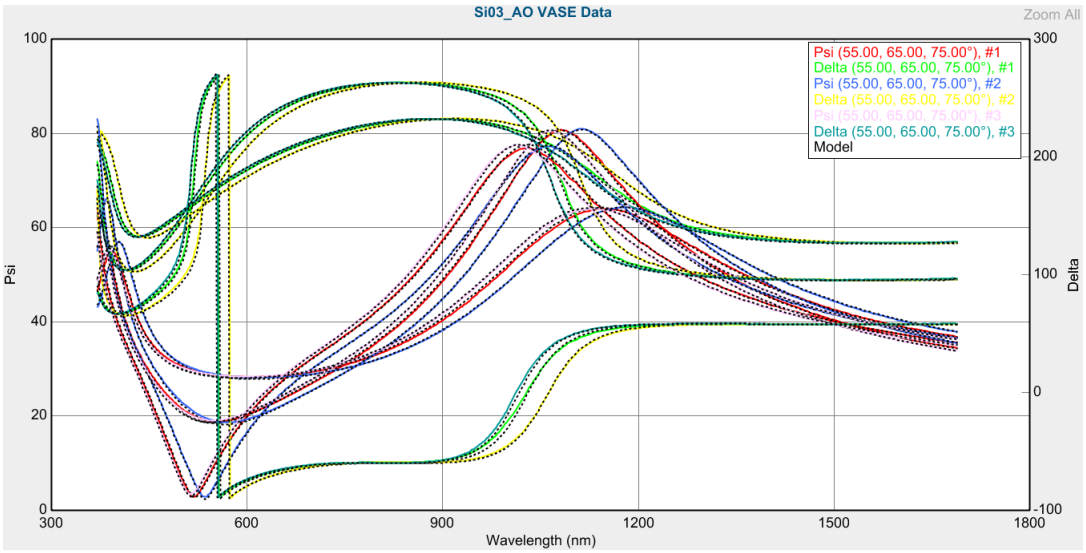

Figure G.2: RTV566 Si03 VASE Data after AO

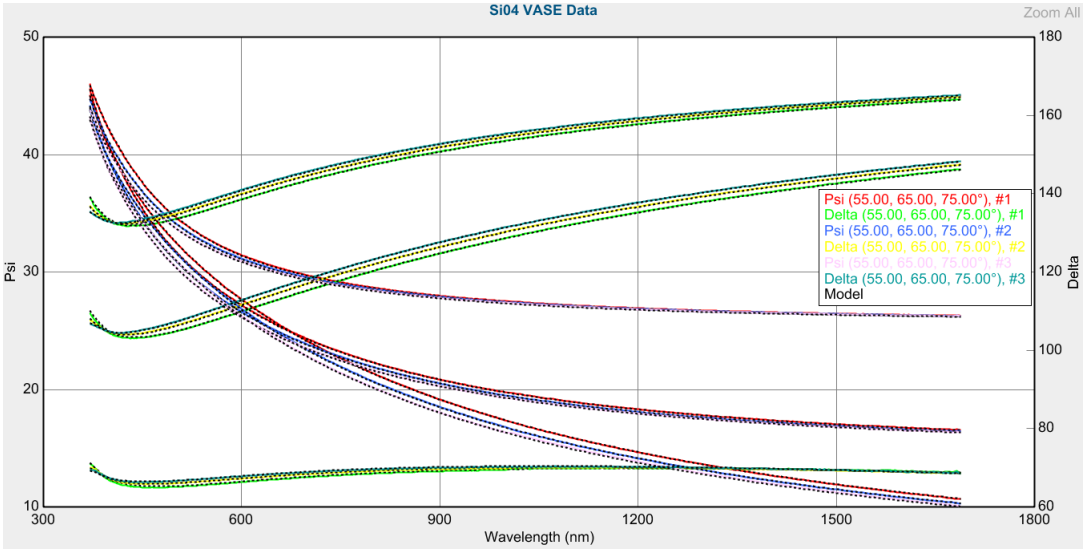

Figure G.3: RTV566 Si04 VASE Data before AO

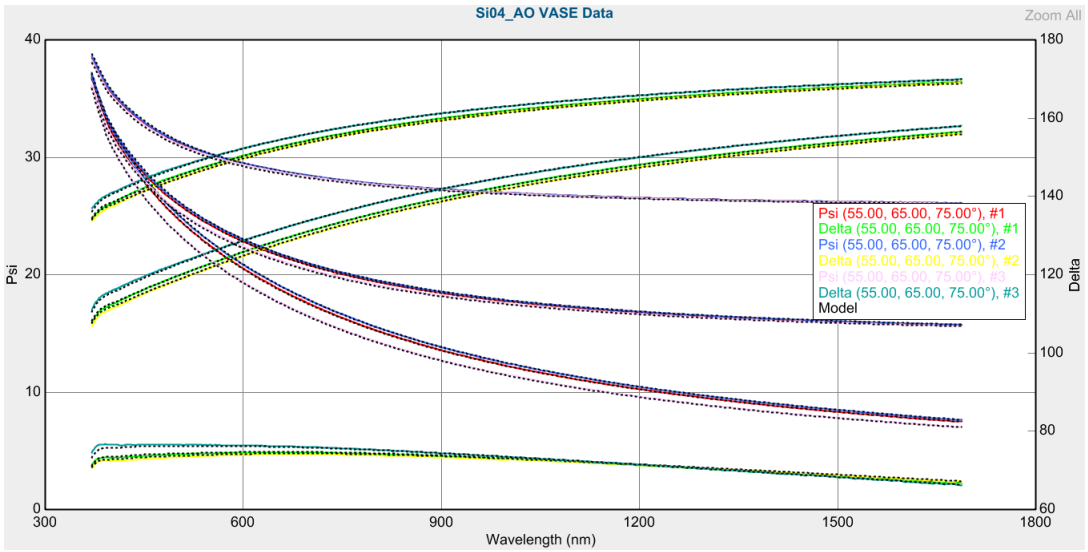

Figure G.4: RTV566 Si04 VASE Data after AO

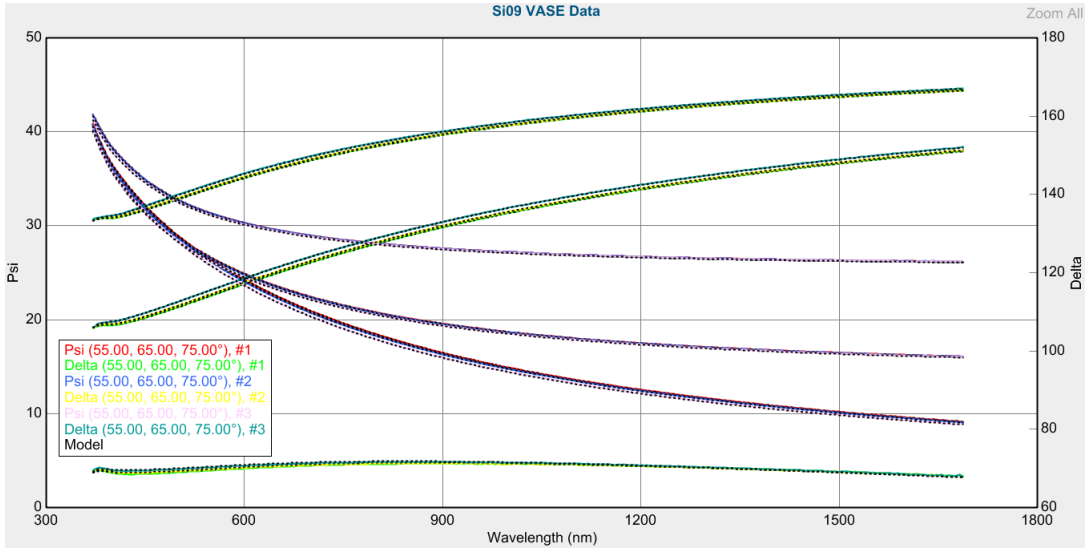

Figure G.5: CV2568 Si09 VASE Data before AO

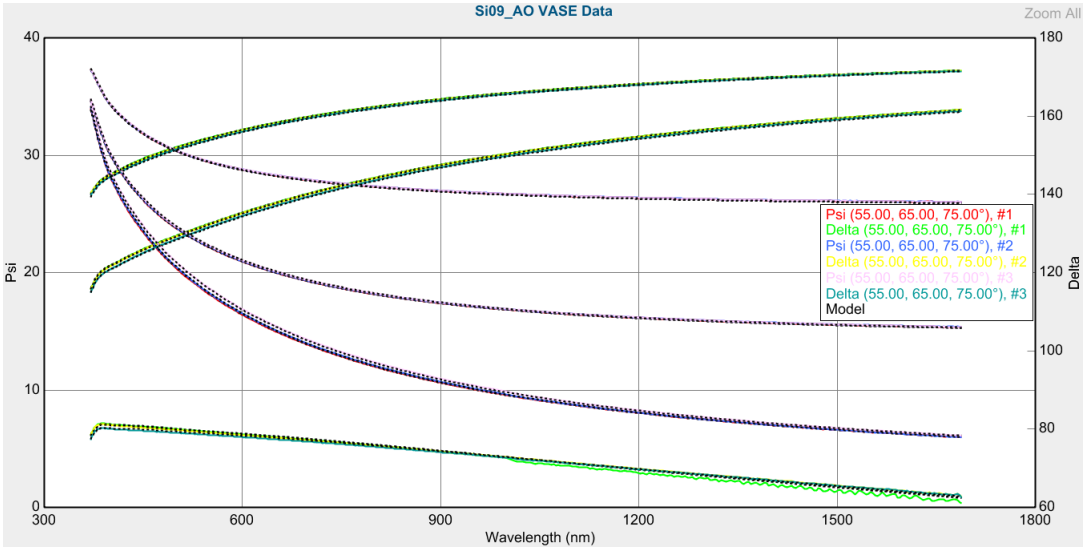

Figure G.6: CV2568 Si09 VASE Data after AO

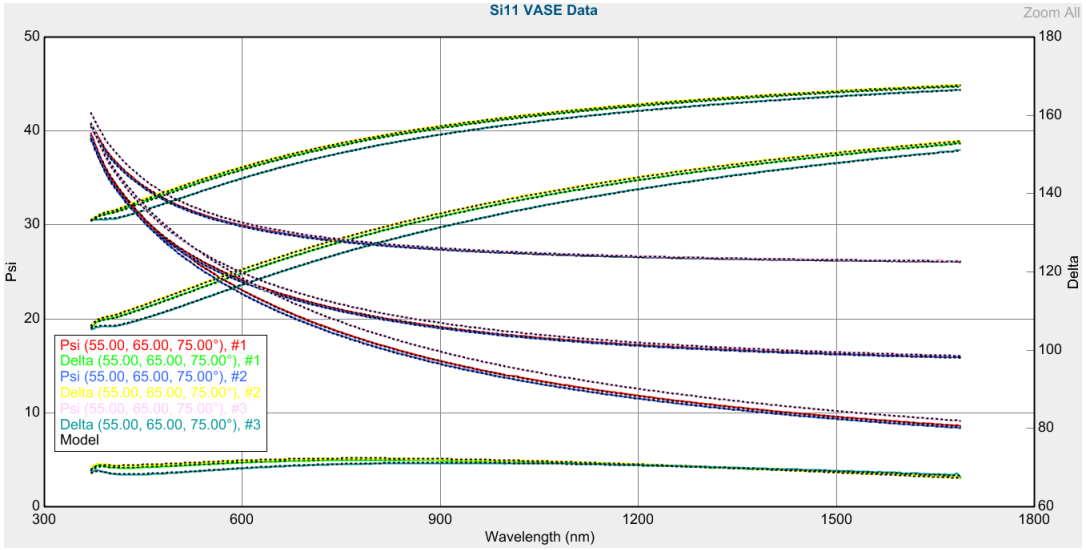

Figure G.7: CV2568 Si11 VASE Data before AO

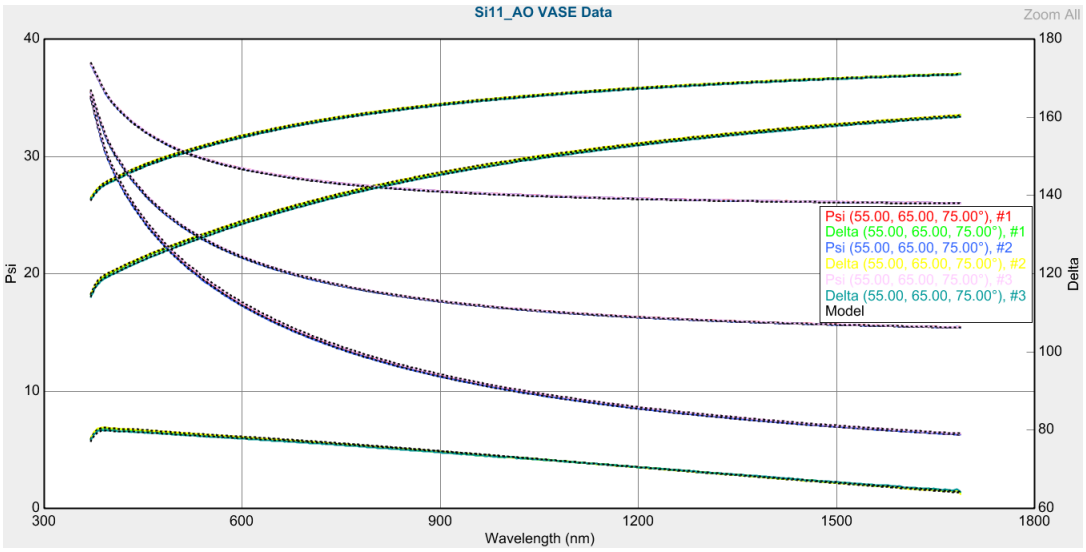

Figure G.8: CV2568 Si11 VASE Data after AO

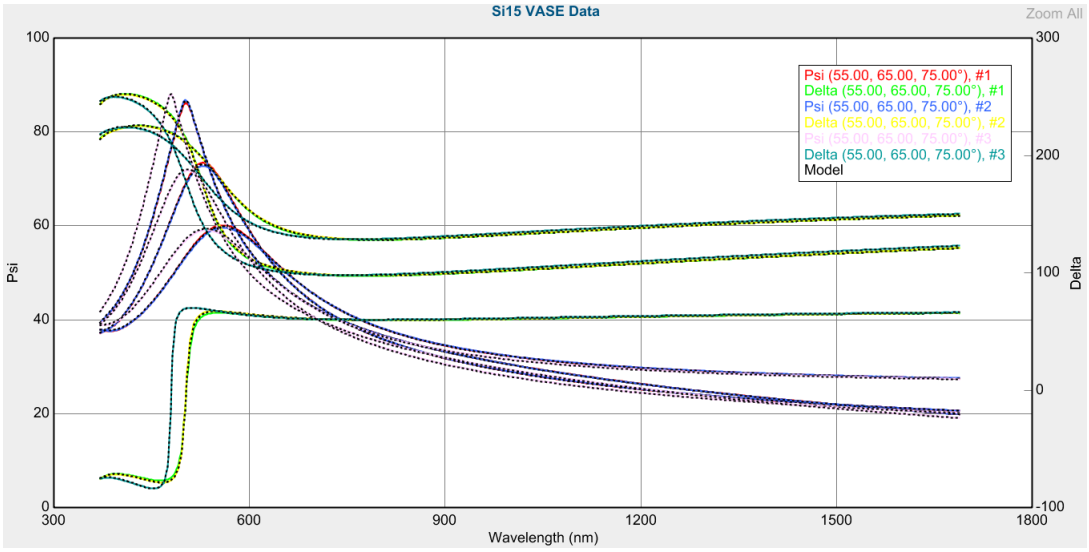

Figure G.9: SCV2590 Si15 VASE Data before AO

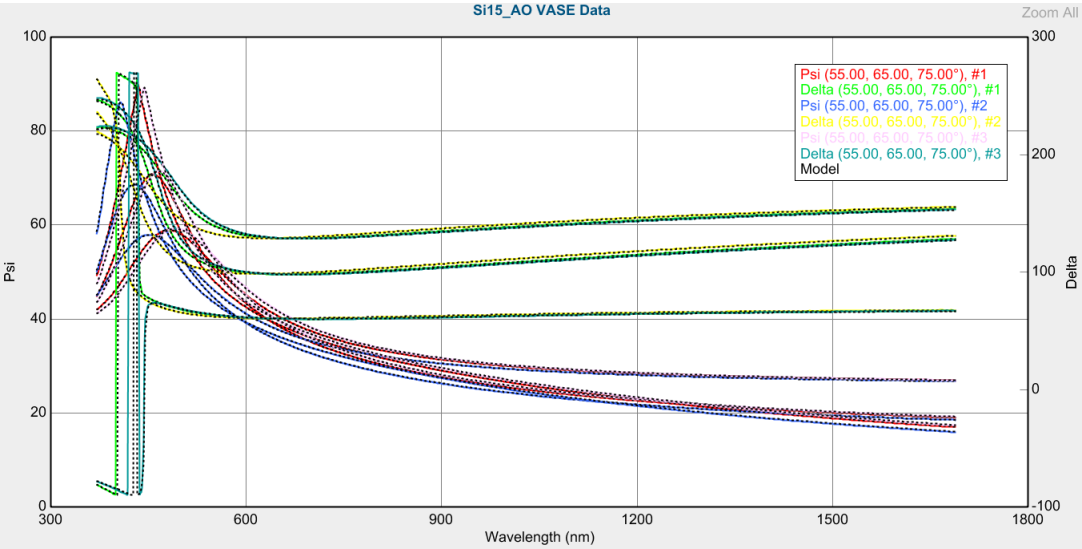

Figure G.10: SCV2590 Si15 VASE Data after AO

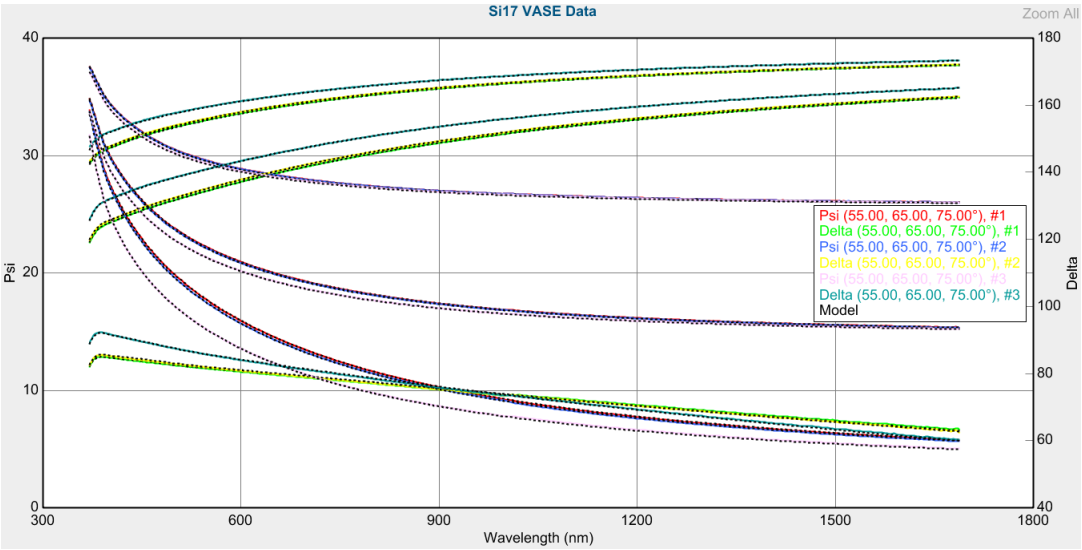

Figure G.11: SCV2590 Si17 VASE Data before AO

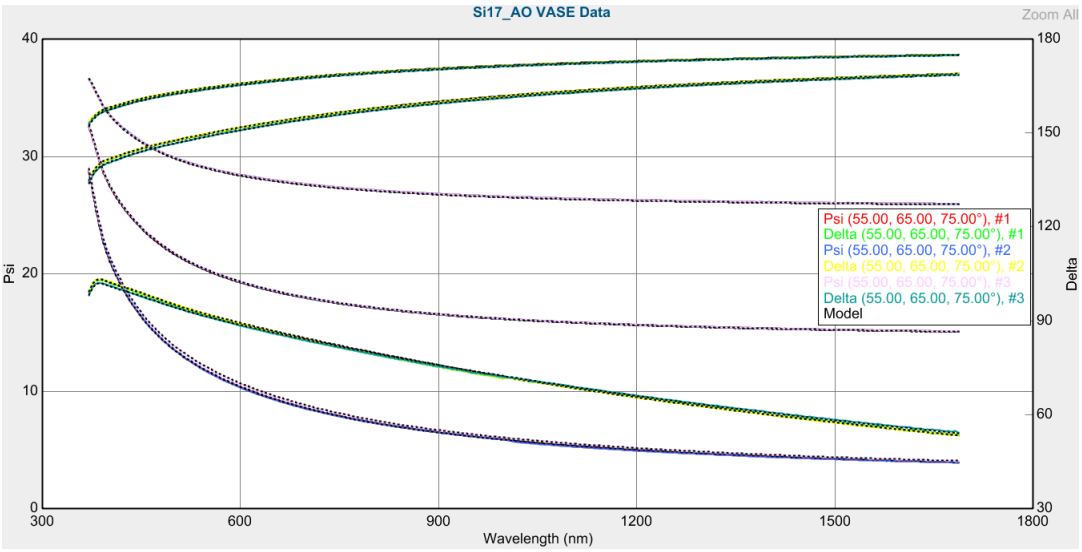

Figure G.12: SCV2590 Si17 VASE Data after AO

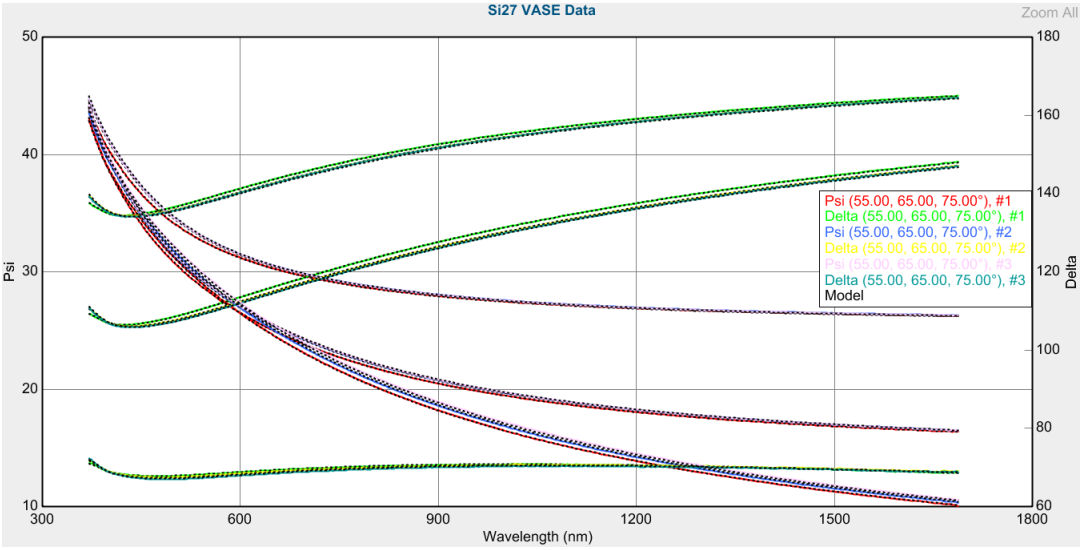

Figure G.13: SCV2590-2 Si27 VASE Data before AO

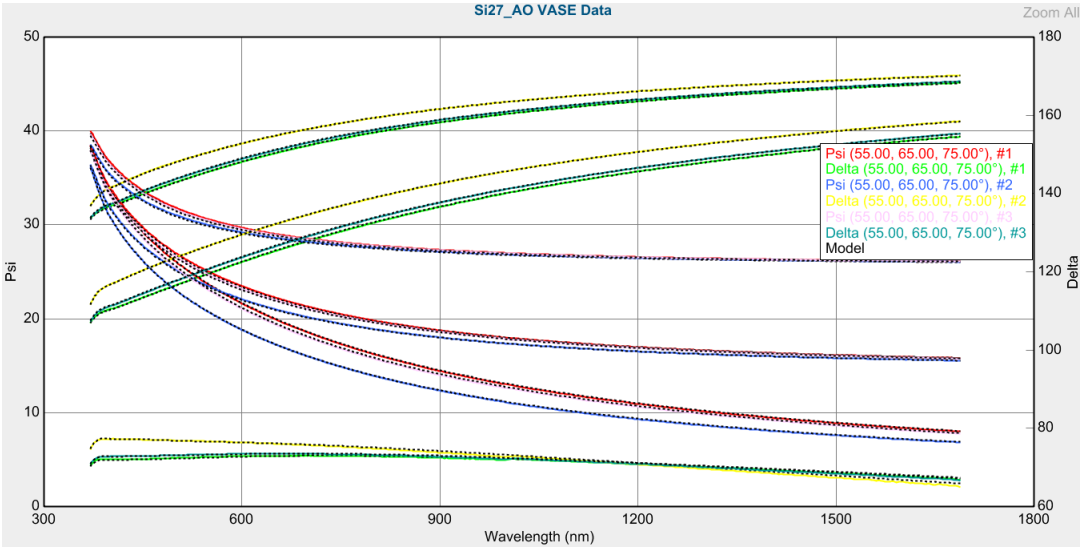

Figure G.14: SCV2590-2 Si27 VASE Data after AO

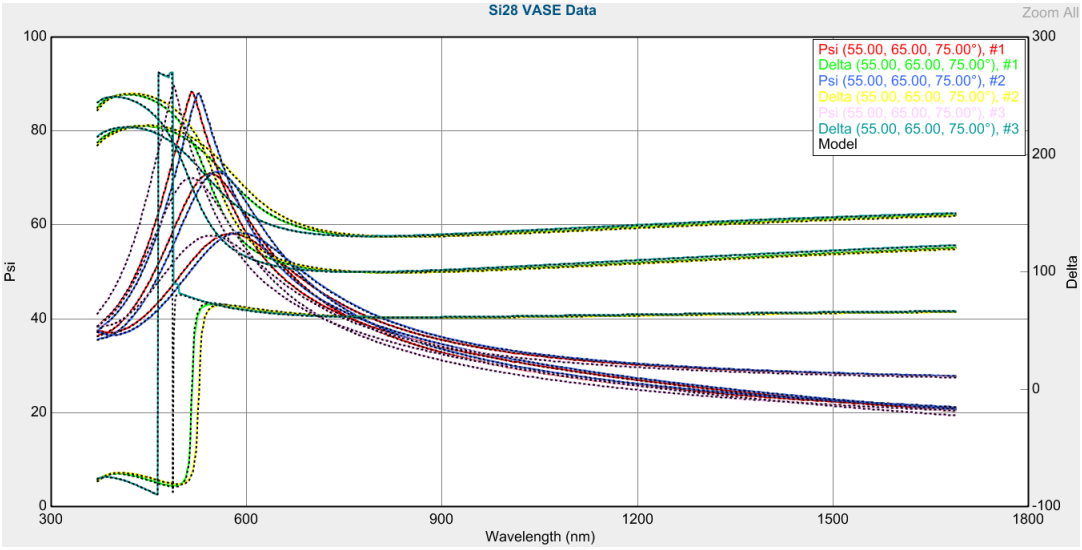

Figure G.15: SCV2590-2 Si28 VASE Data before AO

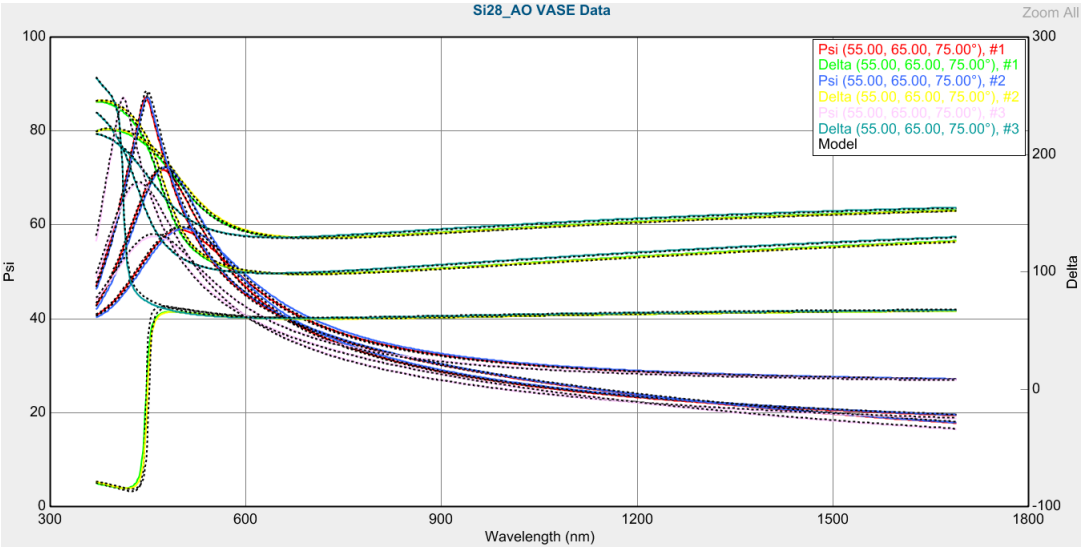

Figure G.16: SCV2590-2 Si28 VASE Data after AO

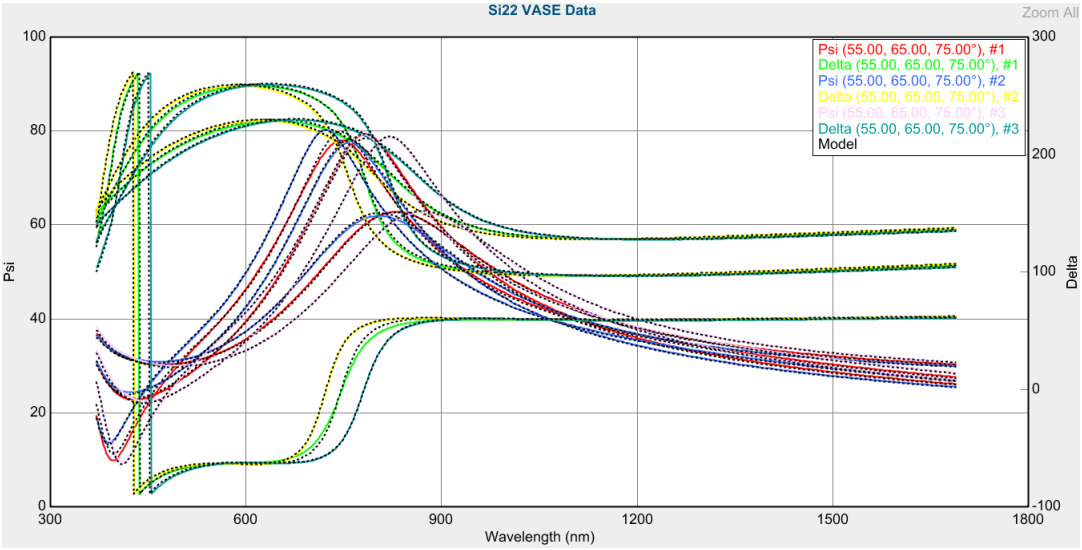

Figure G.17: DC93-500 Si22 VASE Data before AO

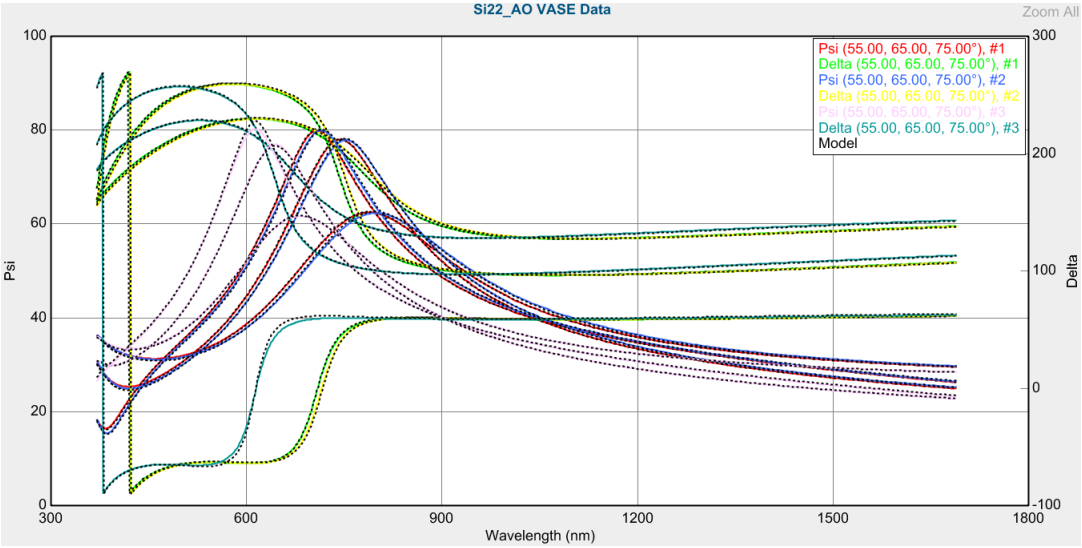

Figure G.18: DC93-500 Si22 VASE Data after AO

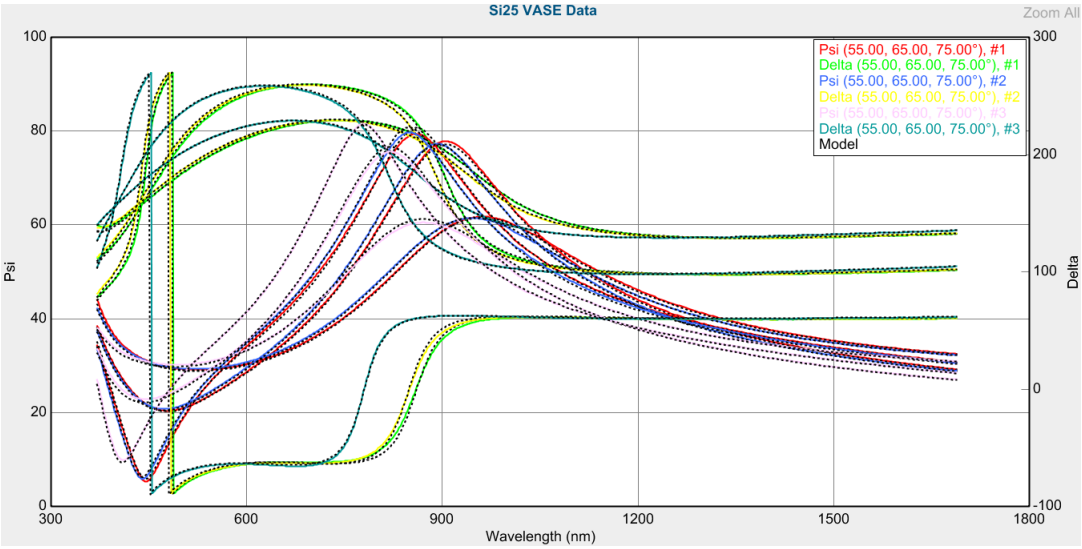

Figure G.19: DC93-500 Si25 VASE Data before AO

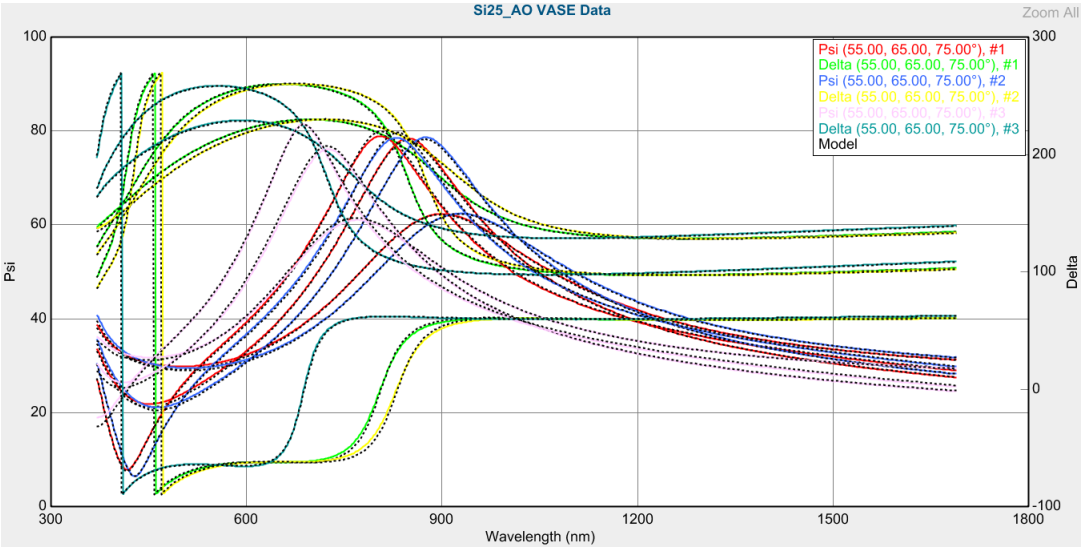

Figure G.20: DC93-500 Si25 VASE Data after AO

Appendix H

VASE Fitting results for Chapter 6 Part II

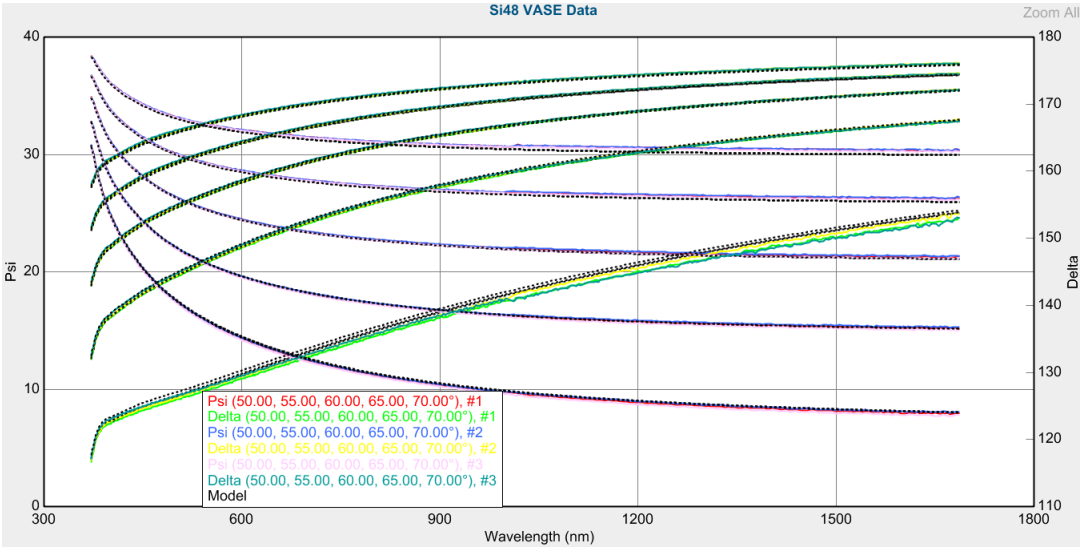

Figure H.1: RTV566 Si48 VASE Data with AO

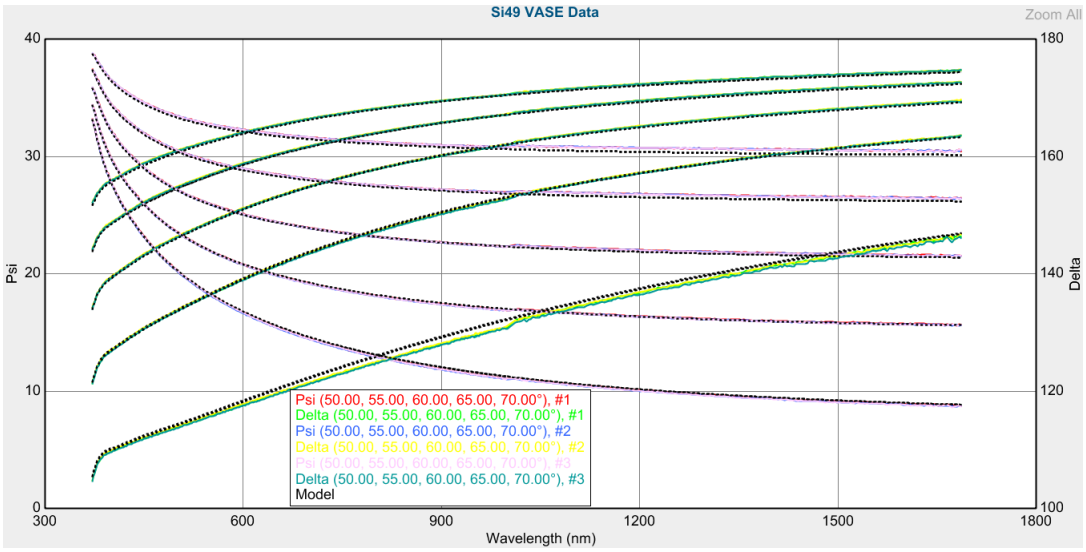

Figure H.2: RTV566 Si49 VASE Data with AO

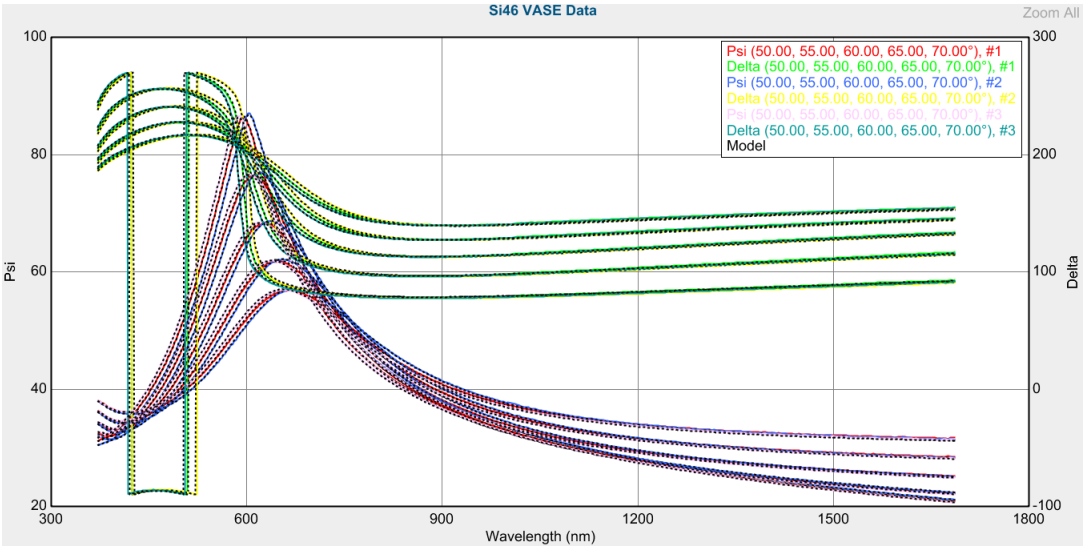

Figure H.3: CV2568 Si46 VASE Data with AO

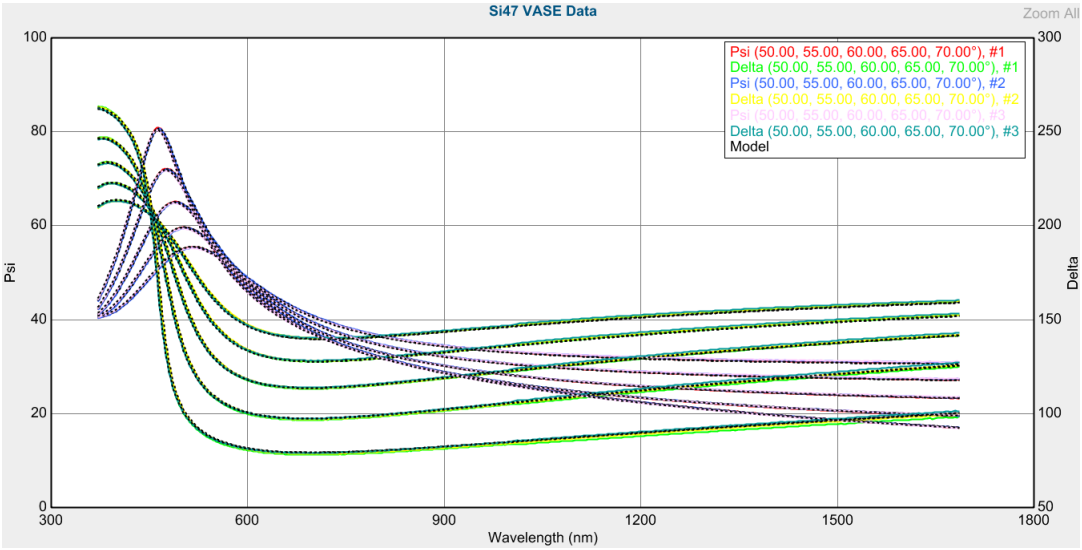

Figure H.4: CV2568 Si47 VASE Data with AO

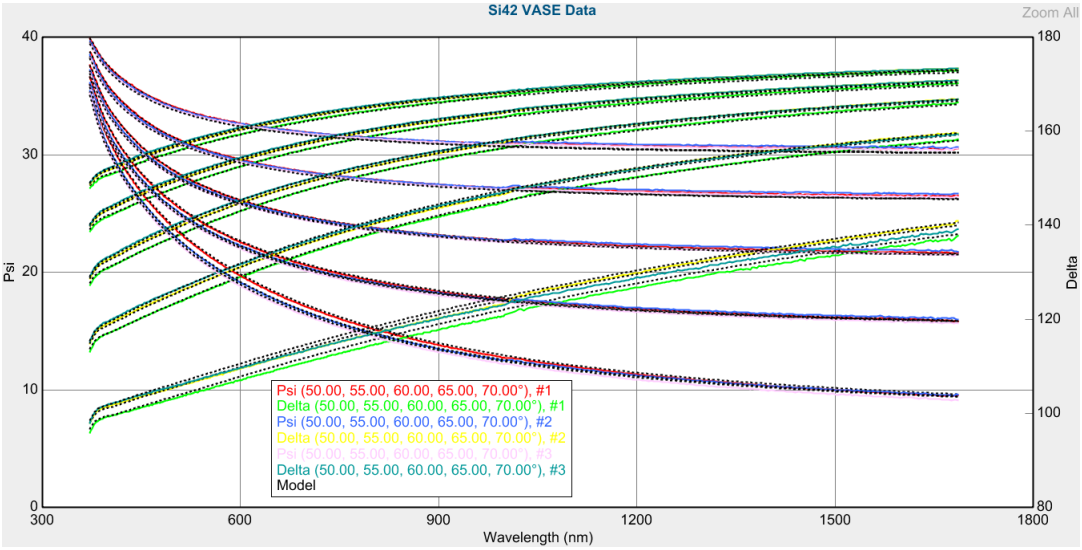

Figure H.5: SCV2590 Si42 VASE Data with AO

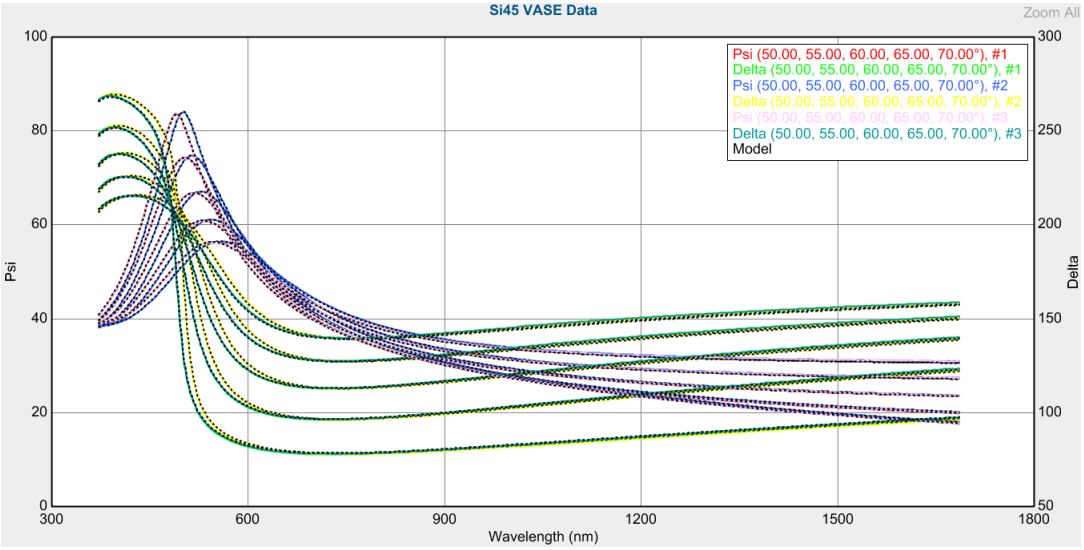

Figure H.6: SCV2590 Si45 VASE Data with AO

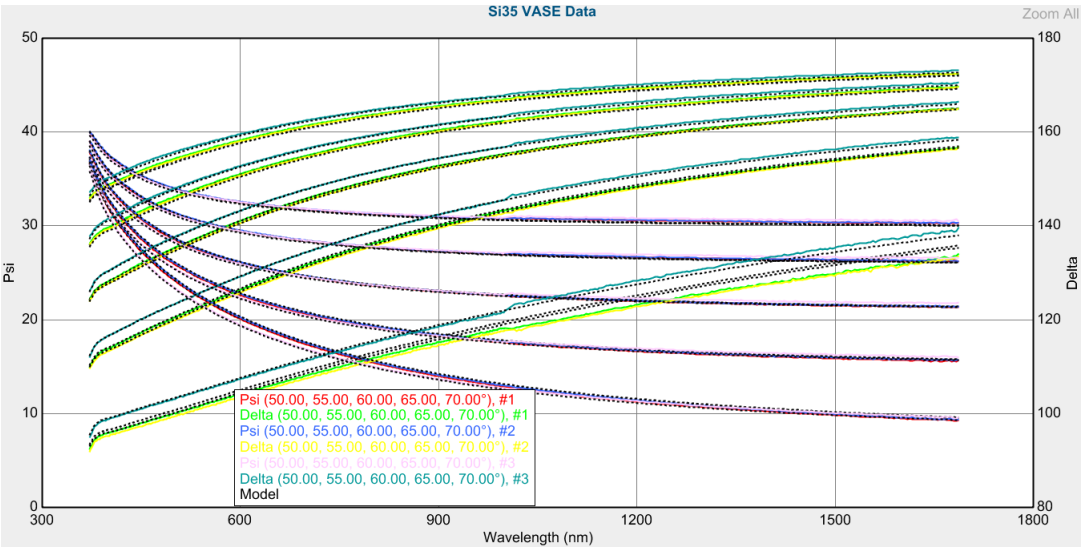

Figure H.7: SCV2590-2 Si35 VASE Data with AO

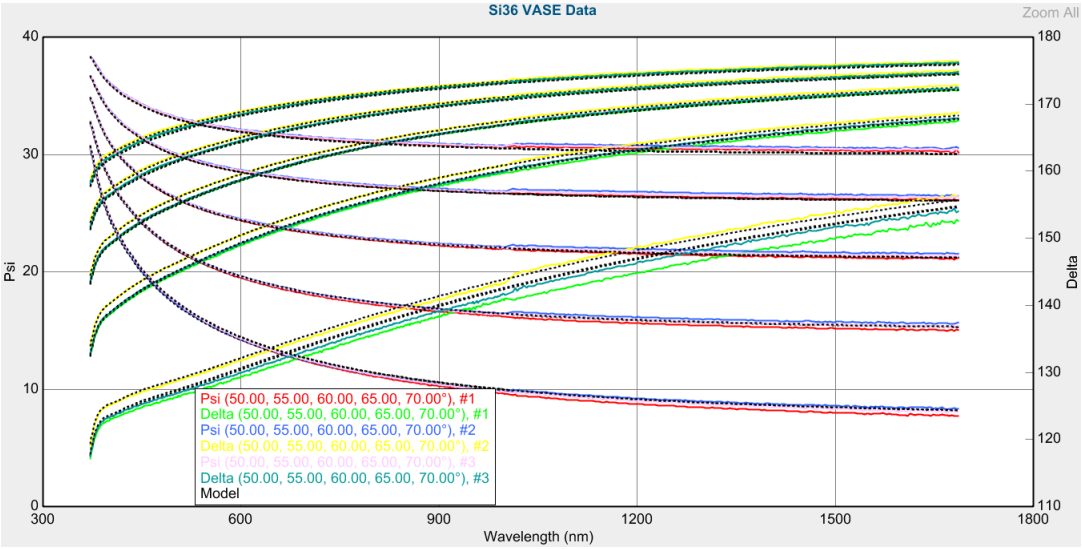

Figure H.8: SCV2590-2 Si36 VASE Data with AO

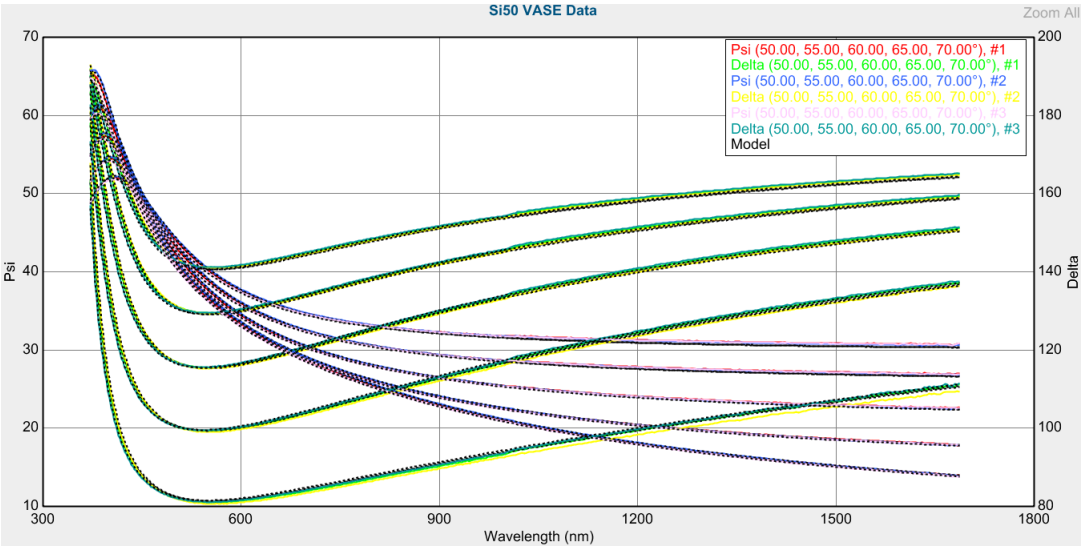

Figure H.9: DC93-500 Si50 VASE Data with AO

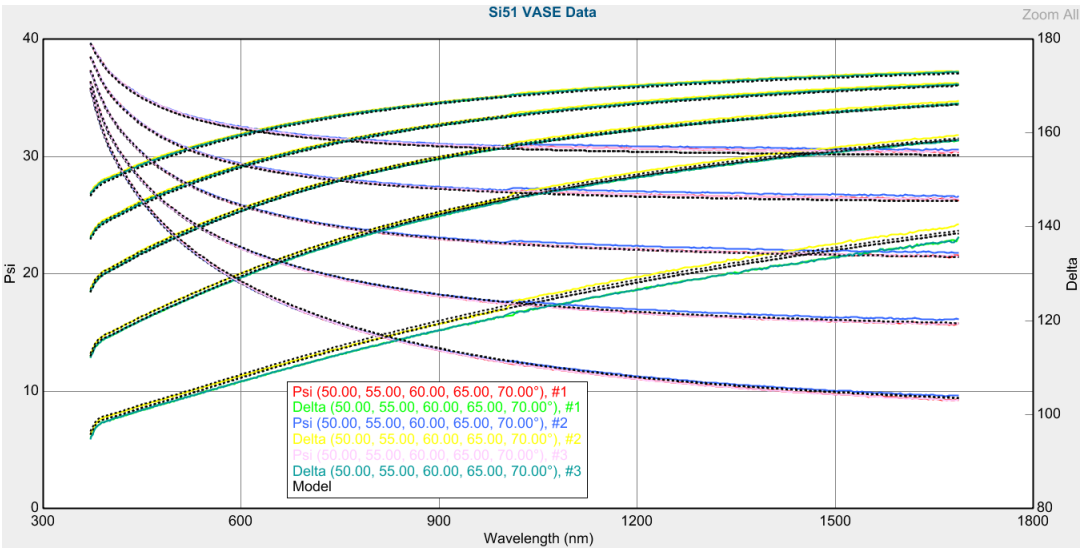

Figure H.10: DC93-500 Si51 VASE Data with AO

Bibliography

[1] B. L. Seiber; W. T. Bertrand; and B. E. Wood. Contamination effects of satellite material outgassing products on thermal surfaces and solar cells. Technical report, Arnold Engineering Development Center, 1990. 1, 2

[2] A. P. M. Glassford; J. W. Garrett. Characterization of contamination generation characteristics of satellite materials. Technical report, Astronaustics Division Lockheed Missiles and Space Co Inc, 1989. 1

[3] B. E. Wood; W. T. Bertrand; R. J. Bryson and B. L. Seiber. Surface effects of satellite outgassing products. Technical report, Arnold Engineering Development Center, 1986. 1

[4] *Controlled Volatility Materials Selection Guide*. 1

[5] J. W. Connell. Oxygen plasma-resistant phenylphosphine oxide-containing polyimides and poly(arylene ether heterocycle)s. *Polymer*, 36:13–19, 1995. 1, 5

[6] Bruce A. Banks. Simulation of the low earth orbital atomic oxygen interaction with materials by means of an oxygen ion beam. Technical report, NASA Lewis Research Center Group, 1989. 1, 94, 102

[7] S. Rutledge B. Banks. Issues and effects of atomic oxygen interactions with silicone contamination on spacecraft in low earth orbit. Technical report, Glenn Research Center, June 2000. 2, 4, 5

[8] *NASA Glenn Research Center's Materials International Space Station Experiments (MISSE 1-7)*, 2008. 2

[9] C. Karniotis D. Dworak, B. Banks. Evaluation of protective silicone siloxane coatings in simulated low-earth-orbit environment. *Journal of Spacecraft and Rockets*, 43(2):393–401, 2006. 2

[10] B. E. Wood W. T. Bertrand. Effects of spacecraft materials outgassing products on cryogenic surfaces. Technical report, Arnold Engineering Development Center, 1993. 2

[11] *Standard Test Method for Total Mass Loss and Collected Volatile Condensable Materials from Outgassing in a Vacuum Environment.* 2

[12] *Standard Test Method for Contamination Outgassing Characteristics of Spacecraft Materials.* 3

[13] Yu. I. Dorofeev V. E. Skurat, E. A. Barbashev. Simulation of polymer film and surface behaviour in a space environment. *Applied Surface Science*, 92(2):441–446, February 1996. 4, 102

[14] B. Riegler R. Johnson R. Thomaier V. Malave, B. Burkitt. Uniquely customized ultra low outgassing silicones to reduce contamination. *Journal of Spacecraft and Rockets*, 48:235–239, 2011. 4

[15] Bill Riegler; Brian Burkitt; Vicent Malave; Roy Johnson; Rob Thomaier. Recent developments in ultra low outgassing silicones for space applications. In *11th Japan International SAMPE Conference*, 2009. 4

[16] D. Silver. Outgassing issues and measurement protocols for spacecraft coatings. *Optical System Contamination: Effects, Measurements, and Control IV*, 2261:160–167, 1994. 4

[17] I. Gouzman E. Grossman. Space environment effects on polymers in low earth orbit. *Nuclear Instruments and Methods in Physics Research B*, 208:48–57, August 2003. 5, 102

[18] D. G. Zimcik. Plasma-deposited protective coatings for spacecraft applications. *Journal of Spacecraft and Rockets*, 28:652–657, 1991. 5

[19] S. Packirisamy. Atomic oxygen resistant coatings for low earth orbit space structures. *Journal of Materials Science*, 30:308–320, 1995. 5, 102

[20] S. A. Wallace D. A. Wallace. Use of a cryogenically cooled qcm in conjunction with a programmable data acquisition system to detect and examine accreted mass on the sensing crystal caused by environmental contamination. *Proceedings of the SPIE - The International Society for Optical Engineering*, 1165:424–431, 1990. 7

[21] N. V. Drozhzhin A. I. Belyaeva. Quartz microbalance for studying surface contamination in cryogenic devices. *Instruments and Experimental Techniques*, 36:660, 1994. 7

[22] D. F. Hall B. E. Wood. Qcm flight measurements of contaminant films and their effect on midcourse space experiment (msx) satellite qcm flight measurements of contaminant films and their effect on midcourse space experiment (msx) satellite optics. *Proc. SPIE - Photonics for Space Environments V*, 3124:34–40, 1997. 7, 102

[23] M. A. Baker. Use of a cooled quartz crystal microbalance to study the molecular flow and condensation of co2 in vacuum. *Journal of Vacuum Science and Technology*, 6:951 – 954, 1969. 7

[24] L. L. Levenson. Condensation coefficients of argon, krypton, xenon, and carbon dioxide measured with a quartz crystal microbalance. *Journal of Vacuum Science and Technology*, 8:629, 1971. 7

[25] I. Yu Y. Seo. Adsorption of n2 on a porous silica substrate studied by a quartz crystal microbalance. *Physical Review B*, 60:17003–17007, 1999. 7

[26] C. Delvac. Influence of monolayer amounts of hno3on the evaporation rate of h2o over ice in the range 179 to 208 k. *Journal of Physical Chemistry A*, 109:7151–7165, 2005. 7

[27] John R Vig. Quartz crystal resonators and oscillators for frequency control and timing applications. a tutorial. *NASA STI Recon Technical Report N*, 95:19519, 1994. 7

[28] Keiji Kanazawa. The oscillation frequency of a quartz resonator in contact with liquid. *Analytica Chimica Acta*, 175:99–105, 1985. 8

[29] D. Johannsmann. Viscoelastic, mechanical, and dielectric measurements on complex samples with the quartz crystal microbalance. *Physical Chemistry Chemical Physics*, 10:4516–4534, 2008. 8, 10

[30] R. N. Thurston. *Mechanics of Solids*. Heidelberg Springer, 1984. 8

[31] P. Horowitz and W. Hill. *The Art of Electronics (2 ed.)*. Cambridge University Press, 1989. 8

[32] A. Arnau, T. Sogorb, and Y. Jimenez. Circuit for continuous motional series resonant frequency and motional resistance monitoring of quartz crystal resonators by parallel capacitance compensation. *Review of Scientific Instruments*, 73:2724–2737, 2002. 8

[33] M. Rodahl and B. Kasemo. A simple setup to simultaneously measure the resonant frequency and the absolute dissipation factor of a quartz crystal microbalance. *Rev. Sci. Instr.*, 67:3238, 1996. 8

[34] D. Johannsmann, K. Mathauer, G. Wegner, and W. Knoll. Viscoelastic properties of thin films probed with a quartz-crystal resonator. *Phys. Rev. B*, 46:7808–7815, 1992. 8

[35] Virgil E Bottom. *Introduction to quartz crystal unit design*. Van Nostrand Reinhold; First edition, 1982. 8

[36] Sauerbrey G. Verwendung von schwingquarzen zur wagung dunner schichten und zur mikrowagung. *G Z. Phys*, 1959. 8

[37] O. Lewis C. Lu. Investigation of film thickness determination by oscillating quartz resonators with large mass load. *J. Appl. Phys.*, 43(11):4385–4390, 1972. 10

[38] D. Johannsmann. Viscoelastic analysis of organic thin films on quartz resonators. *Macromolecular Chemistry and Physics*, 200(3):501–516, 1999. 10

[39] Hiroyuki Fujiwara. *Spectroscopic Ellipsometry: Principles and Applications*. Wiley, 2007. 12, 16, 58

[40] David R. Lide. *CRC Handbook of Chemistry and Physics, 86th edition*. CRC Press, 2005. 31

[41] R.J. Goldstein. *Fluid Mechanics Measurements*. Hemisphere Publishing Corporation, New York, 1983. 33

[42] G. F. N. Fox and W. F. Weeks. Equations for determining the gas and brine volumes in sea-ice samples. *Journal of Glaciology*, 1983. 33

[43] Fen Zhou Hanrahan. *Study of low outgassing materials used for spacecraft: composition and outgassing characterization*. PhD thesis, Univerisity of Nebraska Lincoln, 2013. 46, 47, 94, 96

[44] Mathias Schubert. *Infrared Ellipsometry on Semiconductor Layer Structures*. Springer-Verlag Berlin Heidelberg, 2004. 58

[45] J. P. Li and A. J. Steckl. Nucleation and void formation mechanisms in sic thin film growth on si by carbonization. *J. Electrochem. Soc*, 1995. 75, 84, 88, 93, 114

[46] S. G. Warren. Optical constants of ice from the ultraviolet to the microwave. *Appl. Opt.*, 1984. 79

[47] Michael J. Yaszemskib Antonios G. Mikos Susan L. Ishaug-Riley, Genevieve M. Crane-Kruger. Three-dimensional culture of rat calvarial osteoblasts in porous biodegradable polymers. *Biomaterials*, 1998. 84, 88, 93, 114

[48] Jinming Cai Marco Bieri, Matthias Treier. Porous graphenes: two-dimensional polymer synthesis with atomic precision. *Chem. Commun.*, 2009. 84, 89, 93, 114

[49] B. Banks. Protection of solar array blankets from attack by low earth orbital atomic oxygen. In *IEEE photovoltaic specialists conference. 18*, pages 381–386, 1985. 94

[50] W. A. McGahan C. M. Herzinger, B. Johs and J. A. Woollam. Ellipsometric determination of optical constants for silicon and thermally grown silicon dioxide via a multi-sample, multi-wavelength, multi-angle investigation. *JOURNAL OF APPLIED PHYSICS*, 1998. 100

[51] C. Pailler A. Paillous. Degradation of multiply polymer-matrix composites induced by space environment. *Composites*, 25(4):287–295, April 1994. 102